2016

AN EXPERIMENTAL INVESTIGATION OF LOW TEMPERATURE COMBUSTION REGIMES IN A LIGHT DUTY ENGINE

Kaushik Kannan
Michigan Technological University, kkannan@mtu.edu

AN EXPERIMENTAL INVESTIGATION OF LOW TEMPERATURE COMBUSTION REGIMES IN A LIGHT DUTY ENGINE

By

Kaushik Kannan

A THESIS

Submitted in partial fulfillment of the requirements for the degree of

MASTER OF SCIENCE

In Mechanical Engineering

MICHIGAN TECHNOLOGICAL UNIVERSITY

2016

This thesis has been approved in partial fulfillment of the requirements for the Degree of MASTER OF SCIENCE in Mechanical Engineering.

Department of Mechanical Engineering- Engineering Mechanics

Thesis Advisor: *Dr. Mahdi Shahbakhti*

Committee Member: *Dr. Youngchul Ra*

Committee Member: *Dr. Scott Miers*

Department Chair: *Dr. William W. Predebon*

Dedication

To my Parents, Prathibha, Mentors, Friends and Baby Elephant

Ambition is a dream with a V8 Engine. – Elvis Presley.

Contents

List of Figures . . . . . **xiii**

List of Tables . . . . . **xxiii**

Preface . . . . . **xxvii**

Acknowledgments . . . . . **xxix**

List of Abbreviations . . . . . **xxxi**

Abstract . . . . . **xxxvii**

1 Introduction **1**

1.1 The evolution of Low temperature Combustion (LTC) engines . . . 3

1.2 Principle of Operation of LTC engines 8

1.3 Research Goals and Scope of Research 11

1.4 Organization of Thesis 12

2 Engine Instrumentation and Experimentation **15**

2.1 Engine Setup and Specifications 15

2.2 Port Fuel Injectors (PFI) Instrumentation, Calibration and Assembly 17

2.3 Supercharger control using dSpace 25

2.4 Engine Analysis Parameters 30

2.4.1 Engine Geometry 30

2.4.2 Net Work and Mean effective pressure 34

2.4.3 Polytropic Index 36

2.4.4 Combustion Stability 36

2.4.5 Heat Transfer Coefficient Correlation 38

2.4.6 Combustion Efficiency 40

2.5 Filter Design for Pressure trace 41

2.6 Uncertainty in Analysis 43

2.7 BMEP Parametrization 48

2.8 Accounting for Supercharger losses 49

2.9 SI Map for Baseline Comparison 52

3 Homogeneous Charge Compression Ignition (HCCI) 53

3.1 Parametrization of BMEP using Flynn-Chen Model for HCCI combustion regime 54

3.2 Operating Range 56

3.3 Maps for ISFC, BSFC, Indicated Thermal Efficiency and Exhaust Gas Temperature 59

3.4 Optimized HCCI maps 68

3.5 Effects of RON on HCCI combustion 75
3.6 Effects of Intake Air temperature on HCCI combustion 78
3.7 Effect of boost pressure on HCCI combustion 82

4 Reactivity Controlled Compression Ignition (RCCI) 85
4.1 Parametrization of BMEP using Flynn-Chen Model for RCCI combustion regime 86
4.2 Operating Range 88
4.3 Maps for ISFC, BSFC, Indicated Thermal efficiency and Exhaust gas temperature 91
4.4 Optimized RCCI maps 96
4.5 RCCI optimized maps with supercharger losses accounted 103
4.6 RCCI optimized maps with COV of IMEP less than 5 percent . . . 106
4.7 Effects of PR on RCCI combustion 108
4.8 Effects of Intake Air Temperature on RCCI Combustion 114
4.9 Effect of boost pressure on RCCI combustion 118

5 Partially Premixed Compression Ignition (PPCI) 123
5.1 Parametrization of BMEP using Flynn-Chen Model for PPCI combustion regime 124
5.2 Operating Range Maps 126
5.3 Maps for ISFC, BSFC, Indicated Thermal Efficiency and Exhaust Gas Temperature 128

5.4 Optimized PPCI maps 133
5.5 Effect of Intake Air Temperature on PPCI Combustion 138
5.6 Effects of Boost pressure on PPCI combustion 144
5.7 Effect of SOI on PPCI combustion 151

6 Summary and Conclusions 157
6.1 Conclusions 158
6.1.1 Operating range and performance maps 158
6.1.2 Parametric Study on Combustion and Performance characteristics 162
6.2 Major Contribution towards the thesis 164
6.3 Future Work 166

References 169

A Table of Data points for Experiments 181
A.1 PPCI 181
A.2 HCCI 192
A.3 RCCI 197

B MSc Publications 203
B.1 Conference Papers 203
B.2 Journal Paper 204

C Program and Data File Summary **205**

D Letters of Permission **217**

List of Figures

1.1 Contour plots of soot, NO_x, HC and CO depicting the operating regions of several combustion regimes [1] (Letter of permission D.1) . 2

1.2 Comparison of diesel, Gasoline and HCCI engine [2] (Permission letter given in D.2) 9

1.3 Thesis Organization 13

2.1 Schematic of the LTC engine setup 16

2.2 Experimental LTC Engine Setup 18

2.3 Port fuel injector assembly 19

2.4 Triggered sub-system for PFI control 20

2.5 Monitoring Panel on dSPACE Control Desk for PFI Control 20

2.6 Verification of dSPACE model for calculating injected fuel mass from using DI injectors 21

2.7 Calibration and Verification of the PFI injectors for Iso-Octane fuel 23

2.8 Calibration and Verification of the PFI injectors for n-Heptane fuel 24

2.9 Supercharger VFD unit 26

2.10 Supercharger Frequency maps for IVO of a) -24.5 CAD bTDC and b) 25.5 CAD bTDC 27

2.11 Simulink Model for Supercharger Control using dSpace 28

2.12 Supercharger User Control panel on dSpace control desk 29

2.13 Supercharger power consumed if assumed to be mounted on the engine 51

2.14 Supercharger performance map for Eaton M62 supercharger [3] . . . 51

2.15 ISFC map for Spark Ignition (SI) mode 52

3.1 Experimental FMEP vs Parameterized FMEP 55

3.2 HCCI IMEP and speed range 58

3.3 HCCI IMEP and speed range for 40 °C intake air temperature and 120 kPa intake pressure 59

3.4 HCCI ISFC map for 40 °C intake air temperature at naturally aspirated conditions 60

3.5 HCCI ISFC map for 40 °C intake air temperature and 120 kPa intake pressure 61

3.6 HCCI BSFC map for 40 °C intake air temperature at naturally aspirated conditions 63

3.7 HCCI BSFC map for 40 °C intake air temperature at 120 kPa intake pressure 64

3.8 HCCI indicated thermal efficiency map for 40 °C intake air temperature at naturally aspirated conditions 65

3.9 HCCI Indicated thermal efficiency map for 40 °C intake air temperature and 120 kPa intake pressure 66

3.10 HCCI exhaust gas temperature map for 40 °C intake air temperature and Naturally aspirated 67

3.11 HCCI exhaust gas temperature map for 40 °C intake air temperature and 120 kPa Boost Pressure 68

3.12 HCCI ISFC map for all intake air temperatures and RONs at naturally aspirated conditions 69

3.13 HCCI ISFC map for all intake air temperatures and RONs and 120 kPa intake pressure 70

3.14 HCCI BSFC map for all intake air temperatures and RONs at naturally aspirated conditions 71

3.15 HCCI BSFC map for all intake air temperatures and RONs and 120 kPa intake pressure 71

3.16 HCCI indicated thermal efficiency map for all intake air temperatures and RONs at naturally aspirated conditions 72

3.17 HCCI indicated thermal efficiency map for all intake air temperatures and RONs and 120 kPa intake pressure 73

3.18 HCCI exhaust temperature map for all intake air temperatures and RONs at naturally aspirated conditions 74

3.19 HCCI exhaust temperature map for all intake air temperatures and RONs and 120 kPa intake pressure 74

3.20 a) Pressure and heat release rates for RON 0, 20 and 40 at 1000 rpm and intake temperature of 100 °C and b) Combustion phasing parameters for HCCI combustion regime 77

3.21 Effects of the RON on a) IMEP, b) Indicated thermal efficiency and c) Combustion efficiency for HCCI combustion regime 78

3.22 Effects of the intake air temperature on 1. IMEP, 2. Indicated thermal efficiency and 3. Combustion efficiency for HCCI combustion regime 80

3.23 a) Pressure and heat release rates for intake air temperatures 40, 60, 80 and 100 °C at 1000 rpm and RON of 20 and b) Effects of the intake air temperature on combustion characteristics (CA10 CA50, CA90 and Burn Duration) for HCCI combustion regime 81

3.24 Pressure and heat release rates for intake pressures 100 kPa, 120 kPa and 140 kPa at 1000 rpm and RON 40 83

3.25 Effects of intake pressure on combustion characteristics (CA10 CA50, CA90 and Burn Duration) for HCCI combustion regime 84

3.26 Effects of the boost pressure on (a) IMEP, (b) Indicated thermal efficiency and (c) Combustion efficiency for HCCI combustion regime . 84

4.1 Experimental FMEP vs Parameterized FMEP 87

4.2 RCCI IMEP and speed range for 40 °C intake air temperature and boost pressure of 140 kPa 89

4.3 RCCI IMEP and speed range for 60 °C intake air temperature and boost pressure of 140 kPa 90

4.4 RCCI ISFC map for three PRs at 40 °C intake air temperature and intake pressure of 140 kPa 92

4.5 RCCI BSFC map for three PRs at 40 °C intake air temperature and 140 kPa intake pressure 93

4.6 RCCI Indicated thermal efficiency map for three PRs at 40 °C intake air temperature and 140 kPa intake pressure 94

4.7 RCCI Exhaust gas temperature map for three PRs at 40 °C intake air temperature and 140 kPa boost pressure 95

4.8 RCCI ISFC optimized map for all intake air temperatures and PRs for naturally aspirated conditions 97

4.9 RCCI ISFC optimized map for all intake air temperatures and PRs at 140 kPa boost pressure 98

4.10 RCCI BSFC optimized map for all intake air temperatures and PRs at naturally aspirated conditions 99

4.11 RCCI BSFC optimized map for all intake air temperatures and PRs at 140 kPa intake pressure 99

4.12 RCCI indicated thermal efficiency optimized map for all intake air temperatures and PRs at naturally aspirated conditions 101

4.13 RCCI indicated thermal efficiency optimized map for all intake air temperatures and PRs at 140 kPa intake pressure 101

4.14 RCCI exhaust temperature optimized map for all intake air temperatures and PRs at naturally aspirated conditions 102

4.15 HCCI exhaust temperature optimized map for all intake air temperatures and PRs at 140 kPa intake pressure 103

4.16 Optimized ISFC map for RCCI combustion regime with supercharger losses accounted for 105

4.17 Optimized $\eta_{th,ind}$ map for RCCI combustion regime with supercharger losses accounted for 105

4.18 ISFC optimized map for RCCI combustion regime for COV of IMEP less than 5% at naturally aspirated conditions 106

4.19 Indicated thermal efficiency optimized map for RCCI combustion regime for COV of IMEP less than 5% at naturally aspirated conditions 107

4.20 ISFC optimized map for RCCI combustion regime for COV of IMEP less than 5% and boosted conditions 107

4.21 Indicated thermal efficiency optimized map for RCCI combustion regime for COV of IMEP less than 5% and boosted conditions . . . 108

4.22 Pressure and heat release rates for PR 20, 40 and 60 for operating conditions listed in Table 4.4 111

4.23 Heat release rate characteristics for RCCI combustion 112

4.24 Effects of PR on combustion characteristics (CA10 CA50, CA90 and Burn Duration) for RCCI combustion regime 112

4.25 Effects of PR on (a) IMEP, (b) Indicated thermal efficiency and (c) Combustion efficiency for RCCI combustion regime 113

4.26 Pressure and heat release rates for PR 20 for operating conditions listed in Table 4.5 116

4.27 Effect of intake air temperature on combustion characteristics (CA10 CA50, CA90 and Burn Duration) for RCCI combustion regime . . . 117

4.28 Effects of T_{intake} on (a) IMEP, (b) Indicated thermal efficiency and (c) Combustion efficiency for RCCI combustion regime 118

4.29 Pressure and heat release rates for PR 20 for operating conditions listed in Table 4.6 120

4.30 Effects of intake pressure on combustion characteristics (CA10 CA50, CA90 and Burn Duration) for RCCI combustion regime 121

4.31 Effects of intake pressure on (a) IMEP, (b) Indicated Thermal efficiency and (c) Combustion efficiency for RCCI combustion regime 121

5.1 Experimental FMEP vs Parameterized FMEP 125

5.2 PPCI IMEP and speed range for 40 °C intake air temperature at naturally aspirated conditions 127

5.3 PPCI IMEP and speed range for 80 °C intake air temperature at naturally aspirated conditions 128

5.4 PPCI ISFC map for 40 °C intake air temperature at naturally aspirated conditions 130

5.5 PPCI BSFC map for 40 °C intake air temperature at naturally aspirated conditions 131

5.6 PPCI indicated thermal efficiency map for 40 °C intake air temperature at naturally aspirated conditions 132

5.7 PPCI exhaust gas temperature map for 40 °C intake air temperature at naturally aspirated conditions 133

5.8 PPCI ISFC optimized map for all intake air temperatures and RONs at naturally aspirated conditions 134

5.9 PPCI BSFC optimized map for all intake air temperatures and RONs at naturally aspirated 135

5.10 PPCI indicated thermal efficiency optimized map for all intake air temperatures and RONs at naturally aspirated conditions 136

5.11 PPCI exhaust temperature optimized map for all intake air temperatures and RONs at naturally aspirated conditions 137

5.12 Effect of intake air temperature on PPCI in-cylinder pressure at a lambda of 2 139

5.13 Effect of intake air temperature on the PPCI heat release rate at a lambda of 2 140

5.14 Effect of Intake temperature on IMEP and BMEP at a lambda of 2 141

5.15 Effect of intake temperature on indicated thermal efficiency at a lambda of 2 142

5.16 Effect of intake temperature on combustion phasing at a lambda of 2 143

5.17 Effect of boost pressure on IMEP in the PPCI regime 145

5.18 Variation of cylinder pressure versus crank angle at different intake manifold pressures at constant fuel energy 749 J in the PPCI regime 146

5.19 Variation of heat release rate versus crank angle at different intake manifold pressures at constant fuel energy 749 J in the PPCI combustion regime 148

5.20 Variation of indicated thermal efficiency with lambda at different intake manifold pressures in PPCI combustion regime 149

5.21 Effect of intake manifold pressure on CA50 at different lambda values in PPCI combustion regime 150

5.22 Effects of SOI on in-cylinder pressure in PPCI combustion regime . 153

5.23 Effects of SOI on heat release rate in PPCI combustion regime . . . 154

5.24 Effects of SOI on CA10, CA50 and CA90 in PPCI combustion regime 155

D.1 Copyright permission for the Figure 1.1 217

D.2 Copyright permission for the Figure 1.2 218

List of Tables

2.1 Engine Specifications 17

2.2 Port Fuel Injector (Bosch EV14) Specifications 18

2.3 Uncertainties involved in Measurement of independent parameters during experimentation 44

2.4 Range of Uncertainties involved in estimation of parameters 45

2.5 Uncertainties of calculated variables with respect to independent parameters 46

2.6 Test parameters 47

2.7 Mean and Standard deviation for repeatability (three trials) 47

3.1 Operating Parameters for HCCI Combustion Mode 54

3.2 Error in estimation of FMEP 55

3.3 Coefficients for the Flynn- Chen Model 56

3.4 Operating conditions used for the experiments to study the effect of RON on HCCI combustion 76

3.5 Operating conditions used for the experiments to study the effect of intake air temperature on HCCI combustion 80

3.6 Operating conditions used for the experiments to study the effect of Boost pressure on HCCI combustion 83

4.1 Operating Parameters for RCCI Combustion mode 86

4.2 Error in estimation of FMEP 87

4.3 Coefficients for the Flynn- Chen Model 88

4.4 Operating conditions used for the experiments to study the effect of PR on RCCI combustion 109

4.5 Operating conditions used for the experiments to study the effect of PR on RCCI combustion 114

4.6 Operating conditions used for the experiments to study the effect of boost pressure on RCCI combustion 119

5.1 Operating Parameters for PPCI Combustion Mode 124

5.2 Error in estimation of FMEP 125

5.3 Coefficients for the Flynn- Chen Model 126

5.4 Operating conditions used for the experiments to study the effect of intake air temperature on PPCI combustion 138

5.5 Operating conditions used for the experiments to study the effect of intake pressure on PPCI combustion 144

5.6 Operating conditions used for the experiments to study the effect of SOI on PPCI combustion 151

A.1 Steady State Tests-Optimized 182

A.2 Steady State Tests-$T_{intake} = 40$ ° C 184

A.3 Steady State Tests-$T_{intake} = 60$ ° C 186

A.4 Steady State Tests-$T_{intake} = 80$ ° C 188

A.5 Steady State Tests-$T_{intake} = 100$ ° C 190

A.6 Steady State Tests-Optimized at naturally aspirated conditions . . . 193

A.7 Steady State Tests-Optimized at Boosted conditions 195

A.8 Steady State Tests-Boosted-Optimized 198

C.1 Experimental data files 205

C.2 Experimental data files organized in excel 206

C.3 Origin Project files 206

C.4 DSPACE Raw Data for all experiments 207

C.5 Labview Raw Data for all experiments 208

C.6 ACAP Raw Data for all experiments 209

C.7 Matlab Scripts for post processing the data 210

C.8 Figure files included in this thesis 211

C.9 Figure files included in this thesis (Contd.) 212

C.10 Figure files included in this thesis (Contd.) 213

C.11 Visio Figure files in this thesis 214

C.12 Project files for testing and data acquisition 215

Preface

A small portion of this thesis are based on one journal paper [4] and one conference paper [5]. The contribution of the author of this thesis and the contributions of the co-authors for each of the papers are as follows:

Contribution for Chapter 2 [4]: Engine setup, data collection, analysis of experimental data and writing the section for experimental setup have been done by the author of this thesis, K. Kannan. The artificial neural network (ANN) model (not included in this thesis) and validation of the model have been done by Dr. B. Bahri. Dr. M. Shahbakhti and Dr. A. A. Aziz provided technical comments and manuscript editing during the course of this paper.

Contribution for Chapter 5 [5]: Engine setup, data collection and analysis of experimental data have been done by Dr. S. Polat and the author of this thesis, K. Kannan. The author of this thesis is also responsible for the write up for the abstract, introduction and experimental setup sections for this paper. The figures and write up for the effect of boost pressure on PPCI combustion and performance characteristics have been done by Dr. S. Polat and Dr. A. Uyumaz. Valuable technical comments and manuscript editing have been done by Dr. M. Shahbakhti and H. S. Yucesu.

Acknowledgments

With great pleasure, I take this opportunity to express my gratitude to the many people who have helped or supported this work.

First, I wish to thank my advisor Dr. Mahdi Shahbakhti for giving me this opportunity to be a part of his research team at MTU. I am extremely grateful to him for believing in my abilities and shaping this thesis to "perfection". I would also like to thank Dr. Scott Miers and Dr. Youngchul Ra for being a part of my thesis defense committee.

I would like to thank the EML group for assisting me in completing my tasks. I would like to thank Seyfi, Mehran and Hamit for helping me understand the research ethics and for providing valuable technical advice. I would also like to appreciate Jayant, Nithin and Jayadev for helping me in developing the experimental test cell and conducting experiments. I truly appreciate your hard work, it would have never been possible without your efforts.

I would like to thank Paul, Jeremy, Chris and Steve for their advice, knowledge and patience for helping me understand several tasks of my projects. I highly appreciate Akshat, Karan, Nithin and Jayant for helping me editing my draft.

Last but not the least, I would like to thank my parents for providing me with this opportunity to pursue my MS degree in the US. I also thank my parents and sister for their love and for being a pillar of support during all stages of my life. Special thanks to Aishwarya for being such a huge motivation in my life. I appreciate the encouragement I have received from Rakesh, Dheeraj, Vijay and Akshay through all these years. My friends Avinash, Ram, Roshini, Muralee and Kavitha have played an instrumental part of this journey. I thank you for the good times.

List of Abbreviations

Acronyms

aBDC	After Bottom Dead Center
aTDC	After Top Dead Center
BDC	Bottom Dead Center
CAD	Crank Angle Degree
CAI	Controlled Auto-Ignition
CA50	Crank Angle for 50% of the cumulative heat release rate
CI	Compression Ignition
CO	Carbon Monoxide
DI	Direct Injection
EGR	Exhaust Gas Recirculation
EOC	End of Combustion
EPA	Environmental Protection Agency
EVC	Exhaust Valve Closing
EVO	Exhaust Valve Opening
exh	Exhaust
GDI	Gasoline Direct Injection
GDICI	Gasoline Direct Injection Compression Ignition

HCCI	Homogenous Charge Compression Ignition
HEV	Hybrid Electric Vehicle
HTR	High Temperature Region
HTHR	High Temperature Heat Release
ICE	Internal Combustion Engine
IMEP	Indicated Mean Effective Pressure
ISFC	Indicated Specific Fuel Consumption
IVC	Intake Valve Closing
IVO	Intake Valve Opening
LTC	Low Temperature Combustion
MABX	Micro Auto Box
MAP	Manifold Absolute Pressure
NO_x	Nitrogen Oxides
RON	Research Octane Number
PPCI	Partially Premixed Compression Ignition
PFI	Port Fuel Injection
PI	Proportional Integral
PID	Proportional Integral Derivative
PM	Particulate Matter
PPM	Parts Per Million
PR	Premixed Ratio

PRF	Primary Reference Fuel
RCCI	Reactivity Controlled Compression Ignition
RMSE	Root Mean Square Error
rpm	Revolution per Minute
SI	Spark Ignition
SOC	Start of Combustion
SOI	Start of Injection
STD	Standard Deviation
TDC	Top Dead Center
THC	Total Hydrocarbon
UDDS	Urban Dynamometer Driving Schedule
uHC	Unburned Hydrocarbon
VFD	Variable Frequency Drive
VVA	Variable Valve Actuation

Symbols

A	Area (m^2)
AFR	Air Fuel Ratio (-)
BSFC	Brake Specific Fuel Consumption ($\frac{g}{kW.h}$)
$BMEP$	Brake Mean Effective Pressure (kPa)
$\bar{C}_v$	Average Constant-volume Specific Heat Capacity ($\frac{kJ}{kg.K}$)
C_p	Constant Pressure Specific Heat Capacity ($\frac{kJ}{kg.K}$)

CA50	Crank Angle for 50% CHRR (CADaTDC)
COV	Coefficienct of Variation (%)
E	Total Energy (kJ)
EGR	Exhaust Gas Recirculation Fraction (-)
η	Efficiency (%)
F	Force (N)
$FMEP$	Friction Mean Effective Pressure (kPa)
h	Convective Heat Transfer Coefficient ($\frac{W}{m^2K}$)
IMEP	Indicated Mean Effective Pressure (kPa)
ISFC	Indicated Specific Fuel Consumption ($\frac{g}{kW.h}$)
λ	AFR over Stoichiometric AFR (-)
LHV	Low Heating Value (kJ/kg)
m	Mass (g)
LPP	Location of Peak Pressure (CAD aTDC)
MPRR	Maximum Pressure Rise Rate (bar/CAD)
$\dot{m}$	Mass Flow Rate (kg/s) or (g/s)
N	Engine Speed (rpm)
NO_x	Nitrogen Oxides Concentration (ppm)
n	Ratio of Specific Heat Capacities (-)
n_c	Compression Polytropic Index (-)
ω	Rotational Speed ($\frac{rad}{s}$)

RON	Research Octane Number (-)
P	Power (kW)
T	Temperature (° C/K)
W	Work (J)

subscripts

th	Thermal
ind	Indicated
exh	Exhaust
comb	Combustion

Abstract

A continuous investigation on the improvement of internal combustion engines is necessary due to the stringent emission and fuel economy regulations. Low Temperature Combustion (LTC) is a promising field of research since it can simultaneously reduce NO_x and soot while attaining high thermal efficiencies in automotive engines. A thorough study of several LTC regimes is necessary to understand the quantitative comparison and the extent of feasibility of these regimes functioning on an automotive engine. This thesis concentrates on an experimental investigation of three different LTC modes namely Homogeneously Charged Compression Ignition (HCCI), Partially Premixed Compression Ignition (PPCI) and Reactivity Controlled Compression Ignition (RCCI) on a 2.0-liter 4-cylinder gasoline engine.

A detailed experimental study of the LTC regimes with over 2,500 data points on a GM 2.0 L Ecotec engine is performed to study the relationship among the engine variables, combustion and performance characteristics. The operating range extension of the engine for lean limit and load limit while functioning in each combustion mode is discussed through operating region maps. Performance metric maps for indicated specific fuel consumption (ISFC), brake specific fuel consumption (BSFC), thermal efficiency and exhaust temperature are developed and discussed. The optimized maps are developed for each LTC regime considering the best ISFC at each speed-load

condition. Moreover, the behavior of the engine for each combustion mode is investigated and discussed through the trends observed for combustion phasing (CA10, CA50, CA90 and BD) and performance metrics (IMEP, indicated thermal efficiency, combustion efficiency).

The results show that the RCCI combustion mode offers the best indicated thermal efficiency of 47% among the three LTC modes. The Start of Injection (SOI) of n-heptane is found as a dominant factor in order to determine the optimal combustion phasing. The results of a comparative study indicate that HCCI is more suitable for running the engine at low loads, PPCI for low-mid loads and RCCI for mid-high loads.

Chapter 1

Introduction

Over the past two decades, the demand for highly fuel efficient vehicles has increased significantly, owing to the constantly changing emission standards and environmental concerns. New engine technologies are being explored to enhance thermal efficiency and minimize fuel consumption in engines. Automotive manufacturers are trying to comply with emission standards which are designed by environmental legislators and also provide low fuel consumption and high performance engines for customers. Therefore, many experimental and numerical studies were carried out by researchers on these issues. The studies have focused on improving combustion efficiency of internal combustion engines, reduction in emissions and use of alternative fuels [6, 7, 8].

Figure 1.1 represents the soot and NO_x regions for different combustion modes as a plot of local equivalence ratio vs local temperature. It can be seen that the lower equivalence ratio results in higher NO_x while higher equivalence ratios lead to soot formation. The challenge that researchers currently face is to reduce the soot and NO_x emissions, simultaneously. In order to accomplish this, a number of combustion regimes have been explored. NO_x formation occurs at temperatures higher than 2000 K. Therefore, with a decrease in in-cylinder temperatures and avoiding rich local zones, the problem of soot and NO_x emissions could be eliminated to a fair extent.

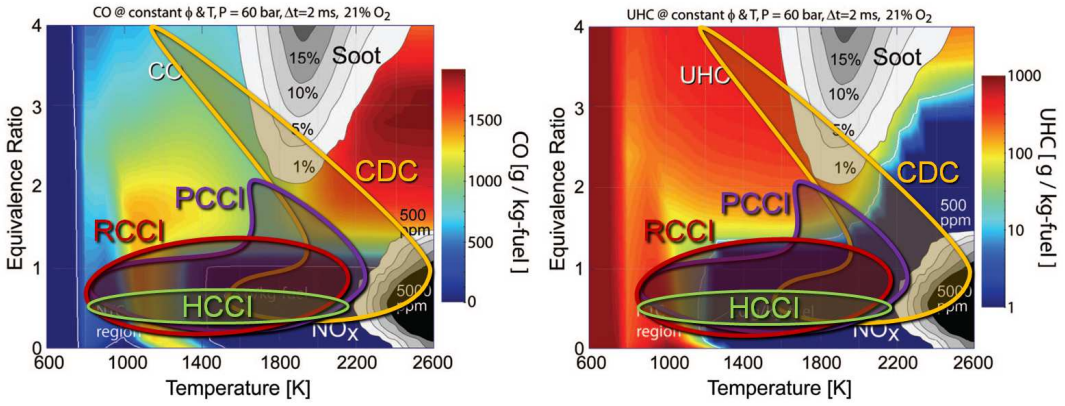

Figure 1.1: Contour plots of soot, NO_x, HC and CO depicting the operating regions of several combustion regimes [1] (Letter of permission D.1)

Low temperature combustion techniques such as HCCI, PPCI and RCCI have proven to be promising alternatives to the conventional Spark ignition and diesel combustion engines beacause of their ability to reduce the in-cylinder local temperatures and the rich zones simultaneously. In all the three LTC modes, the injection of fuel is either

in the port or early during compression stroke in the cylinder. This results in the fuel being premixed, hence avoiding the local rich zones in the cylinder. Moreover, RCCI combustion can be accomplished with split injections over a time period in a cycle, which results in better homogeneity of the air-fuel mixture [9]. Considering this factor, it is of prime importance to reduce the need for aftertreatment systems, while achieving high engine efficiencies.

This chapter describes the evolution of LTC engines explaining their evolution, background, advantages and challenges. It also outlines the operating principle of HCCI engines. Moreover, the research goals and scope of the study are introduced.

1.1 The evolution of Low temperature Combustion (LTC) engines

Spark ignition (gasoline) engines are one of the commonly used IC engines in commercial automobiles these days. Spark ignition engines do not use very high compression ratio due to knock limit and therefore the thermal efficiency is lower in these engines. Also in the spark ignition engines, speed and load conditions are controlled by throttling fresh cylinder charge which results in throttling loss. Cylinder charge in spark ignition engines is homogenous because fuel and air are mixing in intake port. Combustion phenomena in spark ignition engines encompass flame propagation which is

initiated by the spark plug. Since fuel and air are taken into the cylinder together, the fuel sticks on the cylinder wall and piston cavity. Consequently, oxidation is not fully done on these surface and unburned hydrocarbon (HC) emissions are high in spark ignition engines. [6] Compression ignition (diesel) engines are another type of internal combustion engines that are used widely nowadays. High compression ratio is used in these engines which result in high thermal efficiency. There are no throttling losses due to the fact that fuel is sprayed directly into the cylinder. Adverse aspect of compression ignition engines is heterogeneous cylinder charge which is caused by subsequent fuel addition to air inside the cylinder. Nitrogen oxides (NOx) and soot (PM) emissions are high in diesel engines. [7]

Homogeneous charge compression-ignition engines have advantages of spark ignition engines as well as benefits of compression ignition engines. The homogeneous air-fuel mixture is taken into the cylinder without throttling losses. This homogeneous mixture undergoes simultaneous self-ignition throughout the cylinder without the flame propagation while being compressed by piston. Thus the combustion efficiency is higher and the heat transfer losses are lower due to shorter combustion duration. Also thermal efficiency is high because of high compression ratio implementation in these engines. Considering these characteristics we can conclude that HCCI engines provide high thermal efficiency while emitting very low levels of NOx and PM [6, 7, 8]. However, HCCI engines suffer from some problems and commercial use of these engines needs resolution of these weak points which are related to ignition timing and

the combustion rate control. These two problems are difficult to overcome. First, there is no mechanism for ignition timing control similar to spark in spark ignition engines or injection timing in direct injection engines. Second, chemical reaction's dependence on the fuel properties is more dominant in HCCI engines than spark ignition and diesel engines. HCCI engines face with issues such as misfire at low load and knocks at high load. Therefore, HCCI engines have a limited operating range [8]. Recently, many studies have been carried out about the potential control methods as intake air heating [10, 11], variable compression ratio [12, 13], variable valve timing [14, 15] and EGR system [16, 17], etc. Most of studies have focused on the effects of physical and chemical properties of different alternative fuels to control HCCI combustion [6, 18, 19]. In these studies, the important results were obtained about control of the HCCI combustion process. However, satisfactory result was not gained at high-load operation of HCCI engines due to lack of a direct method to control combustion phasing. Another way to overcome the disadvantages of HCCI engines is application of dual mode engine as HCCI/SI engine. A dual-mode HCCI/SI engine is equipped with variable valve timing and ignition system, that can operate in HCCI mode at low and medium load, while operates in SI mode at high load when necessary. In contrast, transition between modes is not acceptably stable especially from SI mode to HCCI mode. It is necessary to make further improvements on controlling strategies in order to eliminate between cycle to cycle variations. Generally, HCCI and SI operation are combined for obtaining the best performance in double-mode

engine [20, 21].

In order to overcome the difficulty of combustion phasing control in HCCI, an alternative LTC mode called Partially Premixed Compression Ignition (PPCI) was introduced in 2005 [22, 23]. Unlike HCCI, the fuel was premixed in a fuel tank (in a desired ratio based on the RON) and was injected directly into the engine cylinder using direct injection. The tests were performed on a boosted Diesel engine with high EGR rates. This type of combustion is more suitable for high octane fuels, since the high volatility of gasoline enabled better mixing of the fuel and air after injection. In this study, a significantly lower fuel consumption, NOx and PM were observed. Extensive research has been conducted in order to understand the dynamics and combustion characteristics of PPCI combustion [5, 24]. An experimental and numerical investigation was performed on a light duty diesel engine to identify the characteristics of GDICI combustion. A parametric study was performed to analyze the feasibility of full load operation of the engine. It was observed that low-emission engine concepts could be extended to high octane high speed engine operation. Owing to the high volatility and octane number of gasoline, there was a significant reduction in the combustion temperatures and ultra-low NOx was achieved, while the ISFC was about 180 g/kW-h. It was also observed that the injection pressure had to be optimized in order to obtain an optimized operating map for a given load. It was observed that the maps were highly sensitive to EGR rate, boost pressure and intake air temperature. Moreover, increasing the intake air temperature and reducing the EGR rate had

very comparable effects on the operating map region [24]. The effects of boost pressure was investigated on PPCI combustion in an early direct injection HCCI engine through experimental methods. It was observed that intake manifold pressure had a significant effect on the operating range extension of the engine. The in-cylinder pressure increased and the combustion was advanced with boosting. Moreover, the best indicated thermal efficiency was obtained when the engine was run at a combustion phasing slightly after TDC. The peak thermal efficiency obtained was about 40 %, which is very much comparable to that of diesel engines. Moreover, higher engine loads could be achieved with higher boost pressures and the engine load boundary was extended significantly [5]. Partial fuel stratification is an approach that has been studied extensively ever since its inception. It has been observed that the auto-ignition knocking tendency could be reduced with PPCI [25, 26]. With this reduction in knock intensity, the combustion phasing control became much easier. As a result of this, higher thermal efficiencies could be attained at higher loads [27]. When partial fuel stratification was compounded with the introduction of reactivity of equivalence ratio stratification, it was possible to further precisely control the combustion phasing and the gradient of heat release [28]. The knock intensity was further reduced at mid-high load condition. This technique has been termed as reactivity controlled compression ignition (RCCI). It is a dual fuel combustion strategy that uses a higher reactivity fuel to be injected directly into the cylinder and the low reactive fuel to be injected in the intake manifold. It has been observed that with RCCI, the engine

operation region could be extended to high load condition, while attaining thermal efficiencies close to the conventional diesel combustion (CDC). The experiments were performed with pump gas 87 octane fuel as the low reactive fuel and ultra-low sulfur diesel as the high reactive fuel. While the MPRR was significantly reduced, indicating acceptable operating region without knock, the EPA 2010 standards for NOx and soot was also met [29]. With RCCI combustion, the gross thermal efficiencies could be escalated to 60 %, with simultaneous reduction in friction and pumping losses. Using an engine with a compression ratio of 18.6:1, a 50 % reduction in heat transfer losses and combustion losses were obtained. Moreover, the NOx and PM levels were near-zero. This shows that thermodynamic conditions and combustion parameters need to be optimized in order to extend the lean limit operation and higher thermal efficiencies at all test points. Moreover, improvement in supercharger efficiencies, low temperature of the exhaust and reduction in friction losses play a key role in attaining high gross efficiencies [30].

1.2 Principle of Operation of LTC engines

HCCI combustion has been an interesting field of research due to its ability to attain ultra low NO_x and near zero PM emissions. This can be achieved by firstly obtaining a homogeneous air-fuel mixture and then providing sufficient heat for the mixture to auto-ignite at the end of compression stroke. Achieving these tasks can prove to be

challenging. [31]

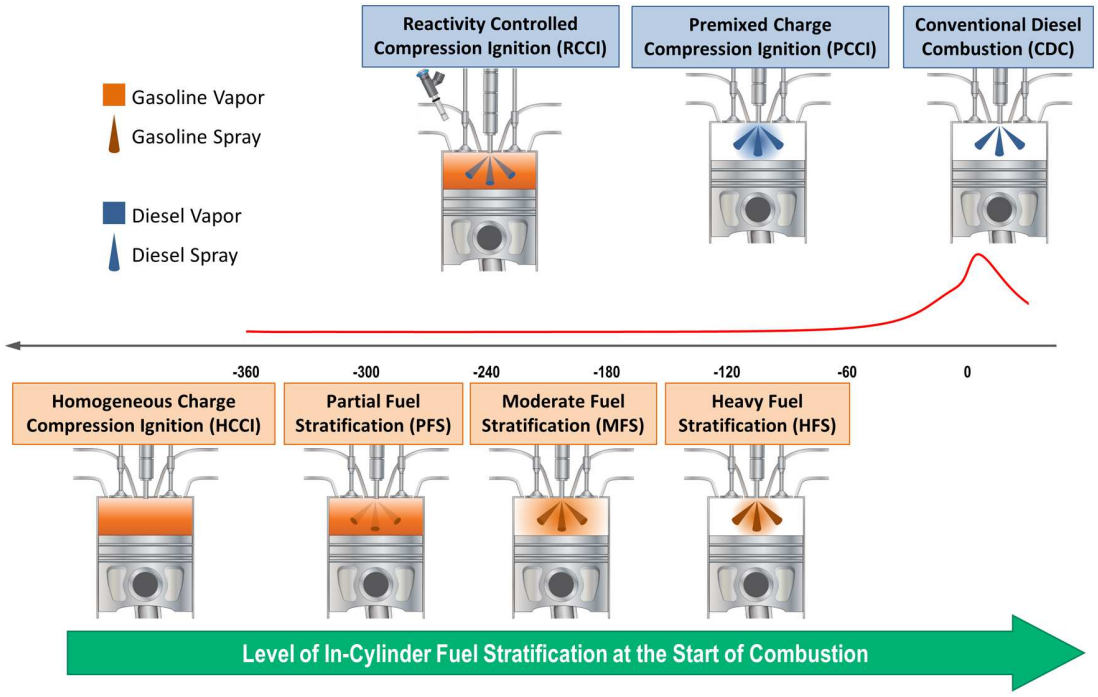

Figure 1.2: Comparison of diesel, Gasoline and HCCI engine [2] (Permission letter given in D.2)

If complete homogeneity is obtained for a mixture, there is a rise in temperature and pressure of the mixture during compression. This leads to auto-ignition of the mixture. However, this differs from a typical diesel CI. In case of HCCI the auto-ignition does not occur at a certain place in the cylinder, but simultaneously across the combustion chamber. Contrary to SI combustion, there is no high temperature flame front in HCCI during the auto-ignition of the mixture. This leads to reduced in-cylinder gas temperatures and lean mixtures, thereby reducing the NO_x formation to near-zero levels. Moreover, due to the absence of local rich zones in the cylinder, the soot emissions is also simultaneously reduced. [32] [33]. In a HCCI engine, the

fuel and air are premixed in the intake port, while in case of PPCI the mixture preparation happens in the cylinder, similar to Gasoline direct injection. The air-fuel mixture is compressed during the compression stroke and combustion is attained by auto-ignition of the mixture at the end of compression. In order to auto ignite the mixture at the end of compression stroke, the gas temperature at the start of compression has to be higher. This can be achieved by either pre-heating the intake air or by trapping residuals in the cylinder. As a result of this, the chemical reactions become more faster and catalyze the combustion process of the mixture. [34]

Although the start of main heat release usually occurs when the temperature reaches a value of 1050– 1100K for gasoline or less than 800K for diesel, many hydrocarbon components in gasoline and diesel undergo low temperature oxidation reactions accompanied by a heat release that can account for up to 10% of the total energy released. The heat release rate and combustion characteristics of HCCI combustion depends on several factors such as the chemical kinetics of the fuel used, dilution strategies used and the temperature-pressure history of the mixture during compression. [34]

While high efficiencies and ultra-low NO_x can be obtained using HCCI, it is limited to low loads and there is no direct means to control combustion phasing [35]. In case of RCCI, two fuels with different reactivities are used. The lower reactive fuel (typically iso-octane) is injected in the port and the higher reactive fuel (typically

n-heptane) is injected late directly in to the cylinder. The heat release for RCCI occurs in three stages: the cool flame, the PRF burn and the late burn. The first stage reaction occurs due to the n-heptane injection which corresponds to the cool flame. The first stage of HTHR occurs due to the PRF burn, where n-heptane and the entrained iso-octane combust resulting in a heat release. The final stage of heat release occurs due to the late burn of the lower reactive fuel i.e iso-octane. The changing fuel ratio results in the change of shape and the magnitude of heat release [36]. This is discussed elaborately in Chapter 4.

1.3 Research Goals and Scope of Research

Low temperature combustion is a promising alternative to conventional SI and CI engines, given the high gross efficiencies, while affirming to the EPA emission standards. However, the operating region for both the lean limit operation and load limit operation for all major LTC regimes on a same engine is not thoroughly discussed in literature. This research is one of its kind, given the fact that all three combustion modes: HCCI, PPCI and RCCI could be run on the same engine. Therefore, the thesis focuses on operating region extension for all three LTC modes, by adopting different techniques. The range of operation for each mode is individually studied and explained. The operating region maps for the load and speed are created. In order to understand the performance characteristics of the engine, maps for BSFC,

ISFC and net indicated thermal efficiency are developed. Moreover, it is important to understand the effect of operating conditions on the performance and combustion characteristics of the engine. Parameters such as engine speed, fuel-air equivalence ratio, intake air temperature, boost pressure, research octane number (RON) and fuel rail pressure were varied independently, one at a time, keeping other parameters constant. A parametric study was performed on the engine for each LTC mode independently under steady state conditions. Blends of n-Heptane and iso-Octane are used as the fuels. Since they are primary reference fuels and have an octane rating of 0 and 100, respectively, they are very similar to the octane rating of conventional diesel and gasoline, respectively. In the thesis, the term Research Octane Number (RON) is used for PPCI and HCCI combustion modes. However, the term premixed ratio (PR), the ratio of premixed fuel (iso-octane) to the total energy supplied, is used for RCCI mode. The ultimate goal of the project is to understand and evaluate thoroughly the operating region characteristics of each of the three combustion modes and parametric studies to understand the effect of operating conditions on the performance and combustion characteristics of the engine.

1.4 Organization of Thesis

This thesis is organized into six different chapters as represented in Figure 1.3. Chapter 1 gives an overview of background, evolution and principle of operation of LTC

engines. The research goals and scope of the thesis are discussed. Chapter 2 gives an overview of the experimental setup, instrumentation and calibration of the com-

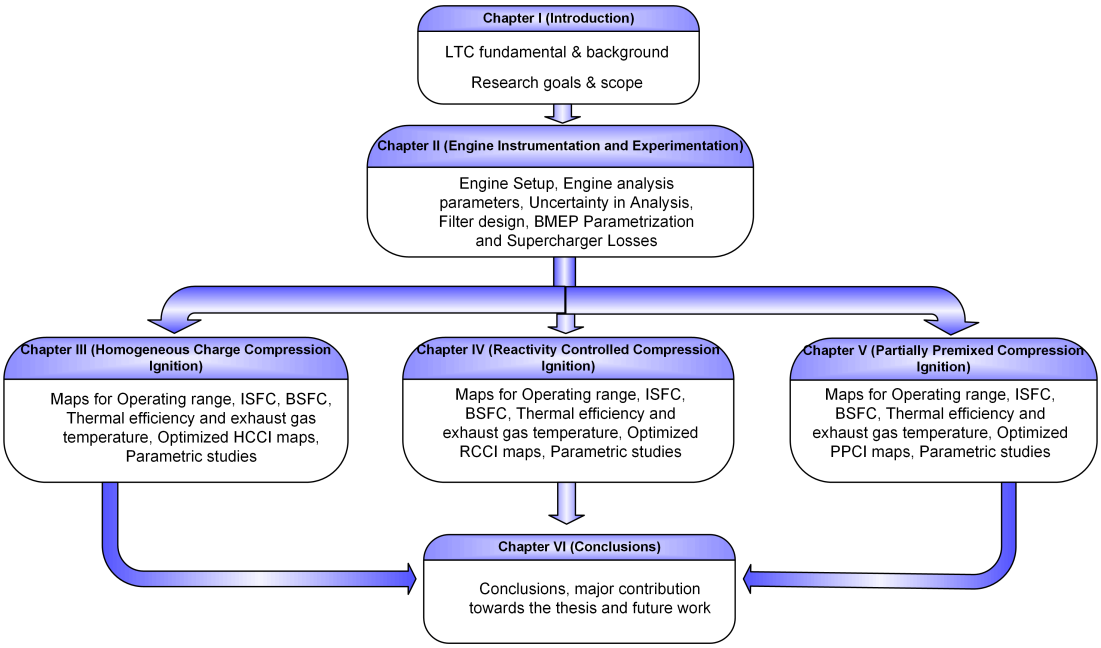

Figure 1.3: Thesis Organization

ponents involved. The calculations involved in the calculation of the engine analysis parameters are elaborated. Further, an uncertainty analysis of the dependent and independent parameters is discussed. Chapters 3, 4 and 5 discuss the results for three different combustion modes HCCI, RCCI and PPCI, respectively. In these three chapters, maps for operating regions, ISFC, BSFC, exhaust gas temperature and thermal efficiency were discussed. Moreover, optimized maps for each of these parameters were also developed. A parametric study of the effect of intake air temperature, boost pressure, RON and SOI were conducted and discussed. Finally, chapter 6 summarizes the results and significant contribution towards the thesis. It also provides

recommendations for the future research based on the results from this thesis.

Chapter 2

Engine Instrumentation and Experimentation

An experimental GDI engine was modified and instrumented to run in several LTC modes including HCCI, PPCI and RCCI. This chapter elaborates the contributions made to the instrumentation of the engine from this thesis.

2.1 Engine Setup and Specifications

Figure 2.1 shows the schematic of the experimental setup of the engine used for running tests in LTC modes. A GM 2.0 L 4-stroke, 4-cylinder Gasoline Direct Injection

Ecotec engine was used for this purpose. The specifications of the engine is shown in Table 2.1.

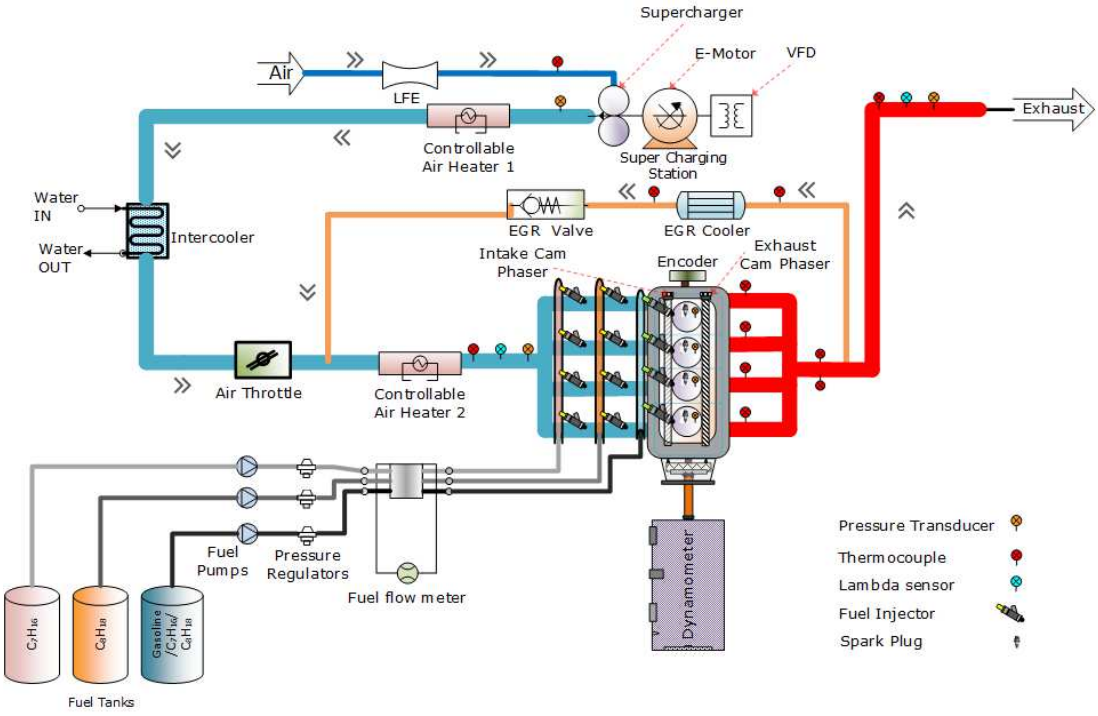

Figure 2.1: Schematic of the LTC engine setup

The turbocharger was disabled. Instead, an Eaton M62 supercharger driven by an external 20 hp e-motor was used. The e-motor was controlled remotely with a GS34040 Variable Frequency Drive (VFD) unit and dSpace MicroAutoBox. An external fuel pump was used to supply fuel at 3 bar pressure to the Port Fuel injectors. Two air heaters between the supercharging station and the intake manifold were used to preheat the intake air to the desired temperature. A 460 hp GE AC Dynamometer was used to control the speed and load of the engine. The mass flow rate of intake air was measured using Merriam MDT500 air flow measurement system [4]. The LTC

experimental setup is shown in Figure 2.2. More information with respect to the instrumentation of the engine can be obtained from the previous works [37, 38, 39]

Table 2.1
Engine Specifications

Engine Type	4 stroke, Gasoline
Number of Cylinders	4
Cylinder volume	1998 cc
Bore	86 mm
Stroke	86 mm
Compression ratio	9.2:1
Max engine power	164 @ 5300 (kW/rpm)
Max engine torque	353 @ 2400 (Nm/rpm)
Diameter of intake valves	35.17 mm
Firing order	1-3-4-2
IVO	25.5/-24.5 (CAD bTDC)
IVC	2/-48 (CAD bBDC)
EVO	36/-14 (CAD bBDC)
EVC	22/-28 (CAD bTDC)
Valve lift	10.3 mm

2.2 Port Fuel Injectors (PFI) Instrumentation, Calibration and Assembly

Eight Bosch EV14 port fuel injectors were used for the engine. The EV14 specifications are given in Table 2.2.

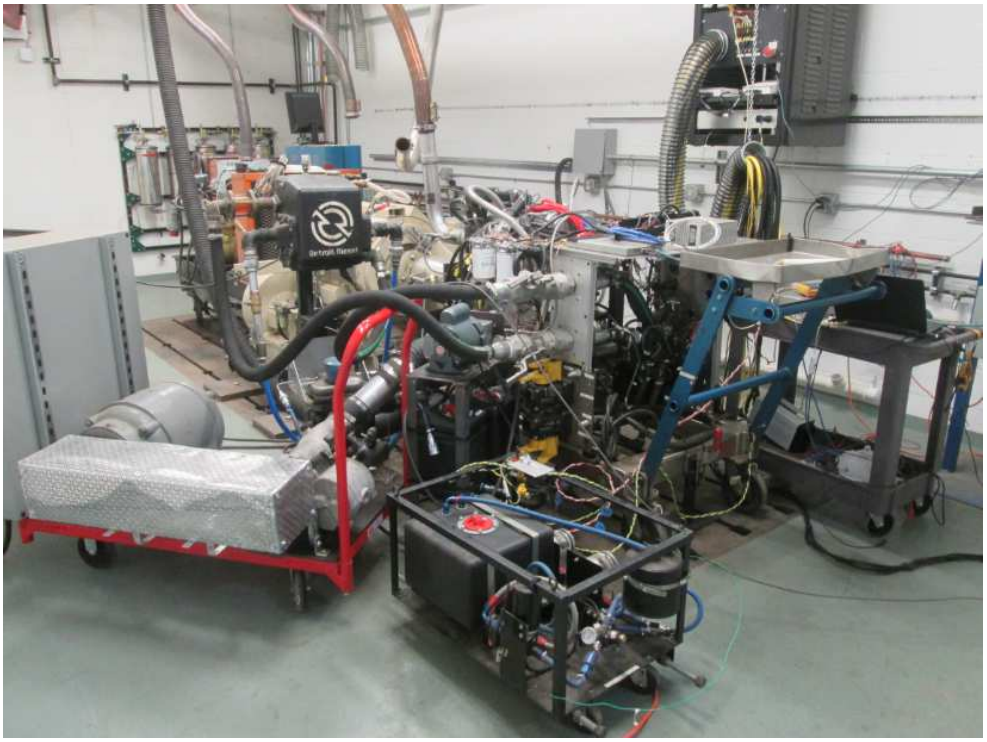

Figure 2.2: Experimental LTC Engine Setup

Table 2.2
Port Fuel Injector (Bosch EV14) Specifications

Part No.	0 280 158 116
Flow rate/min	237 g/min
Type	E
Housing	L
Resistance	12 ohm
Tilt angle	22°

Two Fuel Rails with four injectors were mounted on an interface which was then mounted on the intake manifold of the engine. Figure 2.3 shows the PFI assembly on the engine setup.

The port fuel injectors were controlled using a low side driver unit from Rapid Pro.

Figure 2.3: Port fuel injector assembly

A model as shown in Figure 2.4 was developed in Simulink for Injectors actuation and control. The injector control blocks resided in a sub-system triggered by an angle interrupt. In order to update the injection pulse pattern at run time, the angle value of the interrupt was set lower than the smallest angle value of the new injection pulse pattern. Figure 2.5 represents the display panel for the injectors control. The RON, injection start angle and the fuel mass are the inputs to the model. On the basis of this, the required pulse width is calculated for injectors on rail 1 (x1) and rail 2 (x2). a1, a2, b1 and b2 are the calibration factors for rails 1 and 2.

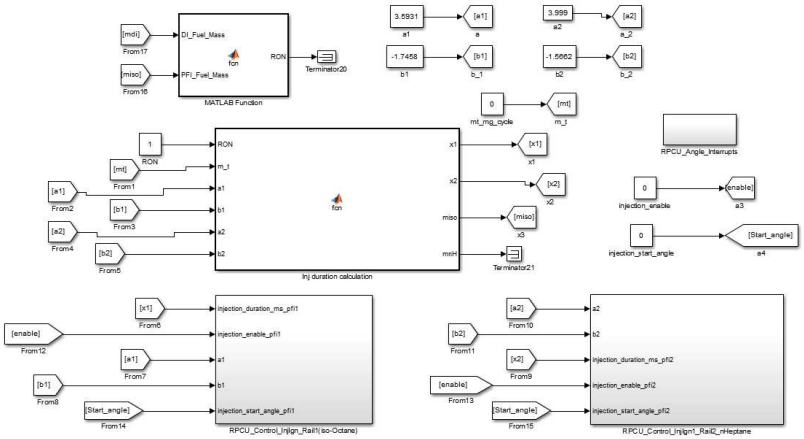

Figure 2.4: Triggered sub-system for PFI control

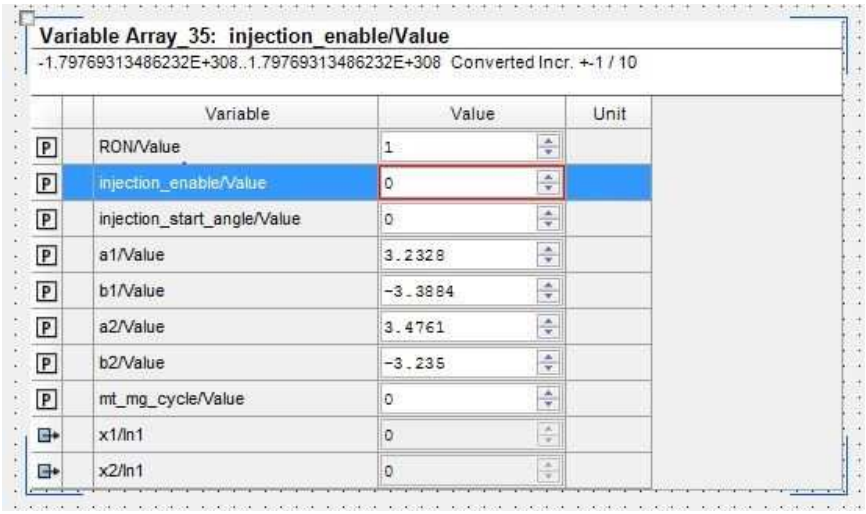

Figure 2.5: Monitoring Panel on dSPACE Control Desk for PFI Control

Low Temperature Combustion engines have the flexibility of being operated with different fuel combinations. For the experiments, iso-octane and n-heptane were blended volumetrically in different proportions so as to attain the desired research octane number (RON). As discussed in this section, the engine is equipped with two PFI rails with four injectors on each rail. The injectors on Rail 1 inject n-heptane while

injectors on Rail 2 inject iso-octane. The percentage of the injected isooctane and n-heptane determines the RON of the fuel. RON number can be regulated by changing the injection durations of the injectors. Therefore, there arises the need to estimate the amount of fuel injected for a given injection duration. This requires the calibration of the PFI injectors for different fuel types because each fuel has a different density value. Micro Motion 1500 transmitter and CMF050 flow sensor were used for the calibration of the PFI injectors. Injected fuel mass was measured via Prolink III software. Prior to the calibration of PFI injectors, the accuracy of the new fuel flow meter was tested using DI injectors which were previously calibrated. Figure 2.6 illustrates the verification result for DI injectors. The average error was determined to be 0.27 mg/cycle that corresponds 1 %.

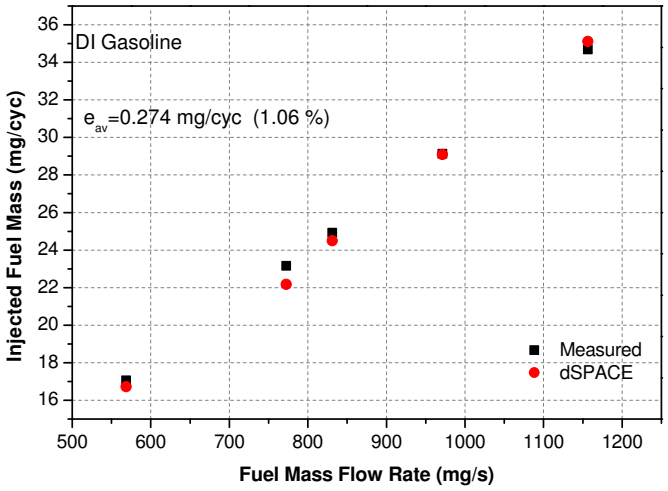

Figure 2.6: Verification of dSPACE model for calculating injected fuel mass from using DI injectors

Figure 2.7(a) illustrates the calibration of the PFI injectors for iso-octane fuel. In order to calibrate the injectors, one of the rail lines was connected to the fuel tank which contained iso-octane. The engine was run at 1000 rpm and injection durations were changed between 3 ms and 11 ms. The mass of fuel injected was measured for two minutes for every injection duration value. The gain and offset values were then determined and a polynomial was fitted as shown in Figure 2.7(a). Figure 2.7(b) illustrates the verification of the calibration of PFI injectors for iso-octane fuel. For mass flow rate of fuel greater than 100 mg/s, an average error of 0.05 mg/cycle was obtained. It was observed that the error increased significantly below 100 mg/s. This can be attributed to the non-linear characteristics of the injector at very low Fuel flow rates. However, for practical applications, the minimum injection duration will be greater than 3 ms. Therefore, this calibration factors hold good. The PFI injectors were also calibrated for n-heptane fuel and the same procedure was followed. Figure 2.2.8(a) and Figure 2.8(b) show the calibration and verification of the calibration for n-heptane, respectively.

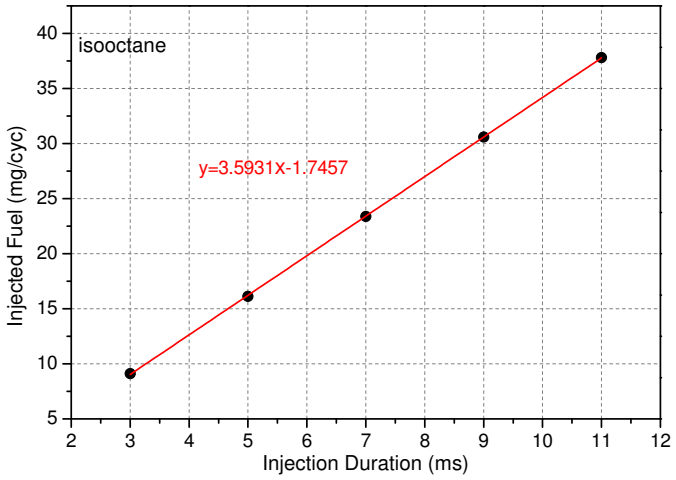

(a) Calibration

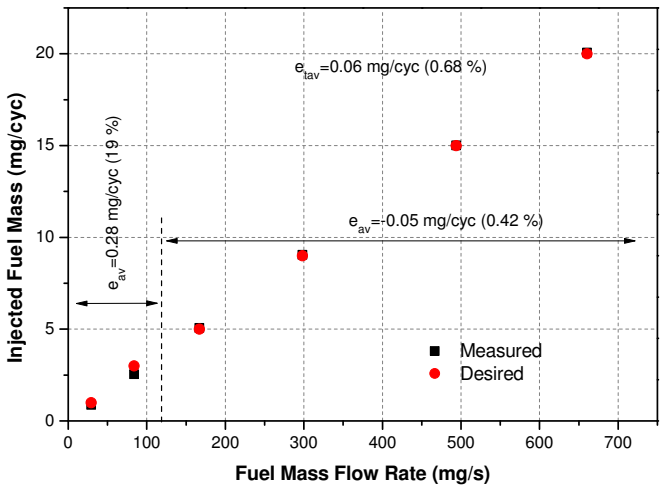

(b) Verification

Figure 2.7: Calibration and Verification of the PFI injectors for Iso-Octane fuel

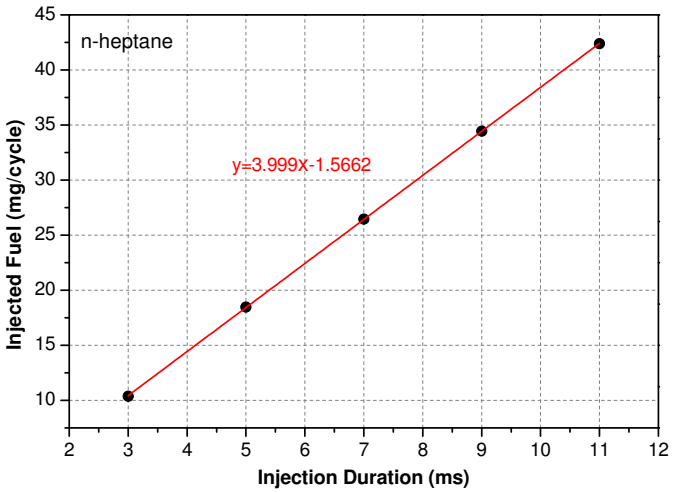

(a) Calibration

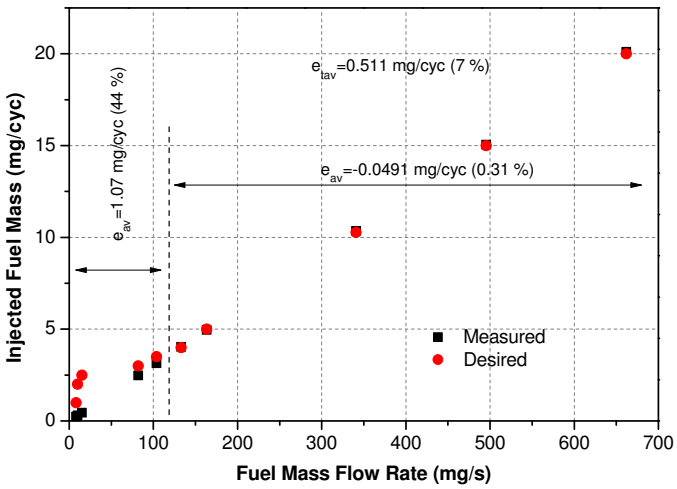

(b) Verification

Figure 2.8: Calibration and Verification of the PFI injectors for n-Heptane fuel

2.3 Supercharger control using dSpace

The supercharger can either be controlled manually using the VFD unit or remotely by supplying an analog voltage between 0-10 V. The former method requires the user to manually change the frequency of the e-motor to attain the desired boost pressure. Supercharger VFD unit runs with a voltage range of 0-10 V. The user changes the frequency of the VFD unit and the VFD controller decides the voltage that needs to be supplied to run the e-motor at a given speed. The correlation between the terminal voltage and the operating frequency of the e-motor is given in Equation (2.1).

$$V = \frac{\nu}{f_{sys}} f_o \tag{2.1}$$

Where V is the terminal voltage, f_{sys} is the operation frequency of the system and f_o is the actual operating frequency of the e-motor.

The manual speed setting method is not time efficient and user friendly. Moreover, it is not applicable when the engine needs to be tested for transient conditions. Therefore, the latter method was developed and the supercharger was controlled and monitored using dSpace MicroAutoBox (MABX). MABX can supply analog voltage in the range of 0-4.75 V. Therefore, a voltage multiplier circuit was designed in order

to amplify the voltage from 0- 4.75 V to 0- 9.5 V. A schematic of the VFD with the phase monitor relay is depicted in Figure 2.9

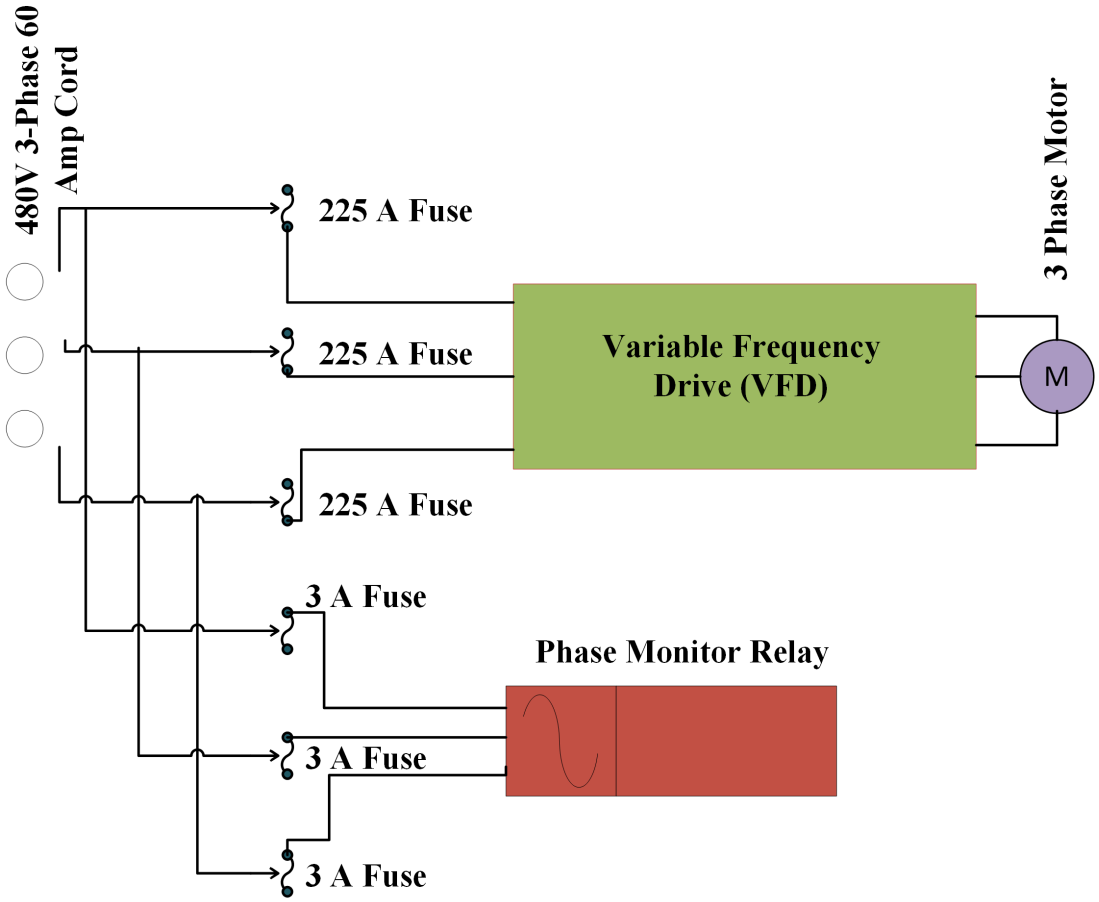

Figure 2.9: Supercharger VFD unit

In order to determine the required terminal voltage for a given boost pressure, two frequency maps with engine speed as a function of boost pressure were developed by operating the supercharger manually. These maps were then used as a lookup table in the Matlab Simulink model. Frequency maps were obtained for intake valve opening (IVO) of -24.5 and 25.5 CAD bTDC. Figure 2.10 illustrate the frequency maps for

-24.5 and 25.5 CAD IVO bTDC.

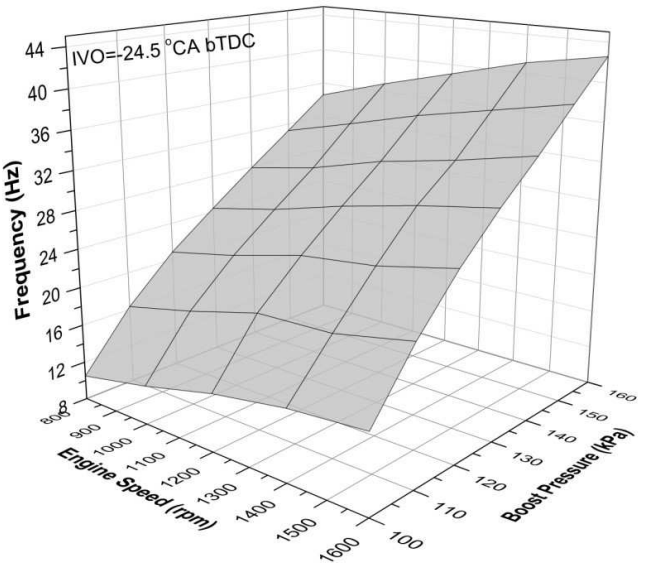

(a) IVO = -24.5 CAD bTDC

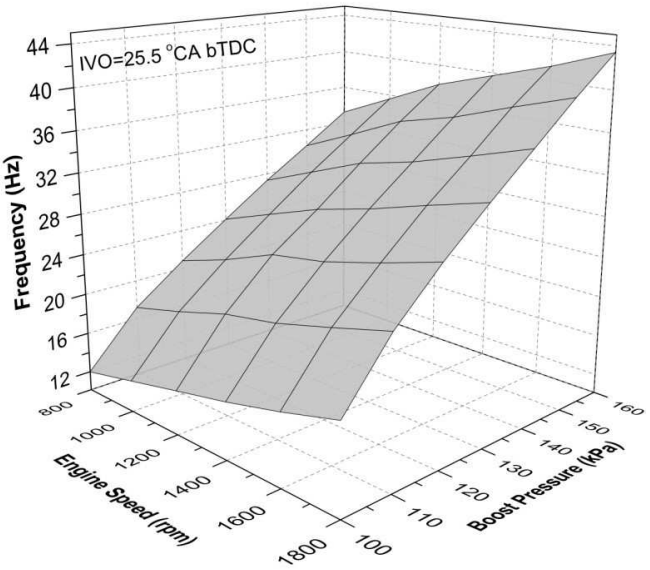

(b) IVO = 25.5 CAD bTDC

Figure 2.10: Supercharger Frequency maps for IVO of a) -24.5 CAD bTDC and b) 25.5 CAD bTDC

Figure 2.11 shows the Matlab Simulink model developed for the MABX to supply the necessary terminal voltage to the VFD. The required frequency is determined from the look-up table. The desired manifold pressure is commanded by the user via dSpace control desk interface. Figure 2.12 shows the screenshot of the supercharger user control panel on the control desk interface. The model gets the instantaneous engine speed from the crank position sensor and frequency was determined from the look-up table. Determined frequency is converted to the voltage value by means of desired gain2 in the model. MicroAutoBox supplies the voltage in terms of duty cycle (in the range of 0-1). Therefore, the calculated voltage is converted to the duty cycle level via desired gain 3 in the model.

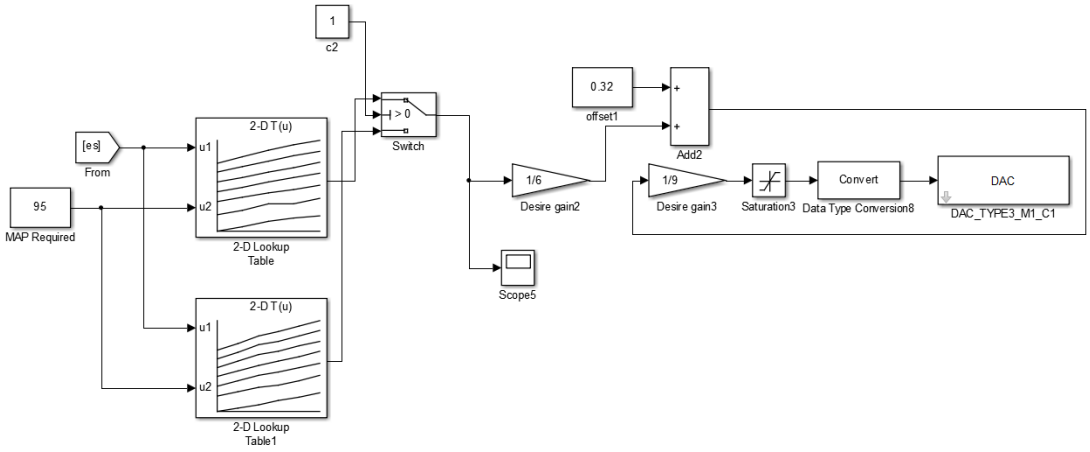

Figure 2.11: Simulink Model for Supercharger Control using dSpace

The Supercharger Control using dSpace has a mean error of 1.2 kPa between the set desired manifold pressure and the output boost pressure. This difference resulted from the variable resistance of the electrical circuitry between the VFD and MABX.

In order to compensate for the decrease in voltage, an average offset value of 0.32 V was used. Although there is a slight difference between the desired and actual values of MAP, the error was less than 1%.

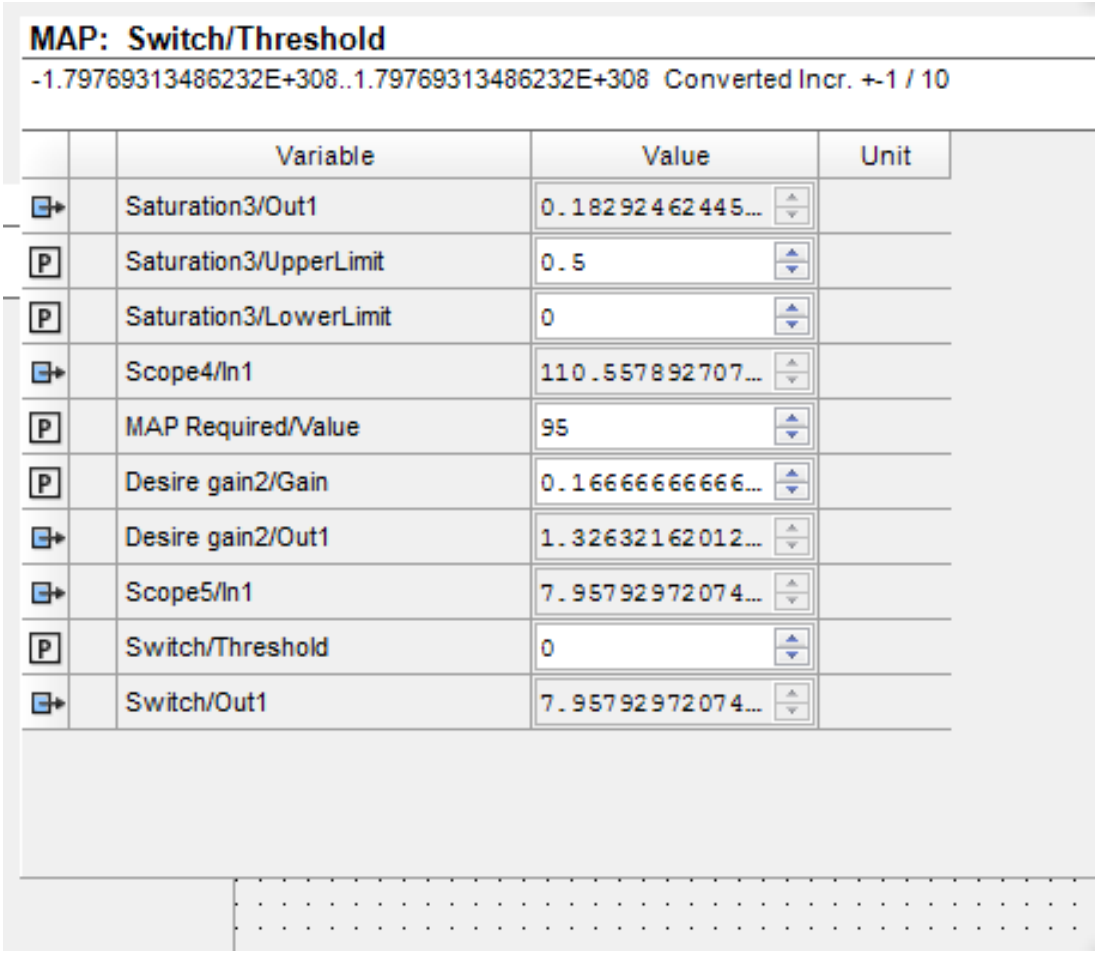

Figure 2.12: Supercharger User Control panel on dSpace control desk

2.4 Engine Analysis Parameters

A MATLAB code was developed for the combustion analysis. Data from dSpace, LabVIEW and ACAP were synchronized on a time basis and were used as the input to the code. The outputs of the code were the averaged in-cylinder pressure trace, average brake mean effective pressure, average intake manifold absolute pressure, piston displacement relative to the crank angle, instantaneous cylinder volume, stroke volume, combustion chamber volume, volumetric efficiency, lambda, equivalence ratio, maximum pressure rise rate (MPRR), gross work, indicted mean effective pressure (IMEP), Coefficient of Variance (COV) of indicated mean effective pressure, expansion and compression polytropic index, in-cylinder temperature prediction, heat transfer, heat release rate, cumulative heat release rate, CA10, CA50, CA90, fuel mass burn fraction, combustion duration, thermal efficiency, combustion efficiency, effective power, effective torque, effective specific fuel consumption, indicated power, indicated torque, indicated specific fuel consumption and mechanical efficiency.

2.4.1 Engine Geometry

Cylinder volume and first derivative of cylinder volume must be computed versus crank angle in order to calculate net work, heat release rate, indicate mean effective

pressure, amount of heat transfer and some engine performance parameters.

The displacement volume, combustion chamber volume and the total cylinder volume were computed using Equations 2.2, 2.3 and 2.4, respectively.

$$V_s = \pi \frac{D^2}{4} H \tag{2.2}$$

$$V_c = \frac{V_s}{CR - 1} \tag{2.3}$$

$$V_{total} = V_s + V_c \tag{2.4}$$

Where V_s is the displacement volume (m^3), V_c is the combustion chamber volume (m^3), V_{total} is the cylinder volume (m^3), D is the cylinder bore (m), H is the stroke length (m) and CR is the compression ratio.

The instantaneous piston displacement can be calculated using Equation 2.5.

$$S = L + r - r\,cos\theta - L\,cos\beta \tag{2.5}$$

The term cosθ can be expressed in terms of crank angle θ as shown in the set of equations below [40].

$$L\,sin\beta \;=\; r\,sin\theta \tag{2.6}$$

$$sin\beta \;=\; \frac{r}{L}\,sin\theta \tag{2.7}$$

$$sin^2\beta + cos^2\beta \;=\; 1 \tag{2.8}$$

$$cos\beta \;=\; \sqrt{1 - sin^2\beta} \tag{2.9}$$

$$cos\beta \;=\; \sqrt{1 - (\frac{r}{L}\,sin\theta)^2} \tag{2.10}$$

From Equation 2.5 and 2.10, the following correlation for piston displacement is obtained [40].

$$S(\theta) \;=\; L + r - r\,cos\theta - L\sqrt{1 - (\frac{r}{L}\,sin\theta)^2} \tag{2.11}$$

$$S(\theta) \;=\; r(1 - cos\theta) + \frac{1}{\lambda} - \sqrt{\frac{1}{(\lambda)^2} - sin^2\theta} \tag{2.12}$$

Where L is the connecting rod length (m), r is the diameter of the crankshaft (m), λ is the ratio of diameter of the crankshaft to the connecting rod length, θ is the angle of the crank shaft (deg), and S(θ) is the instantaneous displacement of the piston with respect to the crankshaft angle (rad).

The instantaneous cylinder volume with respect to the crank angle is given in Equation 2.13.

$$V \;=\; V_c + \pi\,\frac{D^2}{4}\,S(\theta) \tag{2.13}$$

The first derivative of instantaneous cylinder volume is given in Equation 2.14.

$$\frac{dV}{d\theta} \;=\; \pi\,\frac{D^2}{4}\,r\,(sin\theta + \frac{cos\theta\,sin\theta}{\sqrt{(\frac{1}{\lambda^2} - sin^2\theta)}}) \tag{2.14}$$

2.4.2 Net Work and Mean effective pressure

The work and indicated mean effective pressure (IMEP) can be calculated for each cycle using in-cylinder pressure data. IMEP values can be used in determining the engine efficiency since IMEP values are independent of the cylinder volume, cylinder number and engine speed.

Pressure data for the gas in the cylinder over operating cycle of the engine can be used to calculate the work transfer from gas to the piston. The cylinder pressure and corresponding cylinder volume throughout the engine cycle can be shown on a P-V diagram. The indicated work per cycle is obtained by the area under the curve on the PV diagram.

$$W = \oint P \, dV \tag{2.15}$$

Where, W is work (Joule), P is cylinder pressure (Pa) and dV is displaced volume (m^3). There are two ways of defining the work done per cycle. Gross indicated work per cycle W_{gross}; work delivered to the piston over the compression and expansion stroke only. Net indicated work per cycle W_{net}; work delivered to the piston over the entire four stroke cycle. W_{gross} = (area A + area B) and W_{net} = (area A + area C)

- (area B + area C) = (area A - area B), where each of these areas is regarded as a positive quantity. Area B + area C = work transfer between the piston and the cylinder gases during the inlet and exhaust strokes and is called the pumping work (W_{pump}). In case of naturally aspirated engines, the pumping work transfer will be to the cylinder gases because the pressure during the inlet stroke is less than the pressure during the exhaust stroke [41]. The pumping work transfer will be from the cylinder gases to the piston if the exhaust stroke pressure is lower than the intake pressure, which is normally the case with highly loaded turbocharged engines. Net work is equal to area A - area B.

$$W_{net} = W_{gross} - W_{pump} \tag{2.16}$$

$$IMEP_{gross} = \frac{W_{gross}}{V_k} \tag{2.17}$$

$$IMEP_{net} = \frac{W_{net}}{V_k} \tag{2.18}$$

2.4.3 Polytropic Index

The polytropic index remains constant during the compression and expansion process but it changes during the combustion process. Start and end of combustion can be determined through keen observation of polytropic index. The polytropic index during compression and expansion stroke can be expressed as follows:

$$P\,V^{n_c} = C \tag{2.19}$$

$$n_c\,P\,V^{n_c-1}dV + dP\,V^{n_c} = 0 \tag{2.20}$$

$$n_c = -\frac{V\,dP}{P\,dV} \tag{2.21}$$

2.4.4 Combustion Stability

Combustion stability is defined in terms of Coefficient of Variation of the Net IMEP. Compared to traditional S.I. engines, the initiation of HCCI combustion and the

following heat release process are controlled by the chemical reaction rates, which depend on the temperature, pressure and mixture properties including fuel composition, air/fuel ratio and EGR rate. Numerous factors that influence the mode and extent of cycle-to-cycle variation have been identified. These include fluctuations in the following parameters and factors: (1) intake temperature and pressure; (2) intake air/fuel ratio or fuel flow rate; (3) coolant and lubrication oil temperatures; (4)the presence of diluents as a result of either external or internal EGR; (5) thermal and mixture composition stratification as results of in-homogeneity; (6) the intensity of intake charge motion and bulk turbulence; (7) the completeness of combustion in the preceding cycle; and (8) fuel mixing system and homogeneous mixture formation strategies [16], [42].

The COV_{IMEP} is calculated by:

$$COV_{imep}(\%) = \frac{\sigma_{imep}}{\mu_{imep}} x100 \tag{2.22}$$

where σ_{imep} is the standard deviation of IMEP and μ_{imep} is the mean in IMEP.

2.4.5 Heat Transfer Coefficient Correlation

The heat losses account towards approximately 10-15 % of the energy which is transferred to the cylinder as a result of ignition of fuel during the combustion [40]. Force and net work which is applied over the piston decrease due to heat loss from the piston, piston ring crevices, combustion chamber surfaces and cylinder walls. So, thermal efficiency and engine performance are influenced by heat transfer. Heat flux drops to the negative and heat is transferred from cylinder walls to the charge mixture as the temperature of the cylinder charge mixture is lower than the temperature of cylinder walls. Heat flux rises to the highest level and heat is transferred from charge mixture to the cylinder during combustion especially at maximum cylinder pressure and temperatures [31, 32, 33].

According to Newton's law of cooling, heat transfer to the cylinder walls can be calculated as follows [40]:

$$\frac{dQ_{ht}}{d\theta} = \frac{1}{6n}\, h_g\, A\, (T_g - T_w) \tag{2.23}$$

$$A = \frac{V}{A_p}\, \pi\, D + 2\, A_p \tag{2.24}$$

$$A_p = \frac{\pi\, D^2}{4} \tag{2.25}$$

Where, $\frac{dQ_{ht}}{d\theta}$ is instant heat transfer versus crank angle (J/deg), n is engine speed (RPM), h_g is the instantaneous convection heat transfer coefficient, W/(m^2 K), T_g is instantaneous in-cylinder mean gas temperature versus crank angle degree (K), T_w is cylinder wall temperature (K), A is heat transfer surface area versus crank angle (m^2), V is instantaneous cylinder volume versus crank angle (m^3), D is cylinder bore (m) and A_p is piston crown area (m^2)

h_g (Convection heat transfer coefficient) is dependent on cylinder bore, cylinder volume, in-cylinder pressure, in-cylinder gas temperature and mean in-cylinder gas velocity. A correlation was obtained by Woschni for the calculation of the convection heat transfer coefficient as defined in Equation 2.26 and it was used commonly in the internal combustion engines [40, 42, 43].

$$h_g = 3.26\, D^{-0.2}\, {T_g}^{-0.55}\, P^{0.8}\, w^{0.8} \tag{2.26}$$

Where, D is the cylinder bore (m), P is the in cylinder pressure (kPa) and w is the mean gas velocity (m/s).

However, in case of low temperature combustion modes, the heat release in cylinder

occurs faster than conventional engines like SI and CI and the combustion duration is shorter. Therefore, in LTC engines, heat transfer ratio is less than that in conventional engines. For this reason, Chang at al [44] suggested a modified Woschini model for HCCI engines and a new correlation for LTC engines was developed. Therefore, Equation (2.27) and (2.28) are used for the calculation of heat transfer coefficient.

$$h_g = \alpha_{scaling}\, L^{-0.2}\, {T_g}^{-0.73}\, P^{0.8}\, \nu_{tuned}^{0.8} \tag{2.27}$$

$$\nu_{tuned} = c_1\, S_p + \frac{\frac{c_2}{6}\, V_d\, T_r}{P_r\, V_r}\, (P - P_{motored}) \tag{2.28}$$

In the equation used, T_g is calculated based on the ideal gas law over the closed cycle (compression and expansion).

2.4.6 Combustion Efficiency

Combustion efficiency is calculated by the proportion of the total released energy to the total energy delivered to the cylinder between the start and end of combustion [42]. The start of combustion of charge mixture can be determined via the second derivative of cylinder pressure value which rises from negative to positive values.

Similarly, the end of combustion can be determined via second derivative of cylinder pressure value closest to the zero. Fuel delivered to the cylinder in a cycle must be determined in order to find combustion efficiency. The combustion efficiency is calculated based on the equation given below [42].

$$\eta_{combustion} = \int_{t_{start}}^{t_{end}} \frac{\frac{dQ_{in}}{d\theta} d\theta}{m_f \, Q_{LHV_{fuel}}} \tag{2.29}$$

where m_f is the mass of fuel, $Q_{LHV_{fuel}}$ is the heating value of the fuel and dQ_{in} is the cumulative heat release rate.

2.5 Filter Design for Pressure trace

There are four steps involved in the analysis of In-cylinder pressure: level correction, angle referencing, cycle averaging and filtering. This chapter stresses on the last two steps. There are different types of filters that can be used for reducing the effect of noise and interference on the signal. Two common types of filters are Infinite impulse response (IIR) and Finite Impulse Response (FIR) filters. The latter is based on linear phase characteristics of a system, whereas the former is used for systems which are nonlinear.

In this study, different filters were studied and the most efficient one in terms of noise elimination was used for the In-cylinder pressure analysis. Initially, a center weighted moving average filter was proposed for post processing of the pressure data. However, it was observed that a moving average filter may not eliminate duct resonances properly. Moreover, sharp pressure fluctuations were also distorted. It was also observed that the sampling interval played an important role in determining the smoothing capability of the filter. Payri et. al. [45] suggested that this smoothing method was not frequency sensitive since the sharp heat release peaks were smoothed and hence not recommended. There are a wide range of IIR filters such as Butterworth filter, Chebyshev filter, Bessel filter etc. Among all these filters, Butterworth has the flattest passband and poor roll off rate. Chebyshev filter has a steeper roll off and more pass band ripple than a Butterworth filter. Since the filtering was done offline, the order of the filter had to be chosen in such a way that the roll-off is not very steep as a faster roll-off in the frequency domain corresponds to a slower response rate in the time domain.

In order to determine the filter cut-off frequency, spectral analysis of the pressure trace was performed. With the use of a MATLAB script, a Fast Fourier Transform (FFT) was performed on the pressure trace and the power spectral density of the cylinder pressure signal was obtained. Based on the power spectral density of the trace, the filter cut off frequency was determined. A low pass Butterworth filter was used to filter the pressure trace. The filter cutoff frequency was varied based on the

operating conditions and the cut-off frequency for each set of data.

2.6 Uncertainty in Analysis

Uncertainty analysis refers to the process of estimating the impact that uncertainties in measurement have on the estimated parameters. This provides the experimentalist a rational way of evaluating the significance of the derived and independent parameters on each other. In order to understand the uncertainties involved in measurement, an uncertainty analysis is performed on the experimental data. As already discussed in this chapter, most of the thermodynamic parameters are evaluated from the in-cylinder pressure trace. Some of these properties are MPRR, heat release rate, combustion phasing, Burn Duration, IMEP and thermodynamic efficiencies. To evaluate these parameters, the geometry of the engine and the thermodynamic properties at different states of the cycle are taken as the inputs. The calculated parameter Y can be expressed as a function of one or more independent variables.

$$Y = f(X_1, X_2, ...X_i) \tag{2.30}$$

Using the Uncertainty analysis, the uncertainties involved in each of the measured variables that propagate into the value of the calculated quantity can be estimated.

Assuming the individual measurements to be uncorrelated and random, the uncertainty in the calculated quantity can be determined using the Root sum of Squares (RSS) method. This method for determining the uncertainty propagation is described in NIST Technical Note 1297 (Taylor B.N and Kuyatt).

$$U_Y = \sqrt{\sum (\frac{\partial Y}{\partial X_i})^2 \, U_x^2} \tag{2.31}$$

A list of independent parameters used for calculation and post processing is given in Table 2.3.

Table 2.3
Uncertainties involved in Measurement of independent parameters during experimentation

Parameter	**Value**	**Uncertainty (±)**
Pin-cylinder	2500- 6000 (kPa)	1 (%)
Crank angle	0-720 (deg)	1 (deg)
T_{intake}	40-60-80-100 (°C)	2%
Lambda	1-5.4	0.05
Mass flow rate of intake air	8.1-66.7 (g/s)	0.72%
Mass flow rate of supply fuel	7.4-48 (mg/cycle)	0.1%
Manifold absolute pressure	95- 140 kPa	0.5%
Coolant temperature	60- 80 (°C)	2%
Engine mounted oil temperature	70- 90 (°C)	2%
$T_{exhaust}$	215- 450 (°C)	2%

As explained in Table 2.4, the range of uncertainties can be obtained for the range

Table 2.4
Range of Uncertainties involved in estimation of parameters

Parameter	**Range of Values**	**Range of Uncertainty (±)**
Burn Duration (CAD)	3-31	1
CA50(CAD aTDC)	-8-15	1
ISFC (g/kWh)	110- 325	1.2- 6.4
BSFC (g/kWh)	130- 380	2.4- 14.5
IMEP (kPa)	280- 1300	0.5- 15.5
$\eta_{ind,th}$ (%)	25.5- 47.9	0.21- 2.32
η_{comb} (%)	75.3- 95.8	0.6- 2.2

of parameters listed in the table, using the procedure discussed earlier in the section. All error bars for this thesis are calculated using the same procedure and lie in the range of values listed in the table.

Table 2.5 summarizes the uncertainties involved in calculation of the combustion and performance parameters with respect to the independent parameters.

Table 2.5
Uncertainties of calculated variables with respect to independent parameters

		% of Uncertainty of the calculated variable			
Parameter	Variable Uncertainty (±)	$P_{in-cylinder}$ (kPa)	Engine Speed (rpm)	$m_{f_{fuel}}$	Crank Angle (deg)
Burn Duration (CAD)	35 ± 1	0 %	0 %	0 %	100%
CA50(CAD aTDC)	6 ± 1	0 %	0 %	0 %	100%
ISFC (g/kWh)	285 ± 4.5	0 %	12.82 %	87.38 %	0 %
BSFC (g/kWh)	298 ± 3	0%	16.27 %	82.6 %	0 %
IMEP (kPa)	750 ± 7.7	100 %	0 %	0 %	0 %
$\eta_{ind,th}$ (%)	42.61 ± 0.46	100 %	0 %	0 %	0 %
$\eta_{combustion}$ (%)	93.6 ± 1.8	0 %	0 %	100 %	0 %

To build confidence in collected data, a repeatability of test was conducted. The tests were performed at three different time stamps in order to calculate the error in calculated variables while keeping all controlled parameters constant. The operating conditions for the tests are described in Table 2.6. The mean and standard deviation for the test points are given in Table 2.7.

Table 2.6
Test parameters

Parameter	**Value/Description**
Combustion Mode (-)	RCCI
Engine Speed (RPM)	1000
Boost Pressure (kPa)	120
Intake Air Temperature (°C)	40
Fuel Mass (mg/cycle)	15
SOI (deg bTDC)	33
IVO (deg bTDC)	25.5
EVC (deg bTDC)	22
Fuel Premixed Ratio (PR) (-)	20

Table 2.7
Mean and Standard deviation for repeatability (three trials)

Parameter	**Mean**	**Std Dev**
Intake Air Temperature (°C)	40.6	0.5
Boost Pressure (kPa)	121.5	1.3
CA50(CAD aTDC)	7	1
ISFC (g/kWh)	224.7	3.2
IMEP (kPa)	527.3	2.5
λ (-)	2.34	0.2

2.7 BMEP Parametrization

Even though the brake torque from the engine dynamometer was calculated using ACAP combustion analyzer, there was significant noise in the signal captured, as a result of which the mechanical efficiency of a large number of tests were lesser than expected. However, the exhaust temperature measurement corroborated the speculation, since it was seen that all engine cylinders were firing at the time of data acquisition. As a result of this, the measured values of the brake parameters were not credible. Thus, there arises the need for developing friction models to estimate the brake parameters.

Simple models can be used to estimate the FMEP, making use of a few independent variables, typically one related to the engine load and the other related to the engine speed, in order to separately account for the energy dissipated by friction due to the mass of fuel burned and the losses due to the speed. The Chen and Flynn model is one of the widely used friction model for the estimation of FMEP [46]. It is based on the following equation:

$$FMEP = A + B\,P_{max} + C\,n + D\,n^2 \tag{2.32}$$

As shown, this equation accounts for the engine speed (n) effect through constants C and D, while the load effect is represented by the maximum in cylinder pressure (P_{max}) through constant B. In order to be more precise in the estimation of FMEP, a higher order polynomial was developed and the load factor was accounted for, introducing the second and third power of P_{max} [46].

$$FMEP = A + B\,P_{max} + C\,P_{max}^2 + D\,P_{max}^3 + E\,n + F\,n^2 \tag{2.33}$$

The friction model was parameterized separately for each combustion mode and the corresponding coefficients were used for the estimation of FMEP and BMEP for the respective combustion regime in this thesis.

2.8 Accounting for Supercharger losses

Superchargers are usually mounted on the engine and draw power from the engine crankshaft. Thereby, a part of the power output from the engine is utilized for driving the supercharger. However, for the current setup, the supercharger is driven by an external E-motor which consumes electrical energy. The energy used in driving the supercharger needs to be accounted for. Therefore, based on an assumption that the supercharger is mounted on the engine, with a supercharger efficiency of 0.62 [47],

the power consumed by the supercharger is calculated. The Eaton M62 supercharger used for this setup is capable of running at speeds upto 14,000 rpm. However, for the experiments performed, the full capacity of the supercharger was not utilized. The experiments were run at a boost pressure limit of 1.6 bar and speeds less than 3200 rpm. This corresponds to an inlet volume flow of less than 250 m^3/hr. Given the limited operating region, a well defined supercharger efficiency could not be estimated based on Figure 2.14. Therefore, based on the operating region of the map, an average value of 0.62 was assumed to be constant for all supercharger speeds.

$$P_{consumed} = m_{f_{air}} P_{boost} \eta_{supercharger} \tag{2.34}$$

The power consumed by the supercharger for a boost pressure of 1.2 bar and 1.4 bar were calculated for a speed range of 800 to 3200 rpm as depicted in Figure 2.13

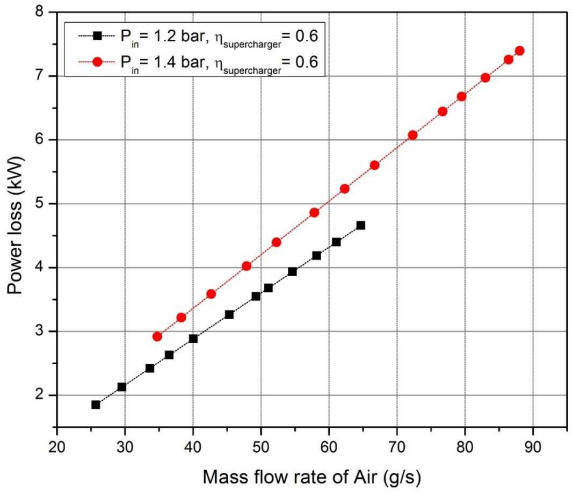

Figure 2.13: Supercharger power consumed if assumed to be mounted on the engine

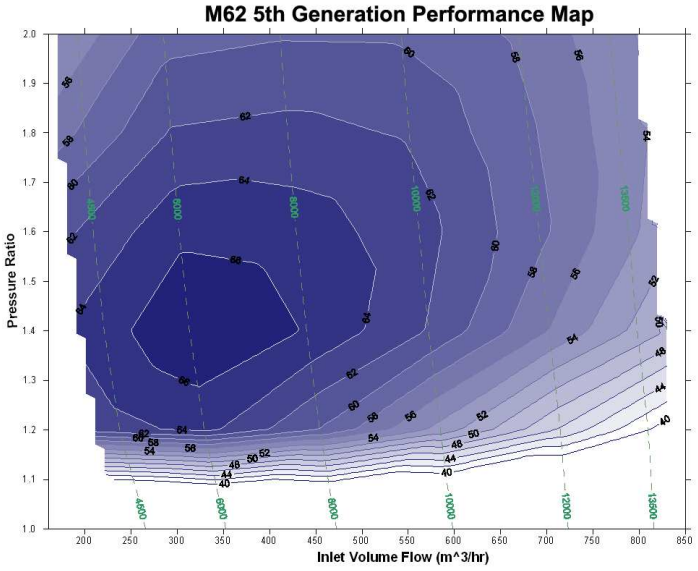

Figure 2.14: Supercharger performance map for Eaton M62 supercharger [3]

2.9 SI Map for Baseline Comparison

There is a need to quantify the improvement in fuel consumption and thermal efficiency of the LTC modes on a relative basis. In order to carry out this task, a spark ignition (SI) map was developed for the engine as a baseline comparison, as shown in Figure 2.15. It can be observed that the engine speed is in the range of 1000-4000 rpm and the engine load is in the range of 370-860 kPa IMEP. The best ISFC of 180 g/kWh was obtained at an engine speed of 3000 rpm and engine load of 390 kPa IMEP.

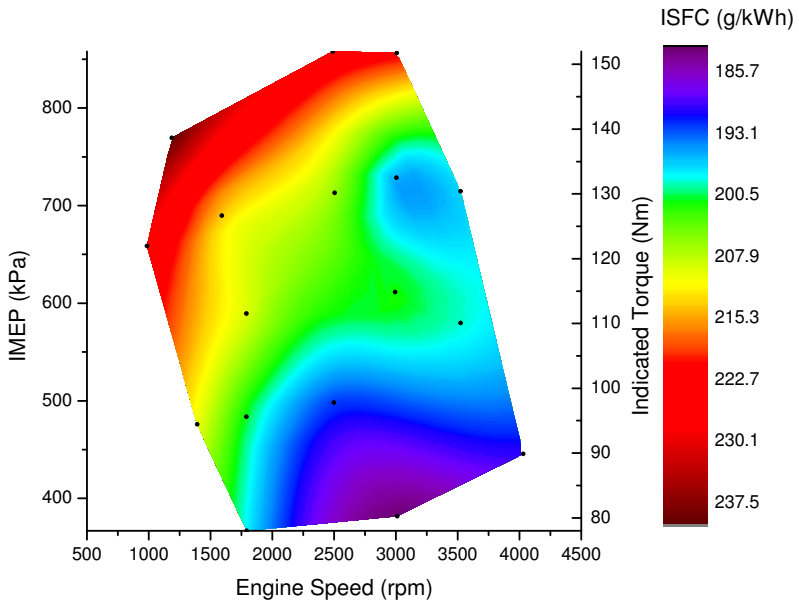

Figure 2.15: ISFC map for Spark Ignition (SI) mode

Chapter 3

Homogeneous Charge Compression Ignition (HCCI)

In this chapter a discussion for the effect of operating parameters on HCCI combustion is presented and maps were developed to determine the operating region for the HCCI combustion regime. The engine was tested in HCCI combustion mode in order to determine the operating region of the engine. Operating parameters such as intake air temperature, boost pressure, engine speed, Research Octane number (RON) of fuel and equivalence ratio were varied. The data was acquired using dSpace, ACAP combustion analyzer and LabVIEW. The acquired data was post processed using a Matlab script developed for this purpose. All indicated parameters were calculated from the mean pressure trace over 100 engine cycles and crank angle (in deg). In

order to estimate the brake parameters, the Flynn-Chen Friction Model was used to parametrize the FMEP and thereby the brake parameters were calculated. Using the post processed variables, maps for BSFC, exhaust gas temperature, IMEP and BMEP were created. The range of operating parameters are given in Table 3.1.

Table 3.1
Operating Parameters for HCCI Combustion Mode

Parameter	**Operating Conditions**
Intake Air Temperature	40-60-80-100 (°C)
Manifold Pressure	95-120-140 (kPa)
Engine Speed	800:200:2400 (rpm)
RON of Fuel	0-20-40 (-)
Lambda	1.8- 3.8 (-)

3.1 Parametrization of BMEP using Flynn-Chen Model for HCCI combustion regime

As shown in the Figure 3.1, a plot of experimental FMEP vs parameterized FMEP for HCCI combustion regime is depicted. It can be seen that the FMEP could be estimated within an error of 14%.

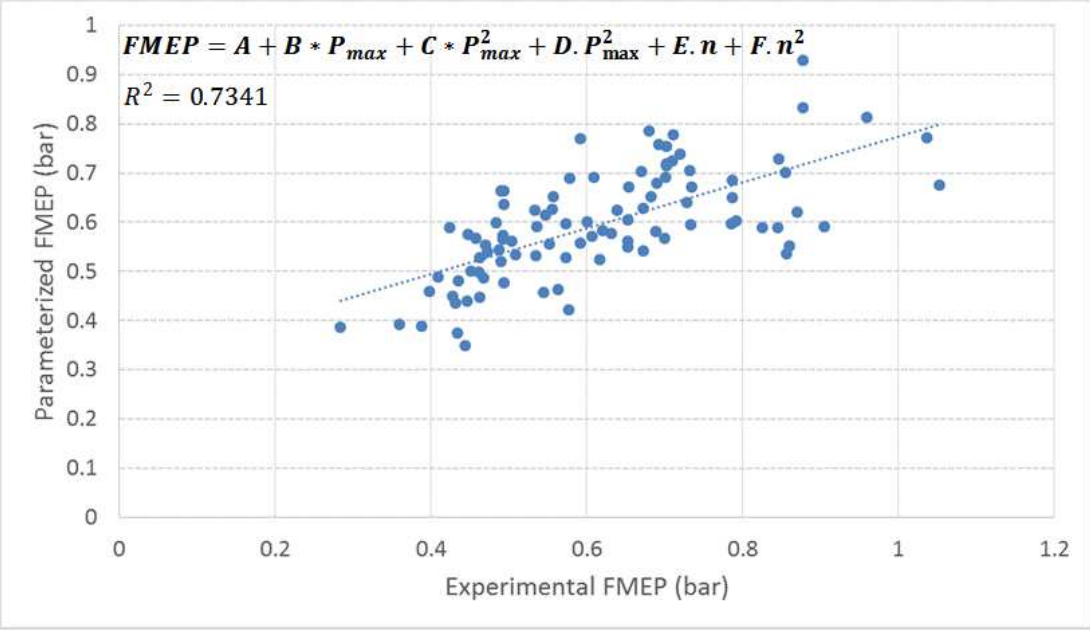

Figure 3.1: Experimental FMEP vs Parameterized FMEP

Table 3.2
Error in estimation of FMEP

Model	**Chen-Flynn with P_{max}^2 and P_{max}^3**
Mean relative error	14 %
Max relative error	37 %
Max absolute error	0.75 bar

Based on the parametrized model for FMEP, the constants obtained for the equation are given in Table 3.3.

Table 3.3
Coefficients for the Flynn- Chen Model

Coefficient	Value
A	-0.3052
B	0.0604
C	-0.0016
D	1.1159E-5
E	-0.1159
F	0.0316

3.2 Operating Range

The operating range maps for HCCI combustion regime at three different operating conditions are shown in Figures 3.2 and 3.3. Figure 3.2(a) shows the operating range for RON 0, 20 and 40 at an intake temperature of 40 °C at naturally aspirated conditions. The results are in good agreement with some HCCI studies [48, 49], in which the operating range for a given octane number reduces with higher engine speeds. It is also apparent that the operating range changes significantly with change in RON. The operating range for RON 0 occurs at a leaner equivalence ratio as compared to RONs 20 and 40. Higher RON reflects a lower reactivity, requires relatively richer mixture to initiate the combustion. The mixtures with lower lambda values have higher energy content. Therefore, the engine load can be increased. However, the control of the SOC is very difficult at higher RONs especially at lower intake air

temperatures. Studies have shown that HCCI engines operate well at part loads [4]. The pressure oscillations are larger at higher engine loads due to the high MPRR and HRR characteristics. Moreover, due to the rich fuel-air mixture at higher engine loads, the auto ignition is due to the locally rich zones in the cylinder. However, there is a higher knock intensity in these cases. Therefore, the homogeneous air-fuel mixture could be diluted with trapped residuals and reduce the gradient of the heat release rate. On the contrary, the compression and combustion temperatures and pressures are lower. In this case, dilution using residual gases can lead to unstable combustion and result in a misfire. The HCCI operating range is limited due to this characteristic of HCCI engines at high engine loads and speeds [50]. As illustrated in Figure 3.2 and Figure 3.3, it is evident that there is a marked difference in the operating range for HCCI at an increased intake temperature and boost pressure. Higher intake temperatures and boost pressures result in enabling HCCI operation over a wider equivalence ratio and a larger speed range. This is mainly attributed to the mixture composition at IVC. With an increase in intake temperature and boost pressure, the density of the air decreases. This results in an increase in the mass flow rate of air being inducted into the cylinder, thereby making the mixture much leaner.

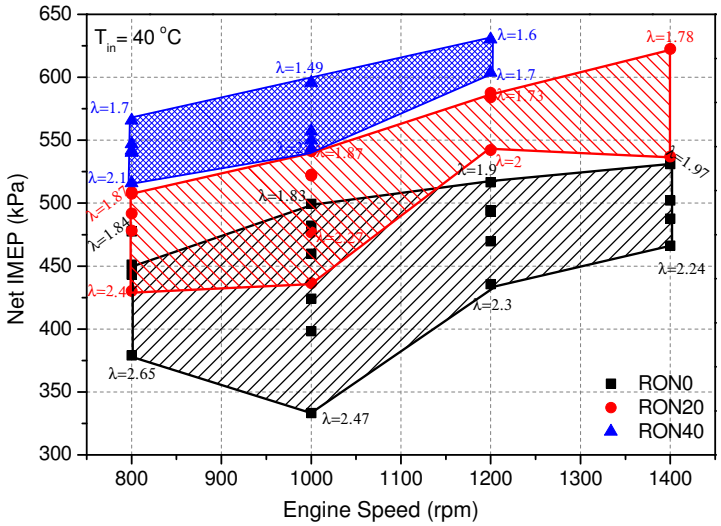

(a) 40 °C intake air temperature and naturally aspirated

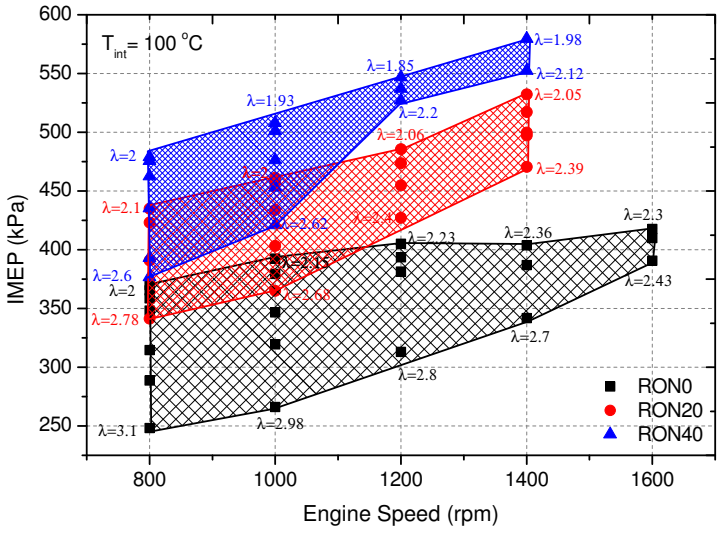

(b) 100 °C intake air temperature and naturally aspirated

Figure 3.2: HCCI IMEP and speed range

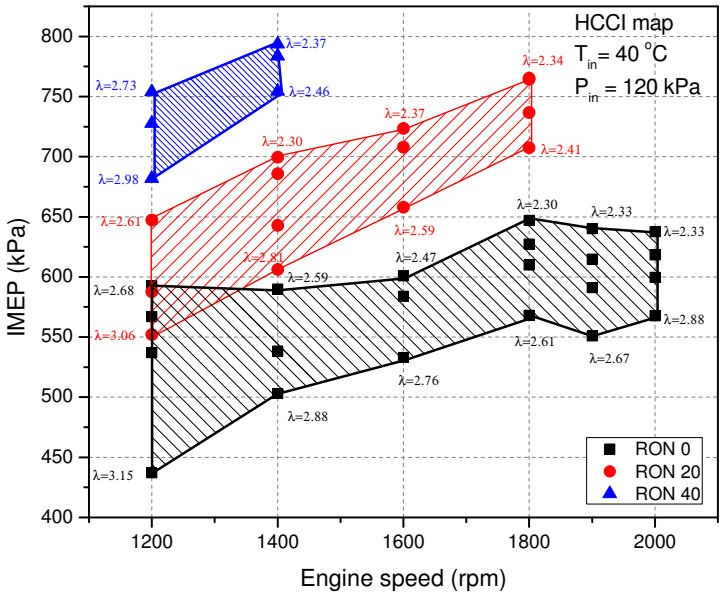

Figure 3.3: HCCI IMEP and speed range for 40 °C intake air temperature and 120 kPa intake pressure

3.3 Maps for ISFC, BSFC, Indicated Thermal Efficiency and Exhaust Gas Temperature

ISFC is an indicator as to how efficient the engine is, in utilizing the fuel supplied to do useful work, without accounting for the friction losses [51]. Figure 3.4 shows the ISFC map for HCCI combustion regime for RON 0, 20 and 40 at an intake air temperature of 40 °C and naturally aspirated conditions. It can be observed that the minimum ISFC is at the low loads for RON 40 with a value of 205 g/kWh. The trend

shows that the ISFC improves with higher RON, where the combustion pressures and the heat release rates are lower [52]. The low ISFC at these points is a result of the combustion phasing being optimized where the compression work is minimized and expansion work is maximized [53].

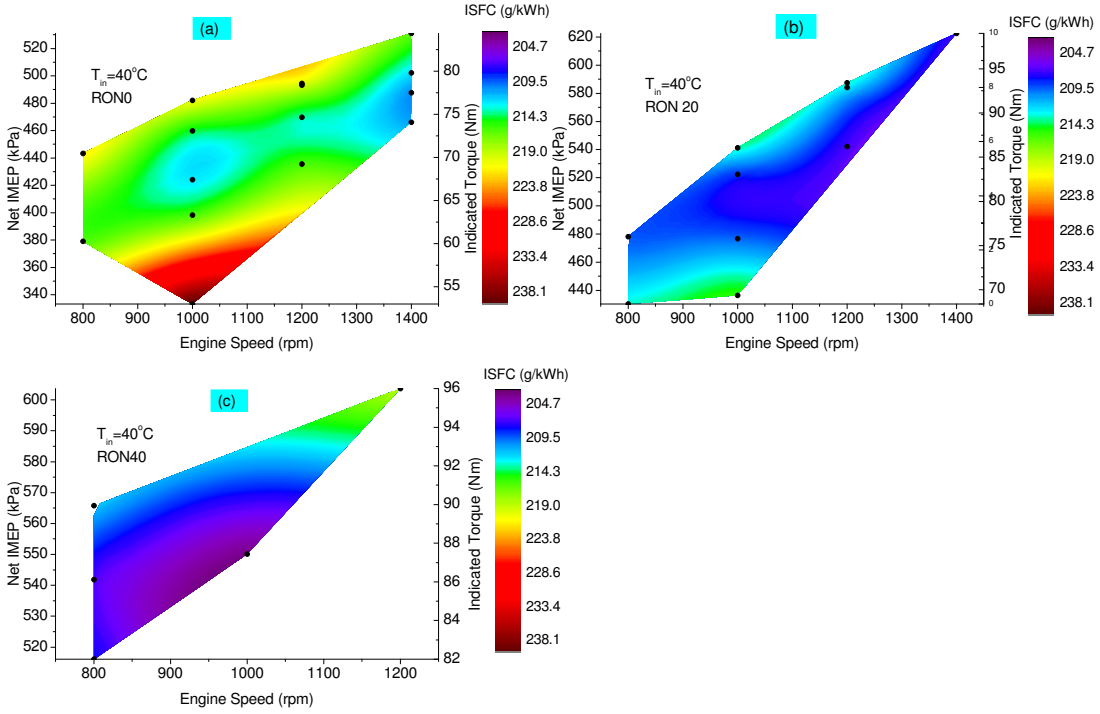

Figure 3.4: HCCI ISFC map for 40 °C intake air temperature at naturally aspirated conditions

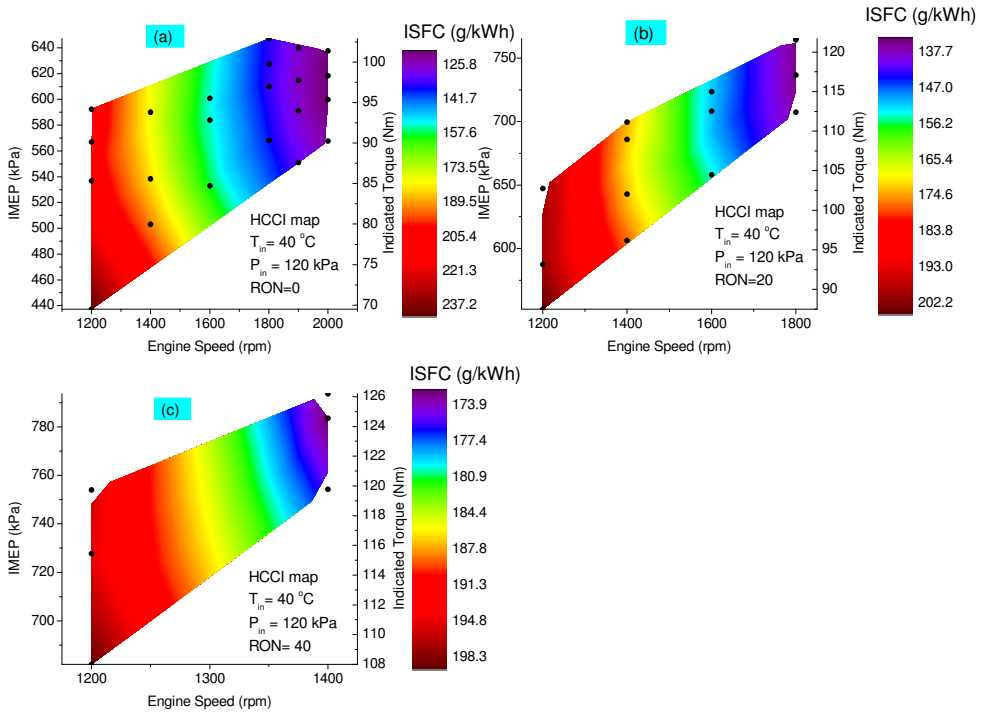

Figure 3.5: HCCI ISFC map for 40 °C intake air temperature and 120 kPa intake pressure

Brake specific fuel consumption (BSFC) maps are shown in Figure 3.6 for RON 0, RON 20 and RON 40 at an intake temperature of 40 °C. When all the intake air temperatures and RONs are taken into consideration, it is seen that the load range of the HCCI engine is between about 50-100 Nm which is ideal for an LTC engine. BSFC maps are very important to understand the most efficient operation ranges of the HCCI engine. HCCI engines can be looked upon as range extenders for hybrid

electrical vehicles in near future [54]. Total efficiency of a hybrid vehicle can be increased by operating the HCCI engine at the most efficient point. Therefore, BSFC, thermal efficiency, CA50 and similar maps have importance to determine an efficient operation range. As seen in the figures, the lowest BSFC is obtained as 210 g/kWh with RON 0. Fuels having high reactivity allow leaner HCCI operation as it is mentioned above. As a result of this lower BSFC values are obtained. Increased intake air temperature causes a decrease in volumetric efficiency of the engine at naturally aspirated operations. Therefore, BSFC increases at higher intake air temperatures. When HCCI operation is observed at boosted conditions, it can be observed that the BSFC improves with an increase in engine speed. The best BSFC is obtained at high speeds and high loads for all three RONs, as shown in Figure 3.7. The pumping losses increase with boosting and reduce significantly with an increase in engine speed [40]. Moreover, the combustion duration is longer for lower engine speeds [55], which tends to have a negative effect on BSFC. However, with an increase in engine speed, the shorter combustion duration and a lower pumping losses results in an improvement in BSFC.

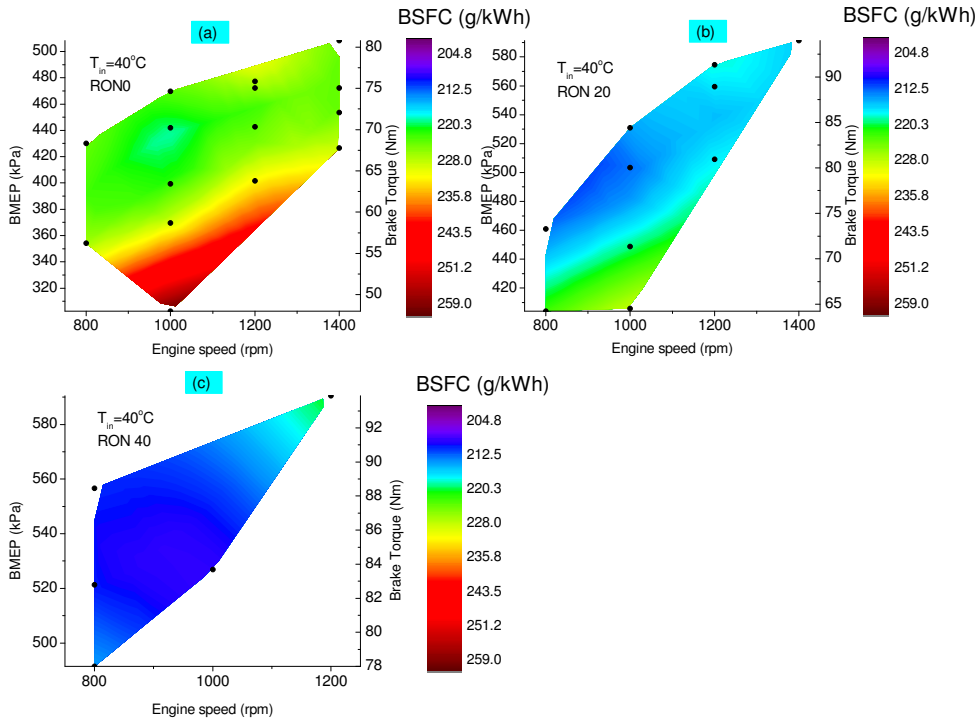

Figure 3.6: HCCI BSFC map for 40 °C intake air temperature at naturally aspirated conditions

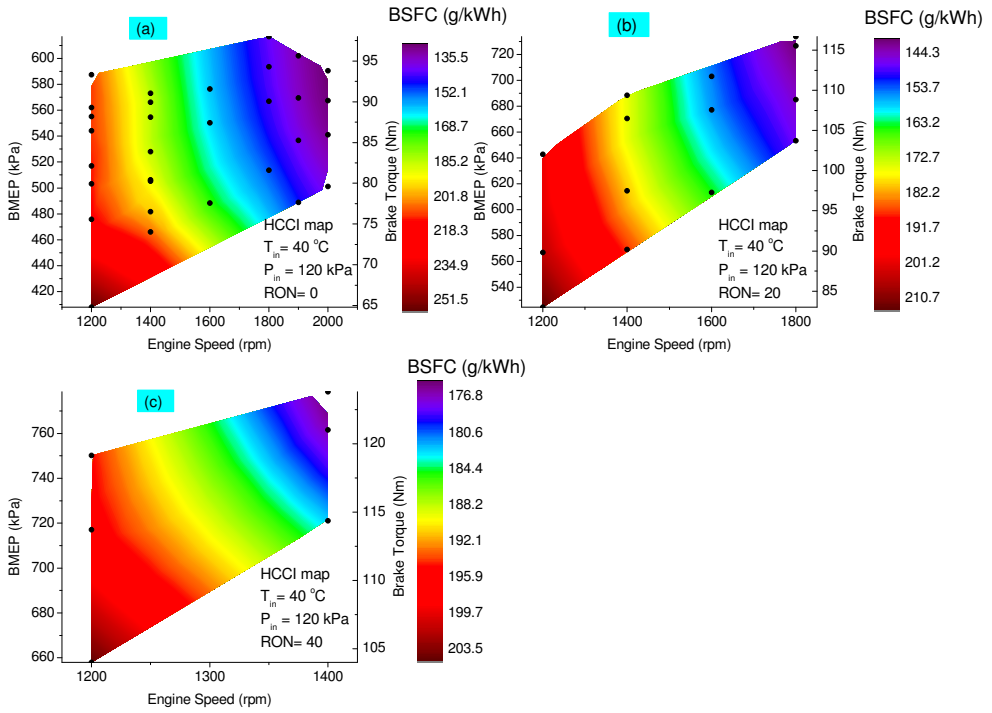

Figure 3.7: HCCI BSFC map for 40 °C intake air temperature at 120 kPa intake pressure

The indicated thermal efficiency map for HCCI at the same operating conditions is illustrated is Figure 3.8. It can be seen that the map is in accordance with the ISFC map. The best thermal efficiency is achieved at the lowest ISFC regions. The present data shows that combustion phasing has a significant effect on HCCI efficiency. All the best thermal efficiency regions were attained at a combustion phasing of 5-8 °aTDC [40]. A maximum thermal efficiency of 40% was obtained at mid load conditions for all three RONs at 40 °C. This is mainly because of reduced heat transfer losses due

to lower compression and combustion temperatures [56]. Moreover, the combustion phasing was optimal, which enabled better mixing of the air-fuel mixture at mid load conditions. The range of thermal efficiencies for the given operating conditions were 33-40 %.

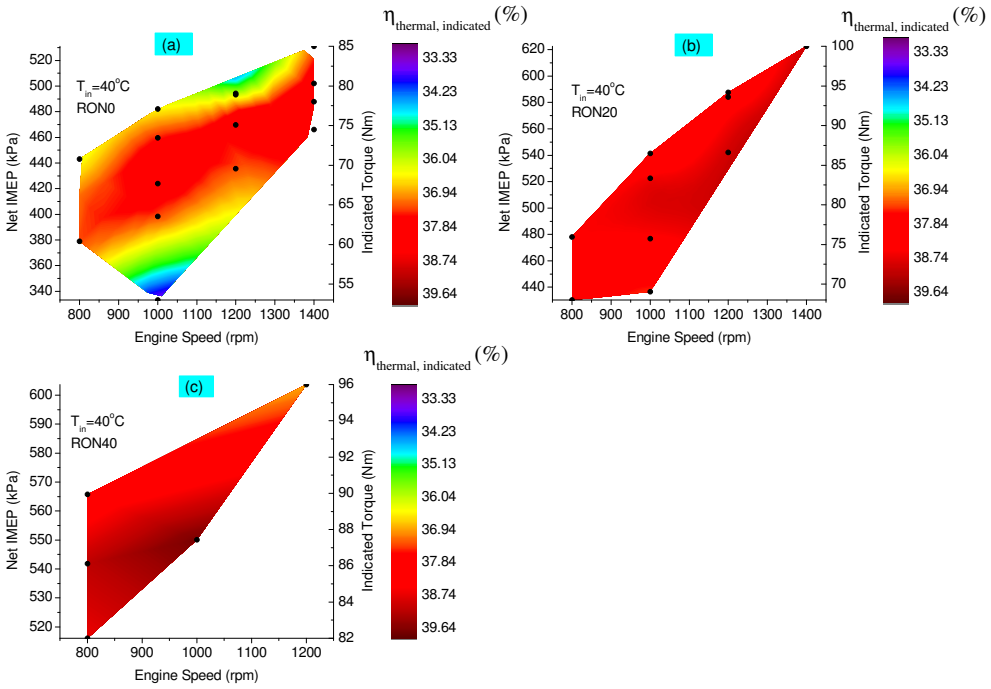

Figure 3.8: HCCI indicated thermal efficiency map for 40 °C intake air temperature at naturally aspirated conditions

HCCI holds the advantage of achieving ultra-low NOx and PM, with a relatively low SFC as compared to SI/CI combustion regimes. However, higher HC and CO

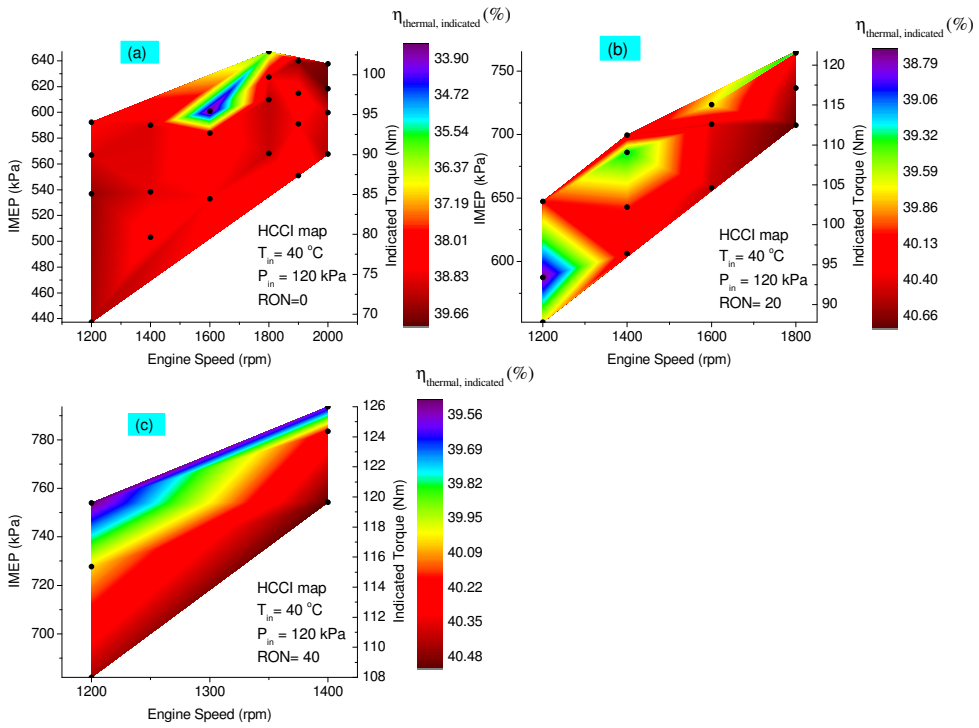

Figure 3.9: HCCI Indicated thermal efficiency map for 40 °C intake air temperature and 120 kPa intake pressure

emissions is a major challenge for HCCI engines. Moreover, the lower exhaust temperatures in HCCI is a limiting factor in constraining the operating range of the engine [57] because high exhaust gas temperature is required to achieve high efficiency of the oxidation catalysts. The catalysts can reach conversion efficiencies of around 95 % for HC and CO, as long as the catalyst light off temperatures are in the range of 250- 300 °C [40, 58, 59]. As seen in Figure 3.11 for naturally aspirated conditions at T_{intake} of 40 °C, the exhaust gas temperature range is between 223âĂŞ400 °C over the entire speed and load range. This is an acceptable range for the catalytic converter

to function properly. Moreover, with this range of temperatures, if the turbocharger is used to extend operating range for high loads, there would be sufficient energy to drive the turbo [58]. The exhaust temperature range for boosted conditions is shown in Figure 3.10 for the entire range of speeds and loads. It can be seen that the exhaust temperature increased with an increase in load and speed for both naturally aspirated and boosted conditions. The range of temperatures is 230 °C to 410 °C, which is equivalent to the temperatures attained in SI combustion for low and mid loads. The energy, if extracted from the exhaust gas using a waste heat recovery system, could be used to heat the intake air, thereby eliminating the need of electrical energy to drive the intake air heater.

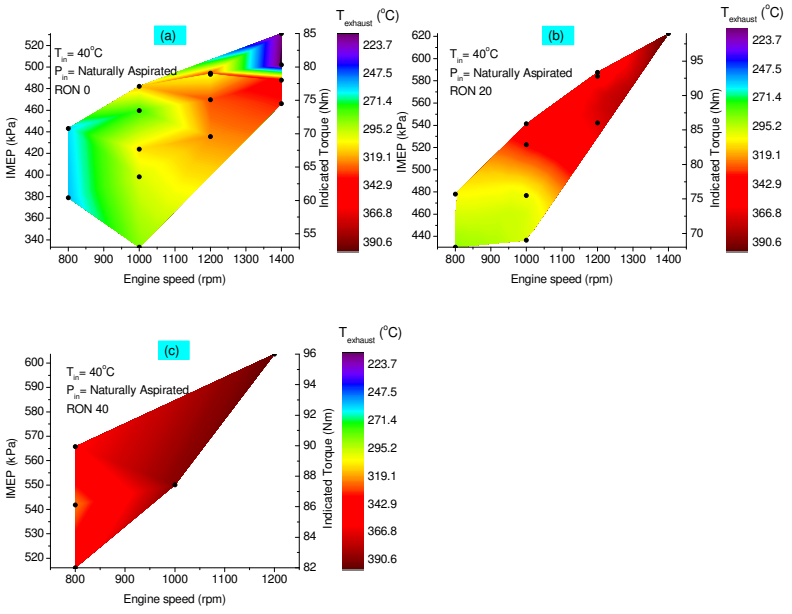

Figure 3.10: HCCI exhaust gas temperature map for 40 °C intake air temperature and Naturally aspirated

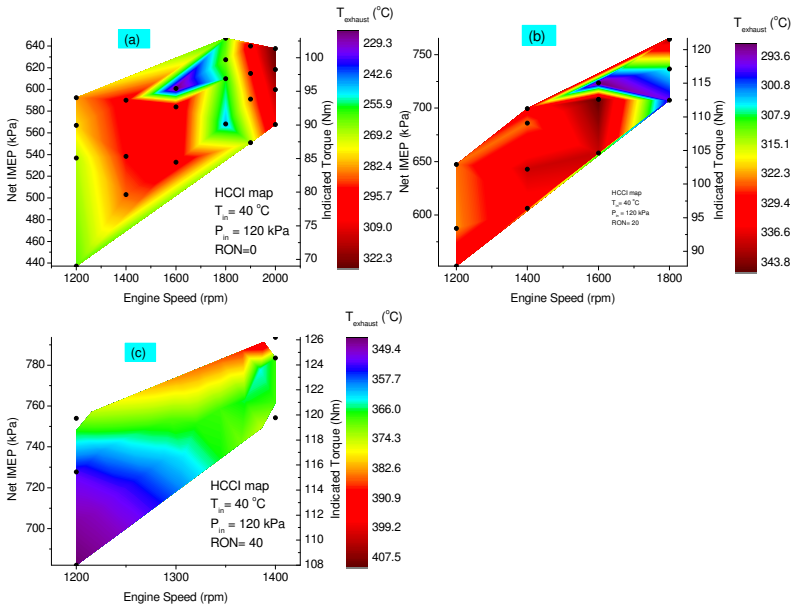

Figure 3.11: HCCI exhaust gas temperature map for 40 °C intake air temperature and 120 kPa Boost Pressure

3.4 Optimized HCCI maps

HCCI tests were carried out for 900 data points over a wide range of operating conditions (Intake air temperature, Boost pressure, RON, Engine speed and equivalence ratio). An optimized map for best ISFC at each speed-load condition was developed and other maps for BSFC, thermal efficiency and exhaust temperature were derived from the optimized data set. The optimized maps were created separately for naturally aspirated and boosted conditions. The data points considered for developing

these maps are given in Appendix A.2. ISFC maps for intake pressures of 100 kPa and 120 kPa are illustrated in Figures 3.12 and 3.13, respectively. While it can be seen that equivalence ratio has a significant effect on the ISFC for naturally aspirated conditions, engine speed takes over predominance for boosted conditions. ISFC increases with a drop in IMEP and indicated torque since the mixture becomes leaner. As a result of this, the oxygen dilution is higher and thereby decreasing combustion temperatures. The best ISFC achieved was 200 g/kWh and 110 g/kWh for naturally aspirated and boosted conditions, respectively. The speed range and load range improved considerably for a boost pressure of 120 kPa as compared to those for 100 kPa.

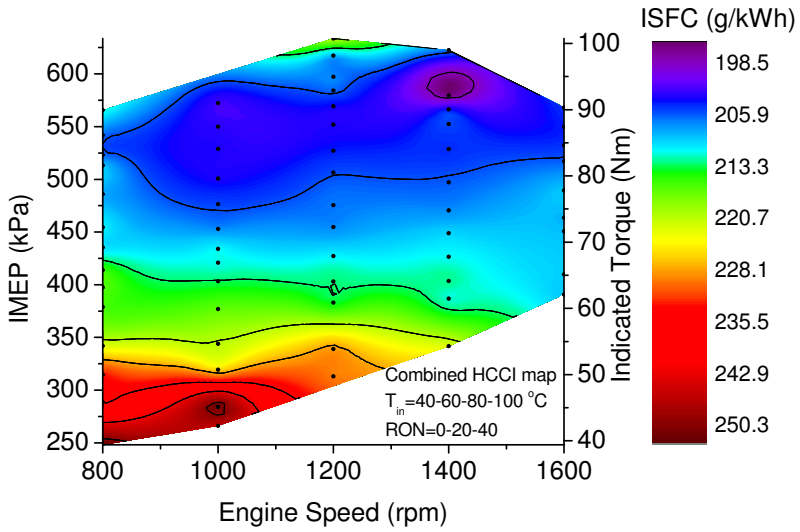

Figure 3.12: HCCI ISFC map for all intake air temperatures and RONs at naturally aspirated conditions

BSFC maps for boost pressures of 100 kPa and 120 kPa are illustrated in Figures 3.14

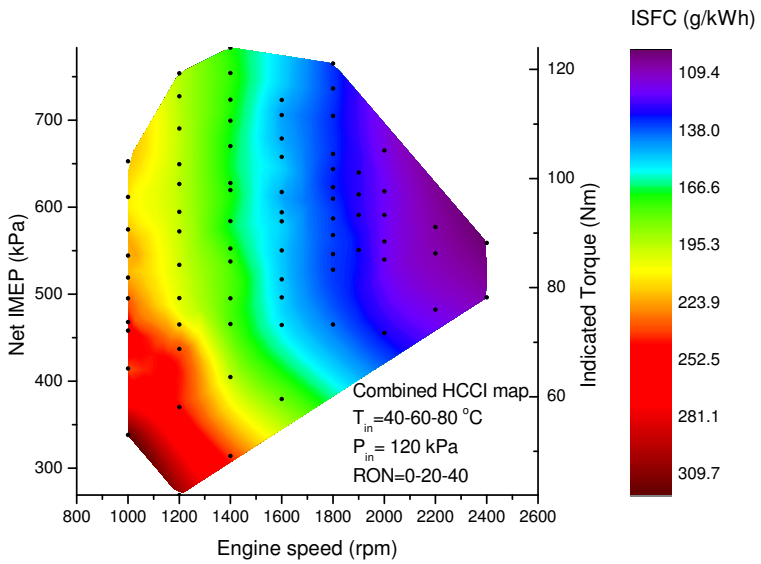

Figure 3.13: HCCI ISFC map for all intake air temperatures and RONs and 120 kPa intake pressure

and 3.15, respectively. It can be seen that the trends are very similar to that of ISFC maps. It can be seen that BMEP decreased with decrease in equivalence ratio. The sweet spot for BSFC (210 g/kWh) for 100 kPa was obtained at 1400 rpm engine speed and 88 Nm brake torque. For 120 kPa boost pressure, the best BSFC of 130 g/kWh was obtained at maximum engine speed of 2400 rpm and 80 Nm brake torque. At high engine speeds, the engine seems to run at a higher combustion efficiency typically above 92 %. This is a result of better fuel-air mixing and higher homogeneity of the mixture [60]. However, at low engine speeds and low loads, the BSFC increases due to the unburned fuel at the exhaust, which approximately corresponds to 80-90 % of combustion efficiency.

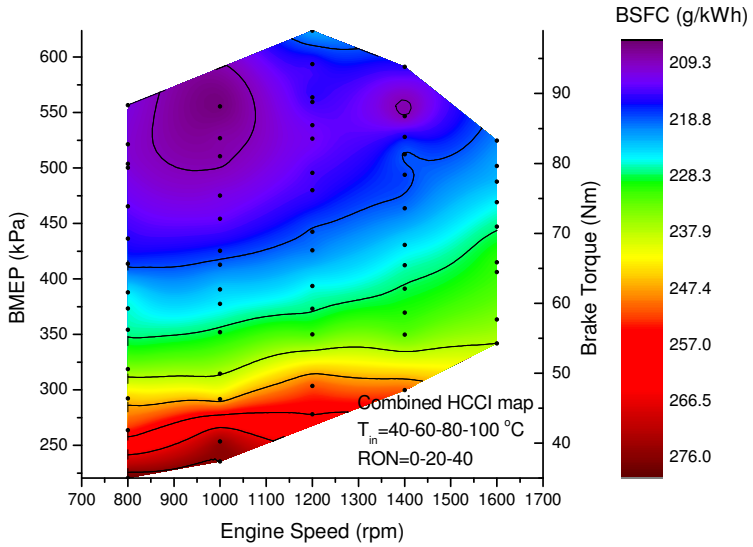

Figure 3.14: HCCI BSFC map for all intake air temperatures and RONs at naturally aspirated conditions

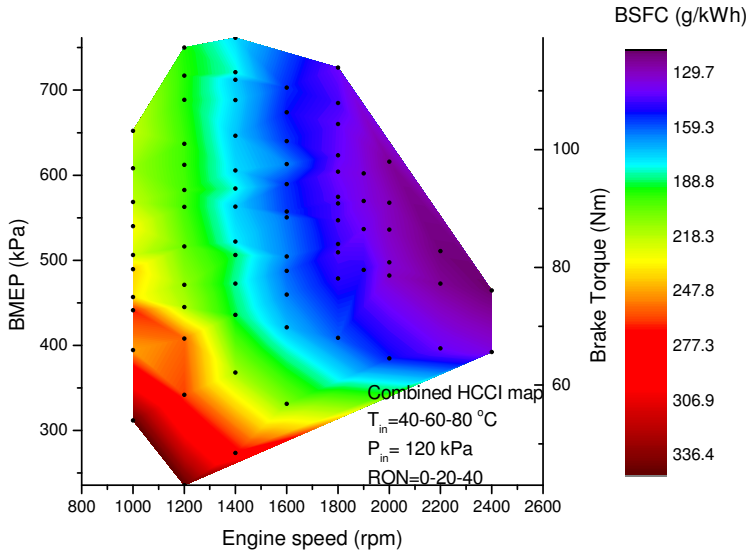

Figure 3.15: HCCI BSFC map for all intake air temperatures and RONs and 120 kPa intake pressure

The $\eta_{th,ind}$ maps for 100 kPa and 120 kPa boost pressure are illustrated in Fig 3.16 and 3.17, respectively. It can be observed that the net indicated thermal efficiency improved with an increase in boost pressure. With an increase in operating range in terms of load and speed, a boost pressure of 120 kPa yielded a peak indicated thermal efficiency of 46% while 100 kPa intake pressure had a peak thermal efficiency of 41%. Moreover, with an increase in equivalence ratio, the thermal efficiency increased for both intake pressures. With richer mixture the compression and combustion temperatures are significantly higher and therefore the combustion efficiencies are higher [56]. The data shows that for better thermal efficiencies, the combustion efficiencies should be higher than 91% to prevent this from having a deteriorating effect on thermal efficiency.

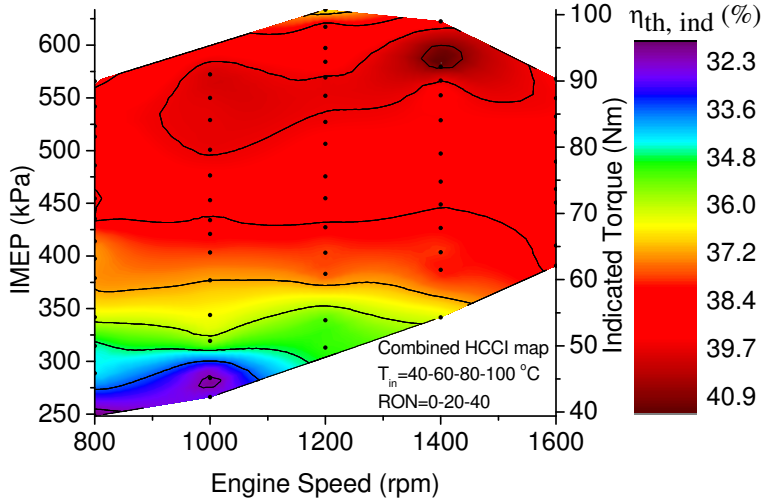

Figure 3.16: HCCI indicated thermal efficiency map for all intake air temperatures and RONs at naturally aspirated conditions

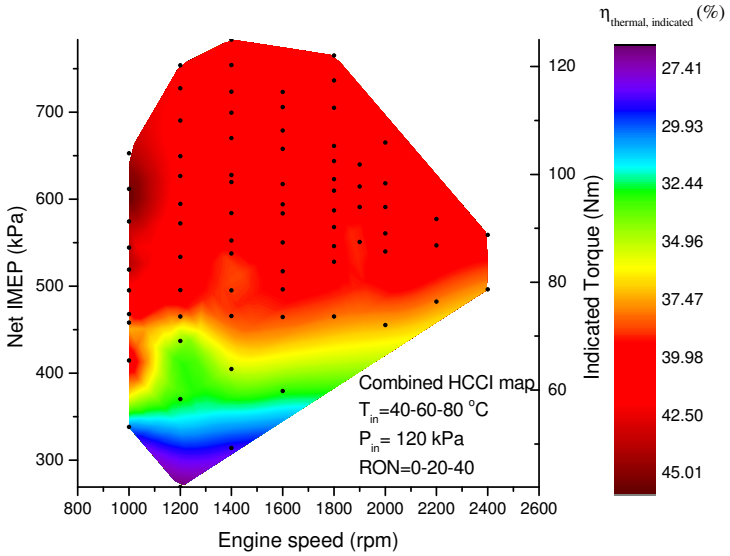

Figure 3.17: HCCI indicated thermal efficiency map for all intake air temperatures and RONs and 120 kPa intake pressure

The optimized exhaust temperature map for naturally aspirated and boosted conditions is illustrated in Figures 3.18 and 3.19. A total of 250 data points were considered to develop the optimized maps and it can be observed from the Appendix A2 that over 75% of the data points have an exhaust temperature greater than 250 °C, which implies that the HC and CO after treatment could be accomplished with a good conversion efficiency of the catalytic converter. It can be observed that the exhaust temperature increases with an increase in engine speed and load due to increase in compression and combustion temperatures. However, at low loads and low speeds, the low $T_{exhaust}$ could limit the practical operation of HCCI engines. But this can be overcome by retarding the combustion phasing for these data points after TDC, thereby compromising on the thermal efficiency of the engine [56].

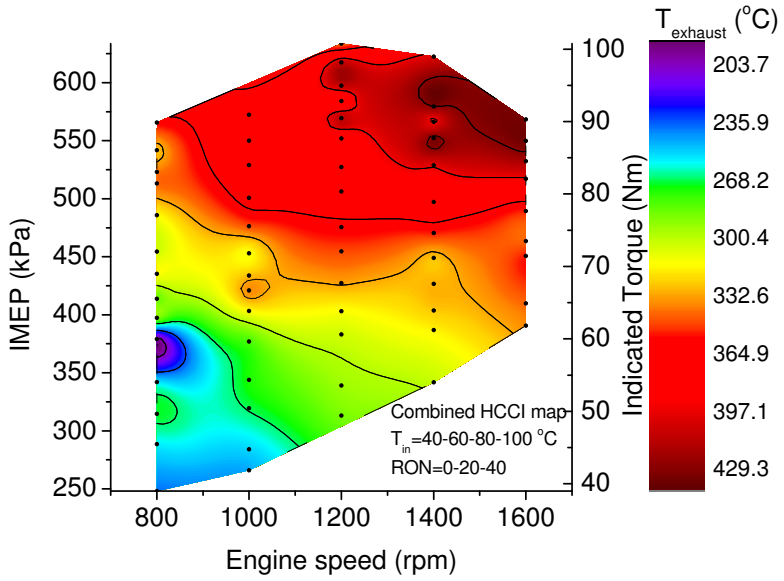

Figure 3.18: HCCI exhaust temperature map for all intake air temperatures and RONs at naturally aspirated conditions

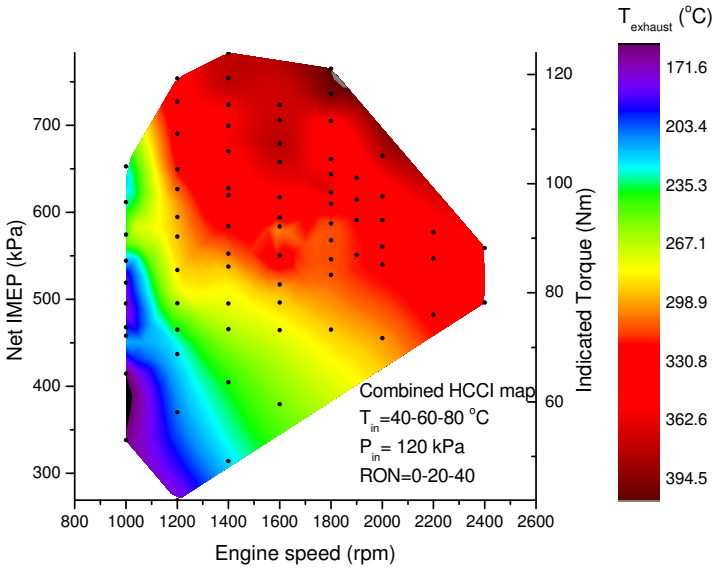

Figure 3.19: HCCI exhaust temperature map for all intake air temperatures and RONs and 120 kPa intake pressure

3.5 Effects of RON on HCCI combustion

Pressure and heat release rate traces for different RONs at 1000 rpm engine speed and intake air temperature of 100 °C are seen in Figure 3.20. Lambda value is around 2.4 for each RON. Combustion characteristics of different RONs in HCCI mode such as CA10, CA50, CA90 and CA10-90 are also seen in Figure 3.21. As it can be seen from pressure trace, heat release rate trace and CA10 values, the SOC is advanced with lower RONs. The reactivity of the fuel decreases with an increase in RON. Higher reactivity enables earlier SOC. This property of the fuel can be useful at low intake air temperatures and lower engine loads. However, at the high intake air temperatures and higher engine loads, the control of SOC and combustion phasing becomes challenging. CA50 is around -6 CAD aTDC for RON0 that results in a lower thermal efficiency. Typically, the combustion phasing must be 8-10 CAD aTDC in order to achieve the best thermal efficiency [40]. This can be attributed to the fact that the heat transfer losses are minimal at the optimal combustion phasing, thereby leading to better thermal efficiencies [60]. It can be seen in Fig 3.21 that as the CA50 approaches close to 8 CAD aTDC, the thermal efficiency increases. The combustion phasing retards as the RON increased because SOC is retarded for RON20 and RON40 compared to RON0.

Table 3.4
Operating conditions used for the experiments to study the effect of RON on HCCI combustion

Test Parameters	**Value/ Desciption**
Engine Speed	1000 (rpm)
Injection Pressure	3.5 (bar)
Injection Starting Angle	450 (deg bTDC)
Fuel Type	RON 0 -20- 40
IVO	25.5 (deg bTDC)
EVC	22 (deg bTDC)
Throttle Body Position	100 (%)
Intake Air Temperature	100 (°C)
Lambda	2.4

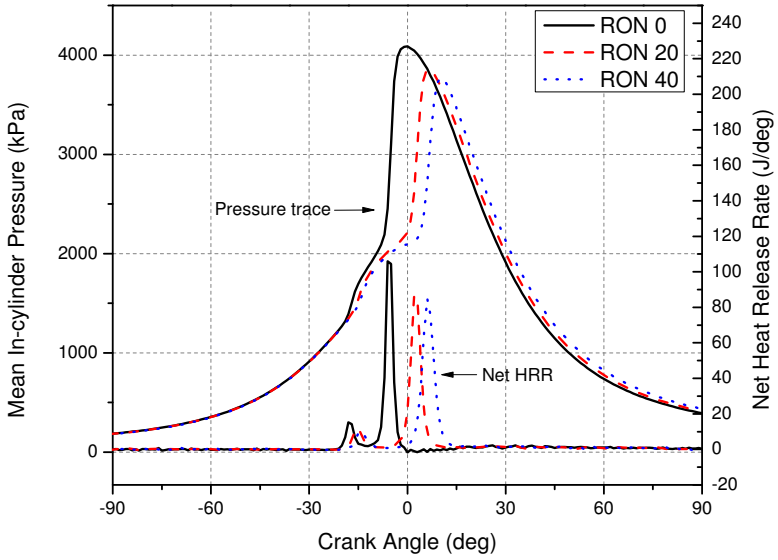

(a) Pressure and heat release rate

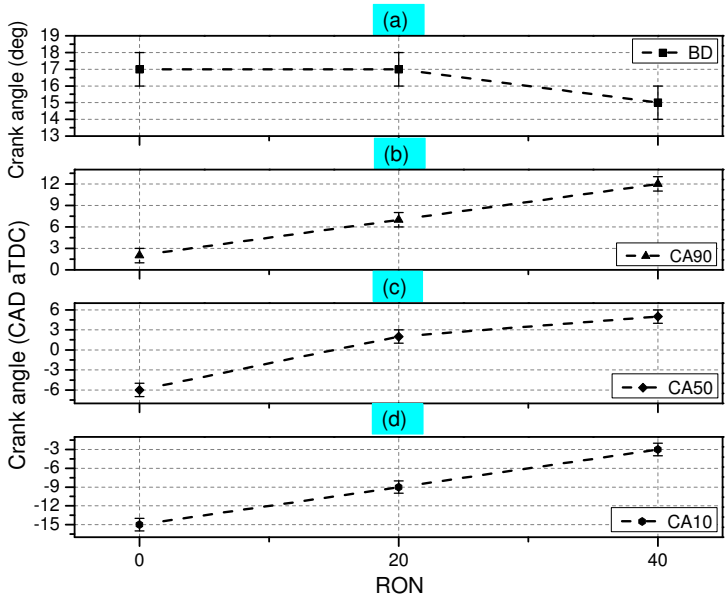

(b) Combustion phasing characteristics

Figure 3.20: a) Pressure and heat release rates for RON 0, 20 and 40 at 1000 rpm and intake temperature of 100 °C and b) Combustion phasing parameters for HCCI combustion regime

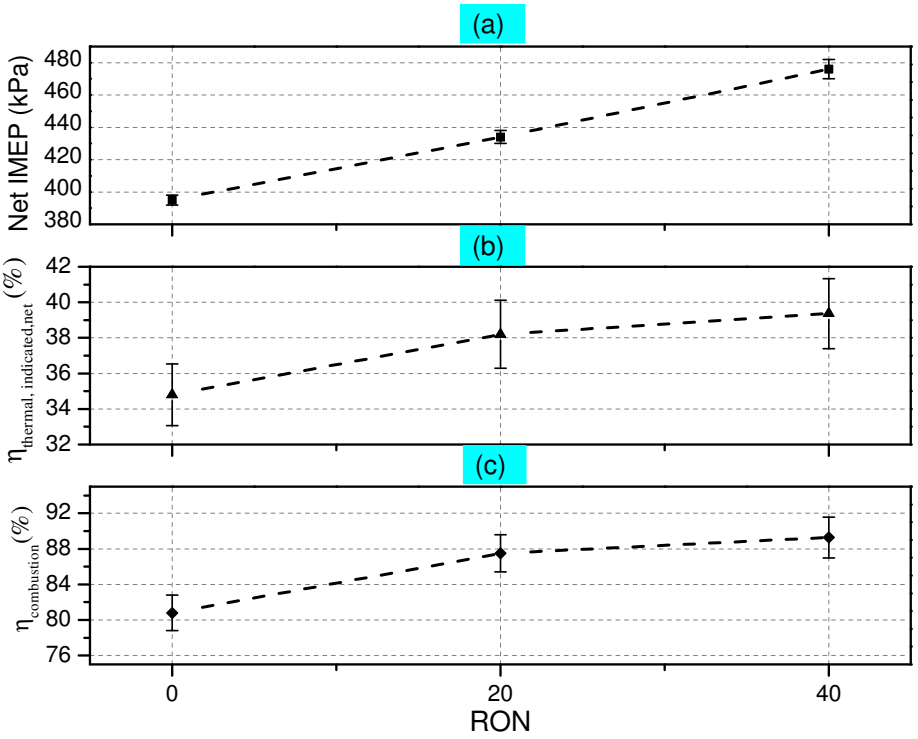

Figure 3.21: Effects of the RON on a) IMEP, b) Indicated thermal efficiency and c) Combustion efficiency for HCCI combustion regime

3.6 Effects of Intake Air temperature on HCCI combustion

Pressure and heat release rate traces for different intake air temperatures at 1000 rpm engine speed are seen in Figure 3.23(a). Lambda value is around 2.3 for each temperature. Combustion characteristics of different intake air temperatures in HCCI

mode such as CA10, CA50, CA90 and CA10-90 are also seen in Figure 3.23(b). The range of values for T_{intake} and lambda were chosen based on the acceptable operating region for HCCI combustion with MPRR less than 8 bar/CAD and COV less than 10 % [61]. HCCI combustion became unstable with leaner equivalence ratios because of misfiring at lower engine speeds and high loads. Moreover, higher MPRR at higher T_{intake} and richer equivalence ratios resulted in higher knock intensities. The increase of T_{intake} improves the auto-ignition characteristics of the mixture in the cylinder. The SOC is advanced at higher intake air temperature as seen in Figure 3.23(b) due to the increased temperature of compression. Furthermore, with an increase in T_{intake}, the chemical reactions between HC and oxygen molecules in side the cylinder was accelerated. As a result of this, the Burn Duration (BD) values decreased with an increase in T_{intake}. From Figure 3.22 and 3.23, it can be seen that the best thermal efficiency is obtained at a combustion phasing of 6 CAD aTDC. The thermal efficiency is lower at other temperatures for which the IMEP values are relatively lower due to the change in fuel energy inducted in the cylinder. As a result of this, the ratio of specific heat of the charge gases decrease due to the higher compression temperatures [56].

Table 3.5
Operating conditions used for the experiments to study the effect of intake air temperature on HCCI combustion

Test Parameters	Value/ Desciption
Engine Speed	1000 (rpm)
Injection Pressure	3.5 (bar)
Injection Starting Angle	450 (deg bTDC)
Fuel Type	RON 20
IVO	25.5 (deg bTDC)
EVC	22 (deg bTDC)
Throttle Body Position	100 (%)
Intake Air Temperature	40, 60, 80, 100 (°C)
Lambda	2.2

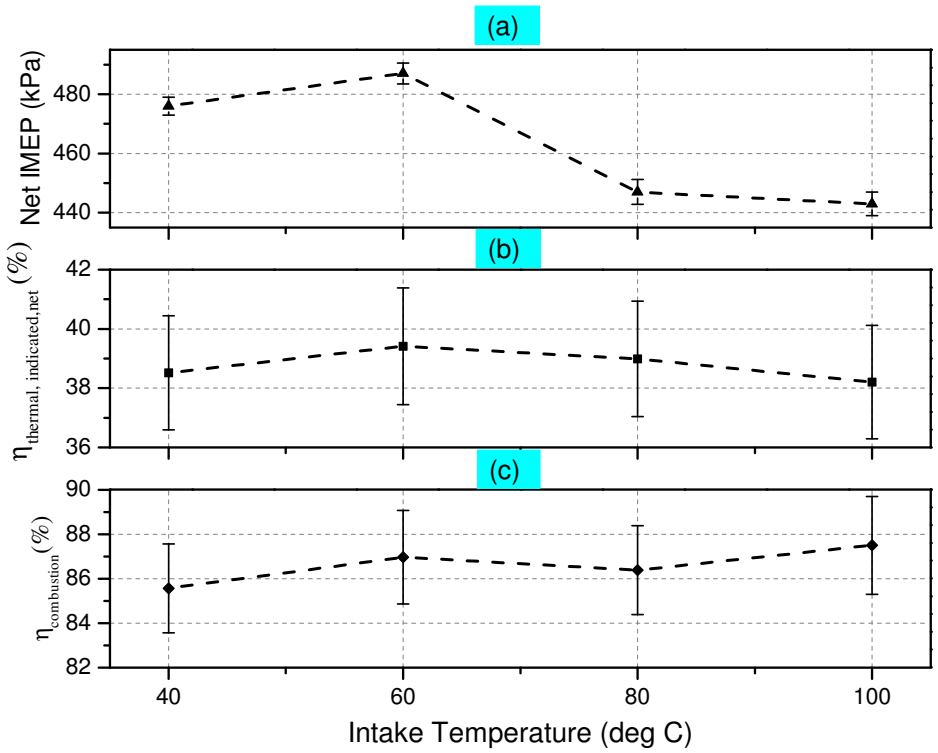

Figure 3.22: Effects of the intake air temperature on 1. IMEP, 2. Indicated thermal efficiency and 3. Combustion efficiency for HCCI combustion regime

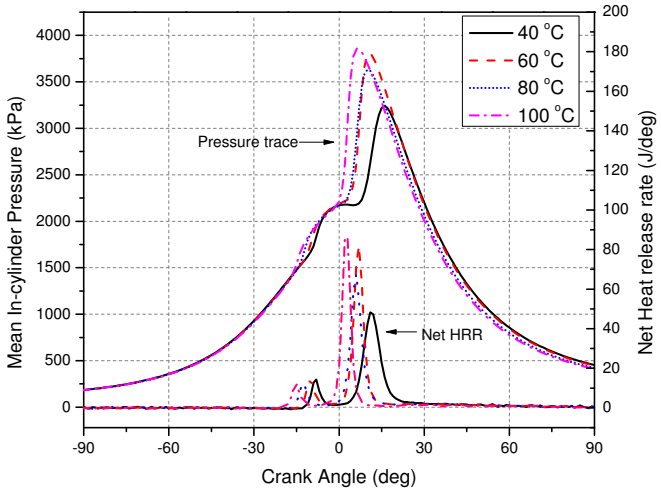

(a) Pressure and heat release rate curve

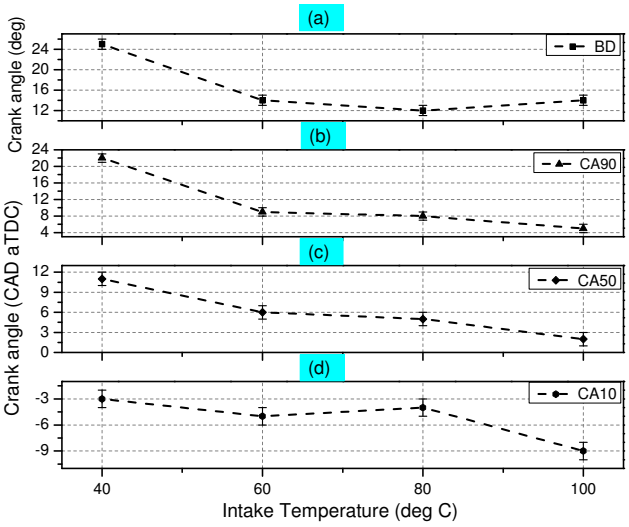

(b) Combustion characteristics

Figure 3.23: a) Pressure and heat release rates for intake air temperatures 40, 60, 80 and 100 °C at 1000 rpm and RON of 20 and b) Effects of the intake air temperature on combustion characteristics (CA10 CA50, CA90 and Burn Duration) for HCCI combustion regime

3.7 Effect of boost pressure on HCCI combustion

Pressure and heat release rate traces for different intake boost pressures at 1000 rpm engine speed and intake air temperature of 40 °C are seen in Figure 3.24. Lambda value is around 2.2 for each intake pressure. Combustion characteristics of different boost pressures in HCCI mode such as CA10, CA50, CA90 and BD are also seen in Figure 3.25. As seen through Figure 3.24, the peak pressure of combustion increases with an increase in boost pressure. This is due to the increase in the effective charge energy being induced into the cylinder owing to the increase in the air flow rate. In order to maintain the same lambda, the fuel quantity increases. As a result of this, the IMEP also increases with an increase in boost pressure. However, the thermal efficiency and the combustion efficiency decreases. The drop in efficiencies is due to the CA50 being too advanced bTDC. For the same lambda, with an increase in boost pressure, the CA50 tends to get advanced since the start of combustion is advanced with higher pressures at IVC.

Table 3.6
Operating conditions used for the experiments to study the effect of Boost pressure on HCCI combustion

Test Parameters	Value/ Unit
Engine Speed	1000 (rpm)
Injection Pressure	3.5 (bar)
Injection Starting Angle	450 (deg bTDC)
Fuel Type	RON 40
IVO	25.5 (deg bTDC)
EVC	22 (deg bTDC)
Throttle Body Position	100 (%)
Intake Air Temperature	40 (°C)
Lambda	2.2
Boost Pressure	100, 120, 140 (kPa)

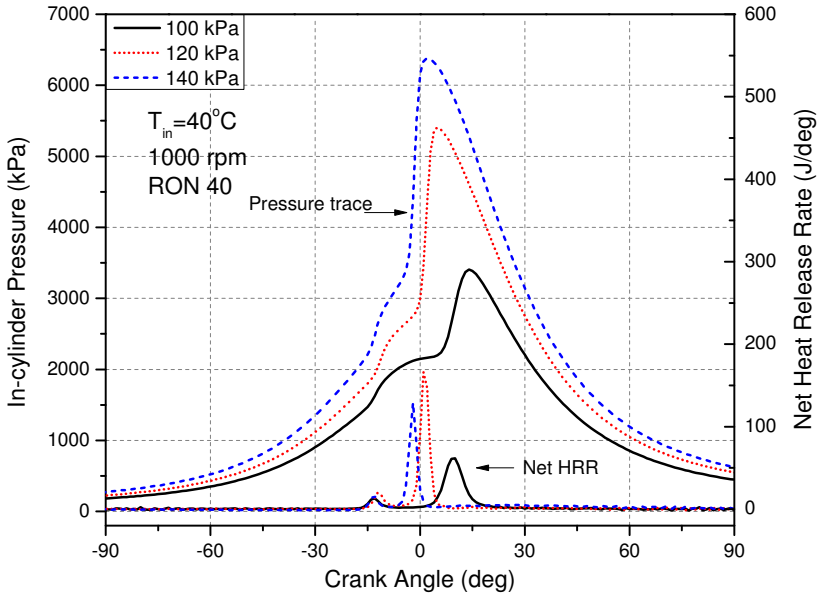

Figure 3.24: Pressure and heat release rates for intake pressures 100 kPa, 120 kPa and 140 kPa at 1000 rpm and RON 40

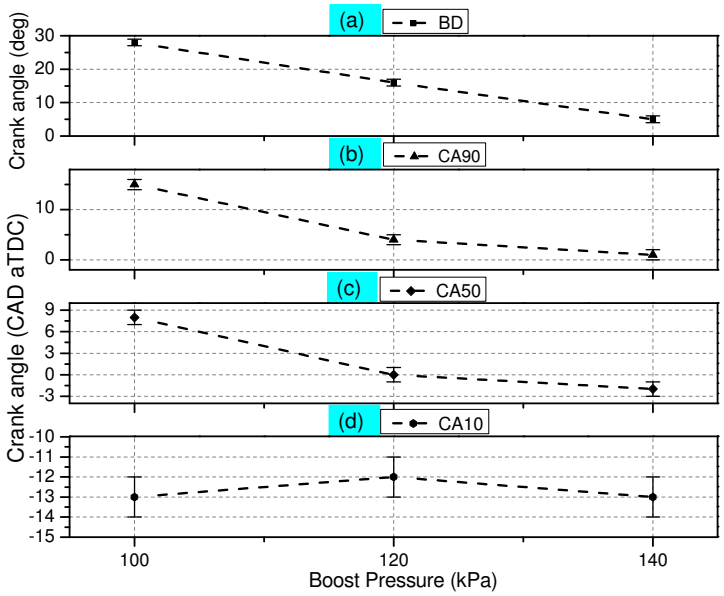

Figure 3.25: Effects of intake pressure on combustion characteristics (CA10 CA50, CA90 and Burn Duration) for HCCI combustion regime

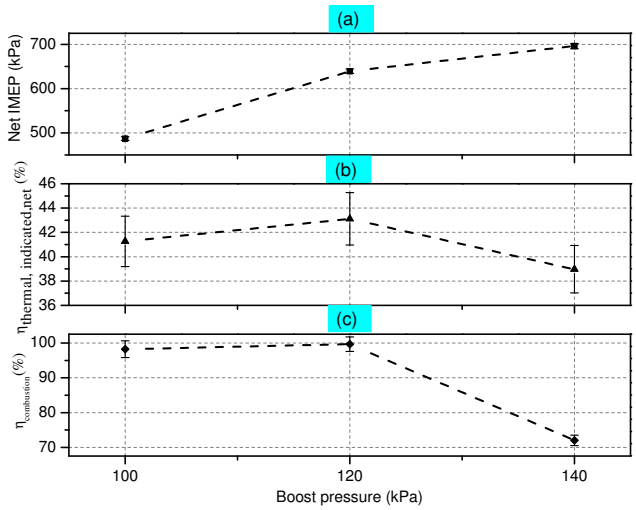

Figure 3.26: Effects of the boost pressure on (a) IMEP, (b) Indicated thermal efficiency and (c) Combustion efficiency for HCCI combustion regime

Chapter 4

Reactivity Controlled Compression Ignition (RCCI)

This chapter presents an overview of the Reactivity Controlled Compression Ignition (RCCI) combustion regime. RCCI has an advantage over other LTC combustion regimes in that the combustion phasing can be controlled by the start of injection of the fuel injected directly into the cylinder. Moreover, the fuel reactivity can be modified based on the engine speed and load allowing a much stable low temperature combustion for low load applications [62]. This chapter explores the engine maps for efficiency and combustion for three different premixed ratios 20, 40 and 60 for RCCI combustion regime over a range of speed and load conditions. The maps are based on constraints with all data points over 8 bar/CAD of MPRR and 10 % COV_{IMEP}

[61] are eliminated. The operating conditions for the tests are represented in Table 4.1.

Table 4.1
Operating Parameters for RCCI Combustion mode

Parameter	Operating Conditions
Intake Air temperature	40, 60, 80 (°C)
Manifold Pressure	120, 140 (kPa)
Engine Speed	800:200:3200 (rpm)
PR of Fuel	20, 40, 60 (-)
Lambda	1.0- 4.2(-)

4.1 Parametrization of BMEP using Flynn-Chen Model for RCCI combustion regime

Figure4.1 compares the experimental FMEP vs parameterized FMEP for RCCI combustion regime. It can be seen that the FMEP can be estimated within an error of 14%.

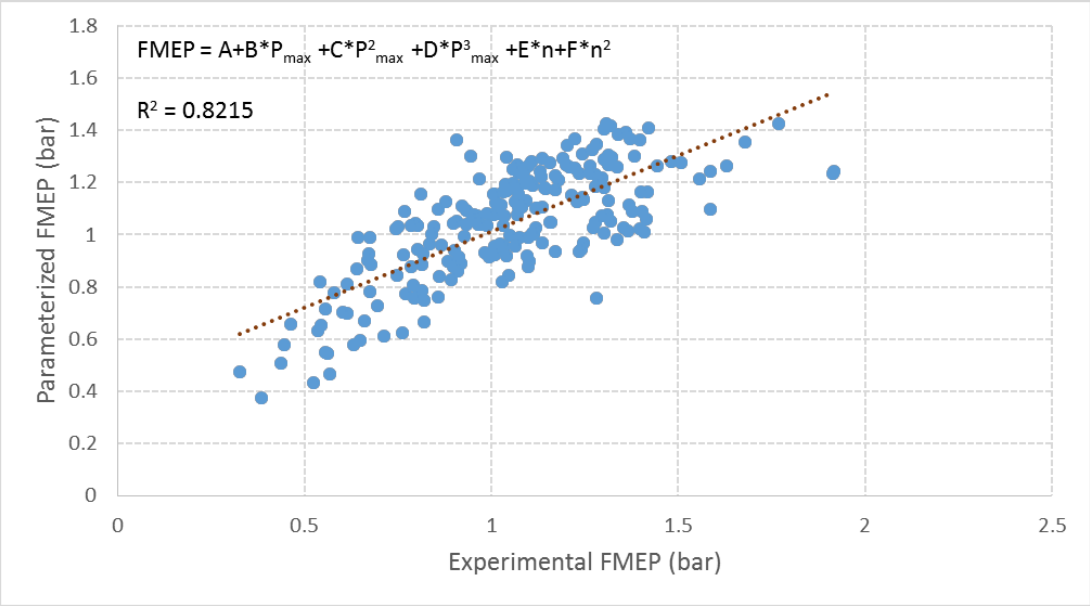

Figure 4.1: Experimental FMEP vs Parameterized FMEP

Table 4.2
Error in estimation of FMEP

Model	**Chen-Flynn with P^2_{max} and P^3_{max}**
Mean relative error	14 %
Max relative error	41 %
Max absolute error	0.7 bar

Table 4.3
Coefficients for the Flynn- Chen Model

Coefficient	Value
A	-2.9371
B	0.0016
C	-0.002
D	9.19E-6
E	0.0806
F	-0.0042

Based on the parametrized model for FMEP, the constants obtained for the Chen-Flynn model are given in Table 4.3.

4.2 Operating Range

RCCI operation over a range of engine speeds and loads was achieved based on a systematic procedure followed to run the tests. The injection pressure for both the DI and the PFI rails were held constant at 100 bar and 3 bar, respectively. The SOI timing was advanced with increase in engine speed. All tests were performed by monitoring the CA50 online and trying to maintain a constant combustion phasing of 5-8 deg aTDC. Figure 4.2 shows the operating range map in terms of equivalence ratio, engine speed and load limits for T_{intake} of 40 °C and boost pressure of 140 kPa. The operating map shows that the speed range for RCCI mode gets narrower with an

increase in PR. This is mainly because the reactive fuel quantity (n-heptane) reduces with an increase in PR. Therefore, the combustion becomes unstable at speeds higher than 1400 rpm for PR 60. It can also be seen that the engine could be run much leaner for a lambda of 5.21 at PR 20 as compared to 4.41 at PR 60. The lean limit for lower PR is much higher because of the combustion stability with the high reactive fuel dominance.

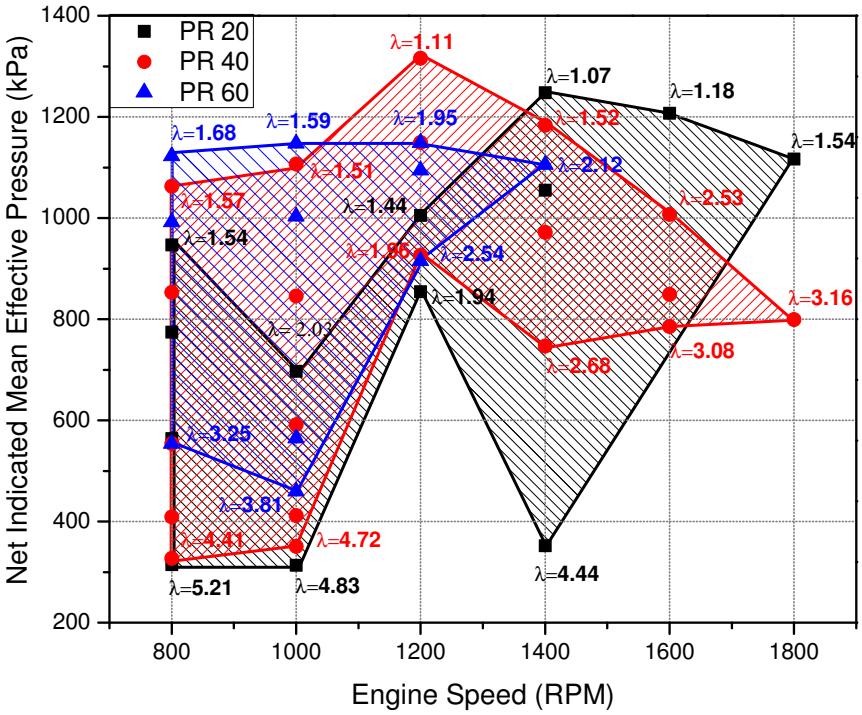

Figure 4.2: RCCI IMEP and speed range for 40 °C intake air temperature and boost pressure of 140 kPa

Figure 4.3 represents the operating range map for an intake temperature of 60 °C

and an intake pressure of 140 kPa. It can be observed that the lean limit for PR 20 is pushed further to a lambda value of 6.27 at 800 rpm. This is mainly due to the increased temperature of the intake charge at IVC. Moreover, the speed range for all three PRs is improved with an increase in intake temperature.

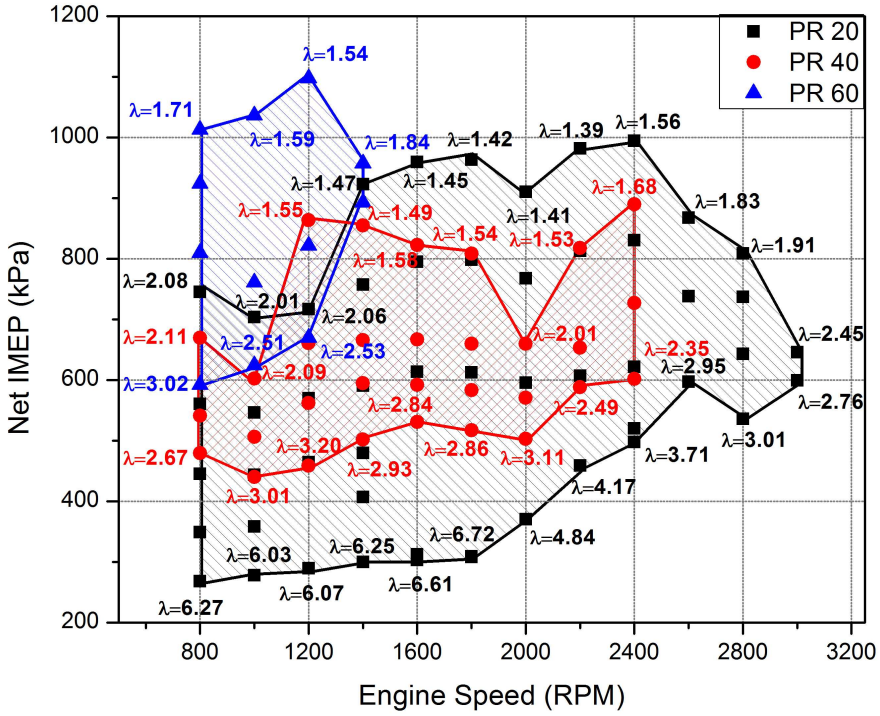

Figure 4.3: RCCI IMEP and speed range for 60 °C intake air temperature and boost pressure of 140 kPa

4.3 Maps for ISFC, BSFC, Indicated Thermal efficiency and Exhaust gas temperature

The ISFC maps for RCCI mode at T_{intake} of 40 °C and P_{intake} of 140 kPa for all three PRs are shown in Figure 4.4. It can be seen that the best ISFC points shift towards higher load conditions at an engine speed of 1400 rpm with an increase in PR of the fuel blends. Lower load performance for PR 20 is diesel like and the ISFC improves with load. It is also observed that the ISFC values are higher at low loads and low speeds for PR 60. This is due to the fact that the combustion efficiency drops at low loads and low speeds due to the ultra-lean air-fuel mixture. This results in a decreased combustion temperature and thereby increasing the unburnt fuel at the exhaust.

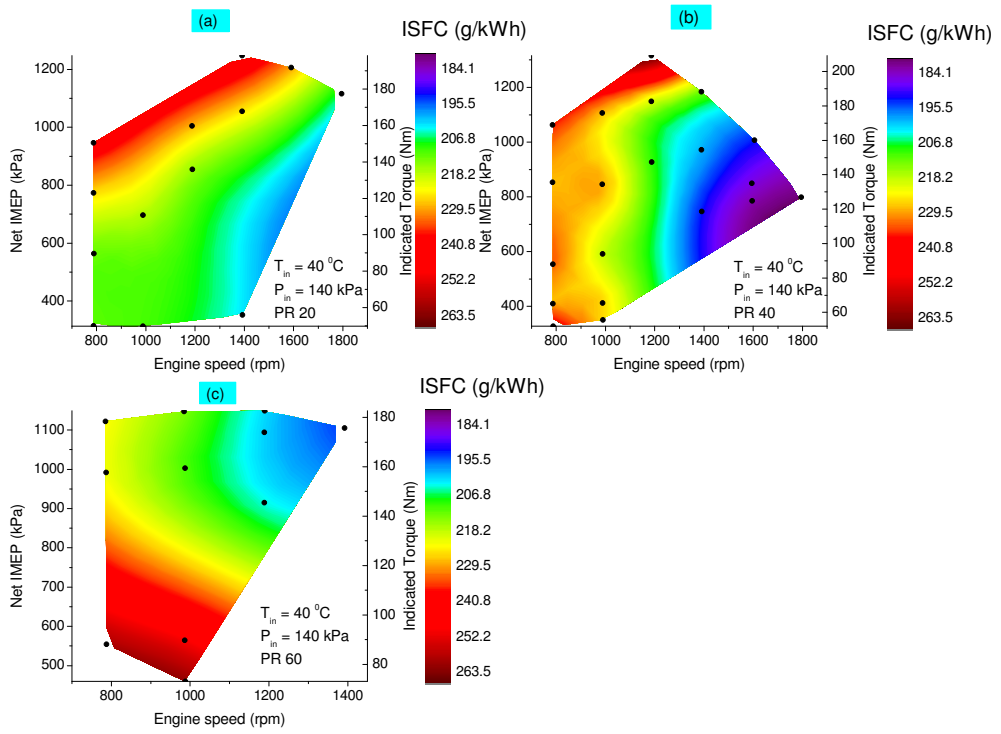

Figure 4.4: RCCI ISFC map for three PRs at 40 °C intake air temperature and intake pressure of 140 kPa

The BSFC maps were parameterized from the Flynn- Chen model and are represented in Figure 4.5 for the same operating conditions. The combustion efficiency was relatively lower at 75% for low loads and low engine speeds, as a result of which an increase in BSFC is observed for all three PRs. The range of BSFC was 230-325 g/kWh with the best BSFC occurring at high speeds and high loads for all PRs. It can be seen that the BMEP increases with increase in fuel energy content per cycle.

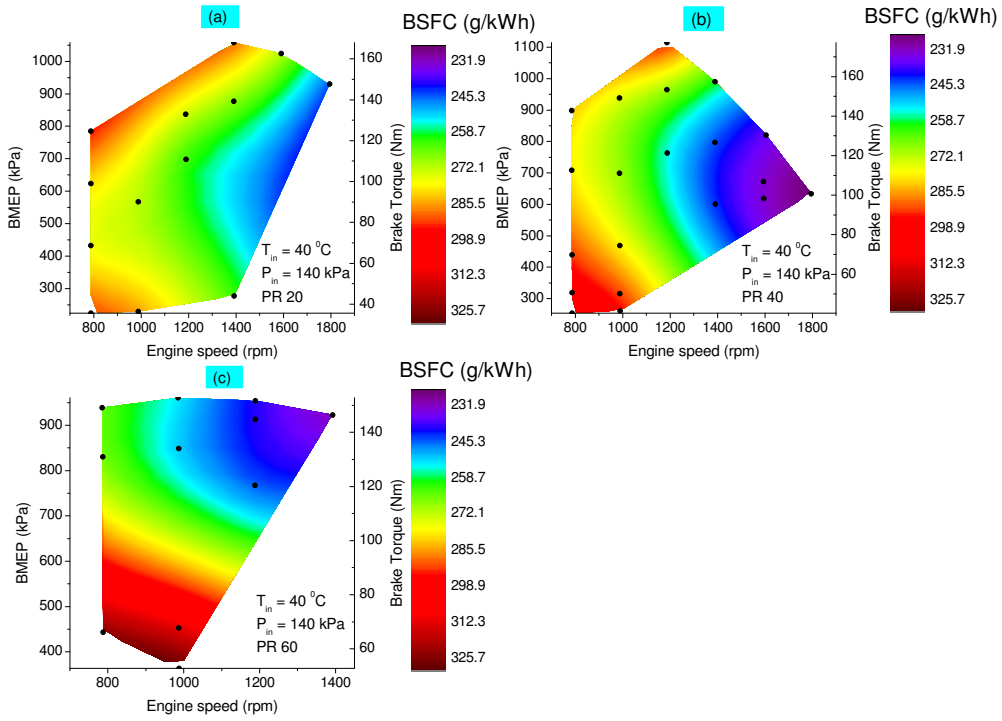

Figure 4.5: RCCI BSFC map for three PRs at 40 °C intake air temperature and 140 kPa intake pressure

Figure 4.6 shows a comparison of indicated thermal efficiencies for the RCCI mode for the same operating conditions. It can be seen that the thermal efficiency improves with load. The maximum thermal efficiency for this map was 45% at 1800 rpm and 120 Nm load for PR 40, which is 5% better than the $\eta_{th,ind}$ for PR 20 at the same speed-load condition. The compression ratio of the engine, pumping losses and specific heat ratio play crucial roles in determining the thermal efficiency [32]. For 1800 rpm and 120 kPa for PR 40, the heat transfer losses are significantly reduced

due to high engine speed. Thereby, the ratio of specific heat is higher with a lower in-cylinder temperature. This results in better combustion efficiency and thereby increasing the thermal efficiency.

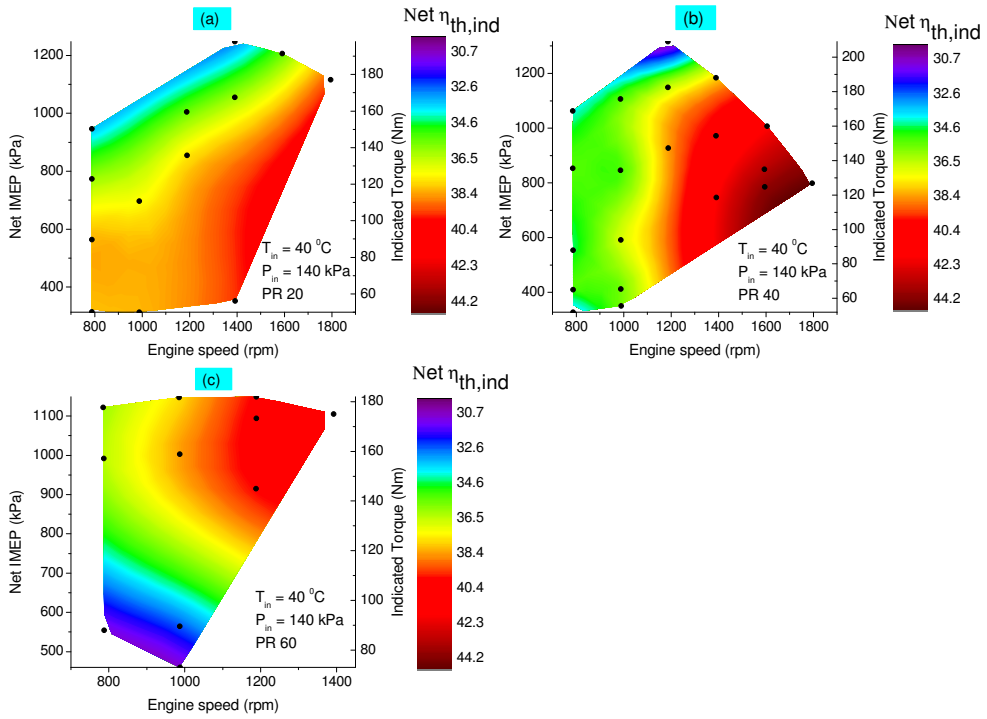

Figure 4.6: RCCI Indicated thermal efficiency map for three PRs at 40 °C intake air temperature and 140 kPa intake pressure

For RCCI combustion regime, the exhaust temperature map is shown in Figure 4.7. It can be seen that at lower loads and lower speeds, $T_{exhaust}$ is less than 200 °C, which implies less capability to reach to catalyst light off temperatures and poses a challenge with respect to the functioning of the oxidation catalysts. However, it can be seen

that the temperatures increase as high as 570 °C at higher speeds and loads. This is the typical temperature at which most SI engines work, at mid- high load conditions. For PR 20, at loads higher than 80 Nm for all engine speeds, the $T_{exhaust}$ is higher than the catalyst light off temperature of the oxidation catalyst. The $T_{exhaust}$ range is much wider as compared to that in the HCCI combustion regime.

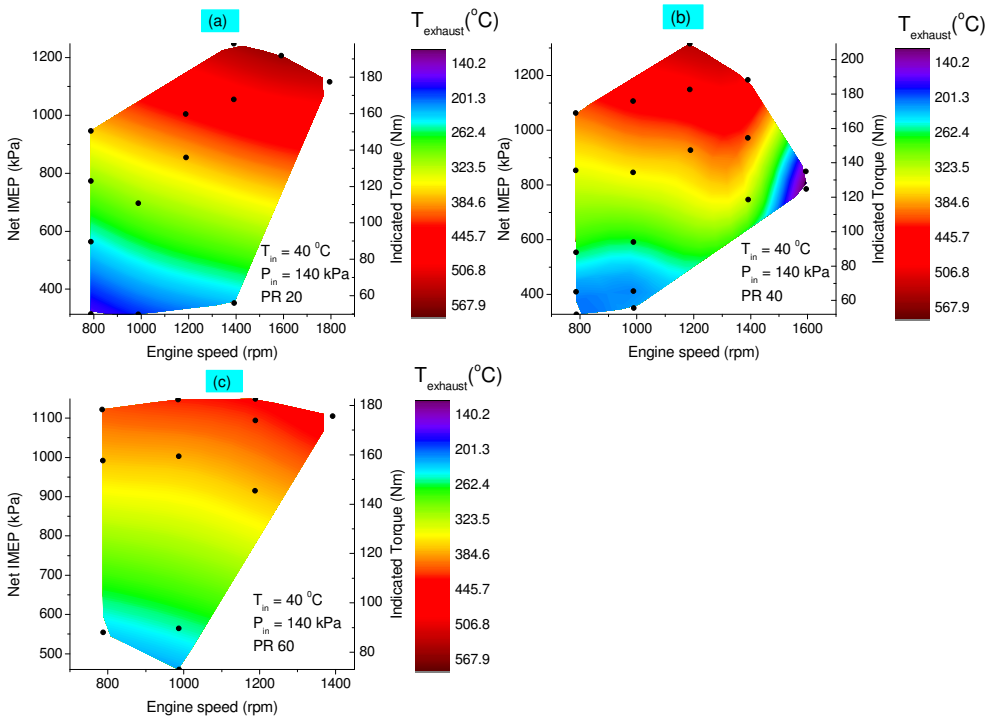

Figure 4.7: RCCI Exhaust gas temperature map for three PRs at 40 °C intake air temperature and 140 kPa boost pressure

4.4 Optimized RCCI maps

The data points for RCCI combustion regime were optimized by considering data points with best ISFC at each speed-load condition. Maps for BSFC, $\eta_{th,ind}$ and T_{exh} were evaluated for the same optimized set of data points. Figures 4.8 and 4.9 represent the optimized RCCI map for ISFC for naturally aspirated and boosted conditions, respectively. It is evident that the speed and load range could be extended with boosting. In order to obtain the best ISFC for Naturally aspirated conditions, the engine should be run within the load range of 70-120 Nm, where an ISFC of 180 g/kWh was obtained. At 1400 rpm and 100 Nm indicated torque, the lowest ISFC of 175 g/kWh was obtained. This data point was run with a combustion phasing of 7 CAD aTDC and had the best indicated thermal efficiency of 46 %. The start of injection was varied to keep the combustion phasing between 5-8 CAD aTDC. Moreover, the mass of fuel unburnt was less than 3 % for this data point. This shows that both combustion efficiency and combustion phasing play a crucial role in attaining the optimal ISFC at a given speed-load condition. For boosted conditions, the speed range was extended to 3400 rpm, while the load range was extended to 210 Nm indicated torque. With this range expansion, the best ISFC was shifted to higher engine speeds and loads as compared to the ISFC map for naturally aspirated conditions. At 140 kPa intake pressure, 2400 rpm engine speed and 80 Nm indicated torque, an ISFC of 176 g/kWh was obtained. It can be seen that the SOI was advanced

to 65 CAD bTDC for this operating condition, in order to maintain a CA50 of 10 CAD aTDC. Moreover, the engine was run at a PR of 60. Thereby, with lower in-cylinder temperatures and a two stage HTHR, the combustion was complete with a combustion efficiency of 98%. With such an optimized set of operating conditions, the thermal efficiencies and henceforth the ISFC seemed to improve considerably.

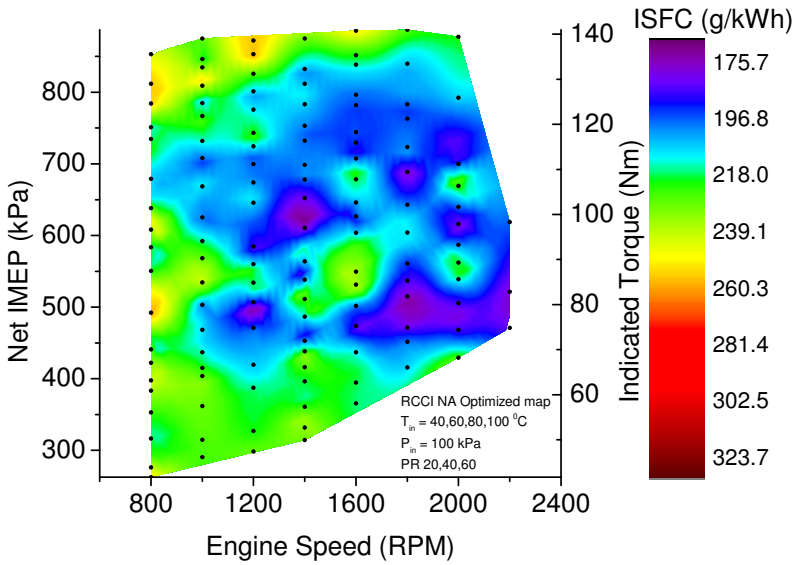

Figure 4.8: RCCI ISFC optimized map for all intake air temperatures and PRs for naturally aspirated conditions

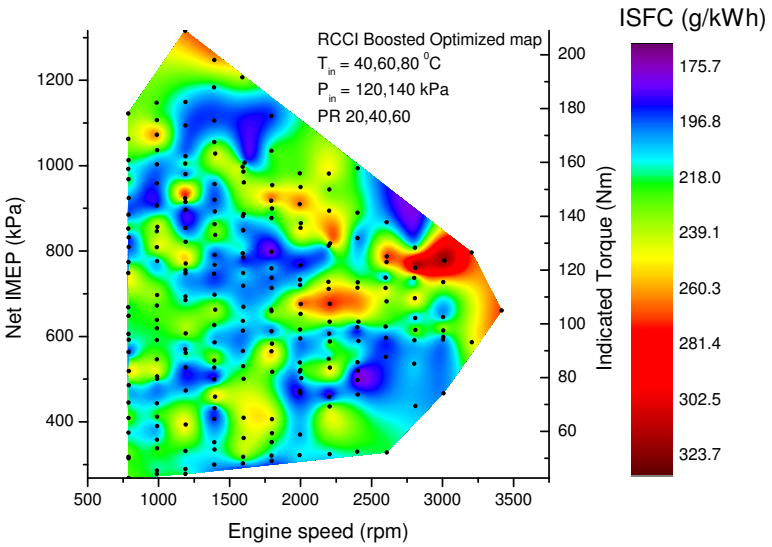

Figure 4.9: RCCI ISFC optimized map for all intake air temperatures and PRs at 140 kPa boost pressure

The BSFC maps as a function of engine speed and load are shown in Figures 4.10 and 4.11 for naturally aspirated and boosted conditions, respectively. It can be seen that with boosted conditions for the lower speeds, the engine could be run at lower loads as compared to naturally aspirated. This correlates to the lower equivalence ratio at boosted conditions, due to the increased density of the air inducted into the cylinder, making the mixture oxygen-rich and thereby leaner. However, the combustion efficiencies at these points were relatively lower, thereby justifying the higher values of BSFC.

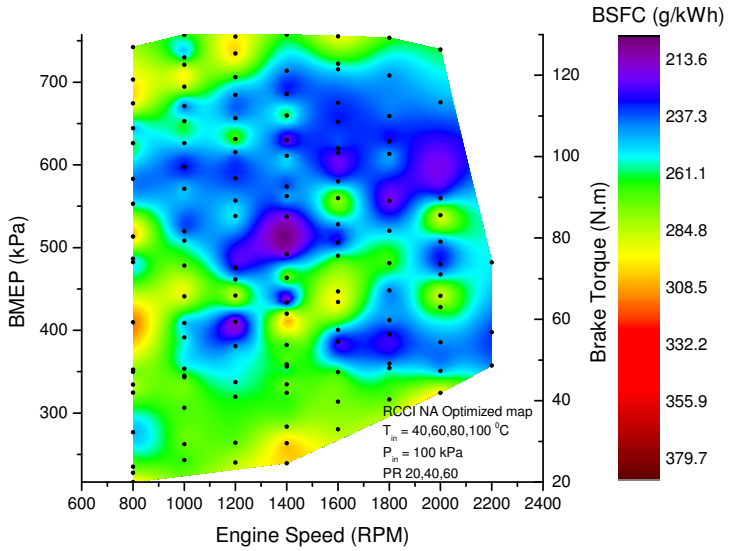

Figure 4.10: RCCI BSFC optimized map for all intake air temperatures and PRs at naturally aspirated conditions

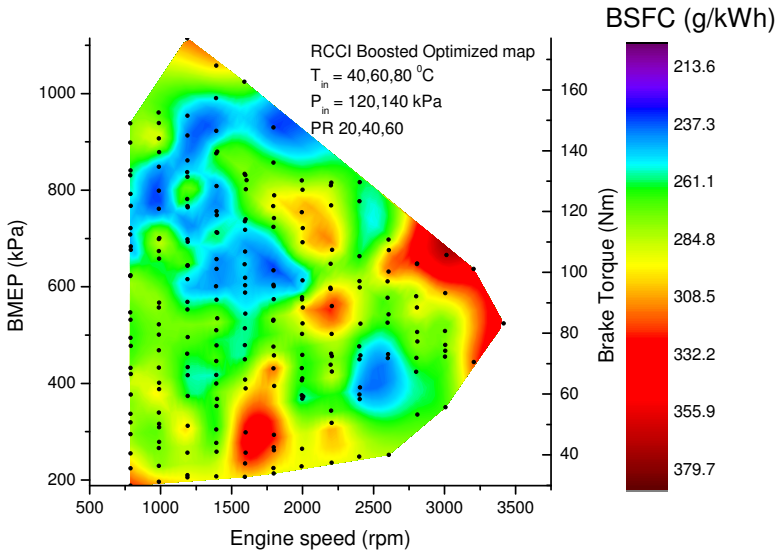

Figure 4.11: RCCI BSFC optimized map for all intake air temperatures and PRs at 140 kPa intake pressure

The most significant observation for RCCI combustion regime is the higher $\eta_{th,ind}$ at a wide range of speed-load conditions. This can be observed in Figures 4.12 and 4.13 for naturally aspirated and boosted conditions, respectively. The $\eta_{th,ind}$ is quite high for high speed-load conditions. The lower equivalence ratio at low speeds and lowest loads comes with the price of decreased stability and efficiency. The start of injection pays a crucial role in determining the combustion phasing. As seen through the data, it is advisable to keep the combustion phasing not greater than 10 CAD aTDC. The combustion efficiencies tend to drop beyond this point. At low speeds such as 800 rpm, the Start of injection is 18 CAD bTDC, which is too late. However, this is the optimal SOI for which the desirable combustion phasing could be achieved. The low thermal efficiency at low speeds could be because of insufficient time for the n-heptane and iso-octane to mix, thereby leading to unburnt fuel over 15% in the exhaust.

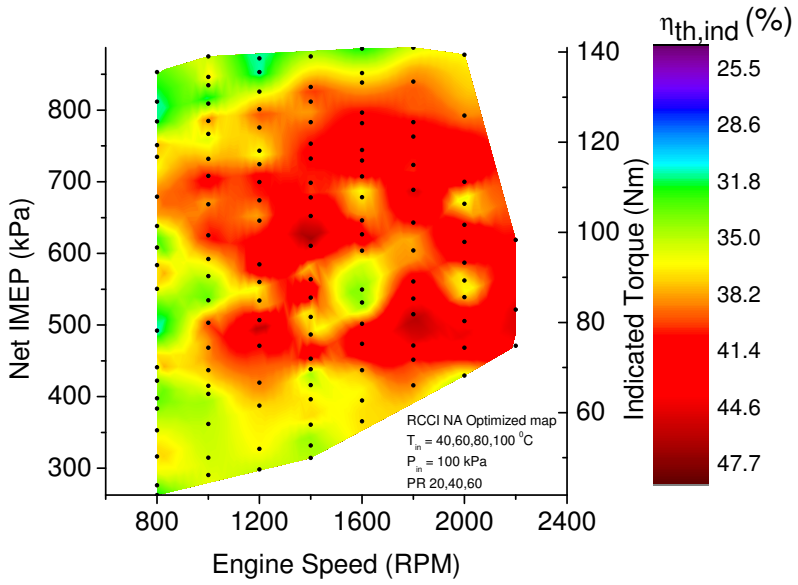

Figure 4.12: RCCI indicated thermal efficiency optimized map for all intake air temperatures and PRs at naturally aspirated conditions

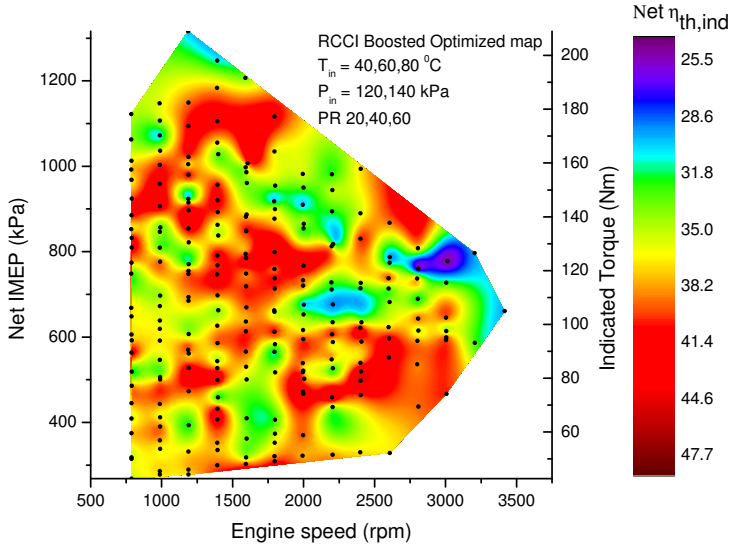

Figure 4.13: RCCI indicated thermal efficiency optimized map for all intake air temperatures and PRs at 140 kPa intake pressure

The optimized exhaust temperature maps for naturally aspirated and boosted conditions are illustrated in Figures 4.14 and 4.15, respectively. The lower and upper limits for the temperatures are 190 °C and 720 °C, respectively. With an increase in engine speed and load, the $T_{exhaust}$ increases. At loads higher than 70 Nm and all engine speeds, the exhaust energy can be recovered to either run the turbocharger or to develop a waste heat recovery system to heat the intake air.

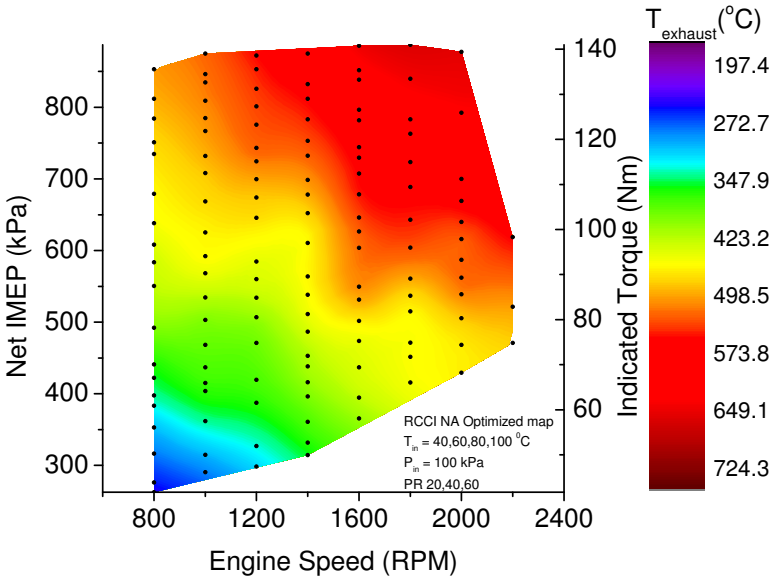

Figure 4.14: RCCI exhaust temperature optimized map for all intake air temperatures and PRs at naturally aspirated conditions

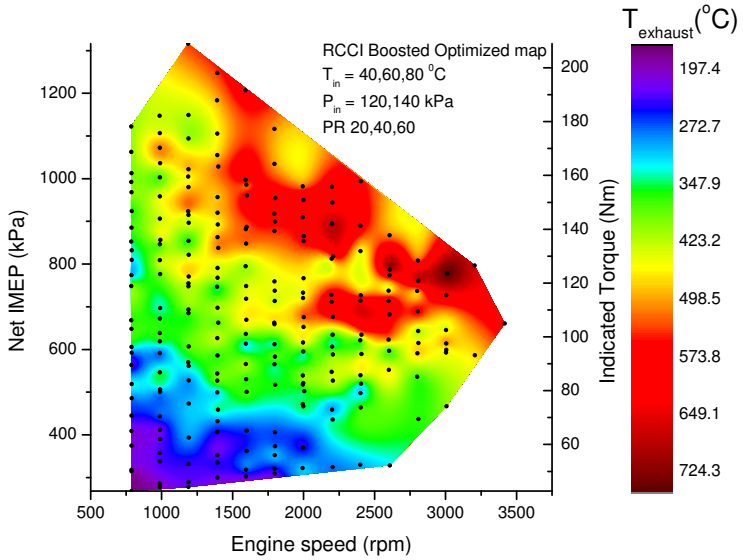

Figure 4.15: HCCI exhaust temperature optimized map for all intake air temperatures and PRs at 140 kPa intake pressure

4.5 RCCI optimized maps with supercharger losses accounted

The RCCI tests for boosted conditions were performed using an e-supercharger, which was driven by an electric motor. This energy consumed by the supercharger was unaccounted for, in the maps represented in Section 4.3. This section provides an overview of the change in the performance parameters, fuel consumption assuming the supercharger was mounted on the engine and drawing power from the engine

crankshaft. The supercharger efficiency was considered constant with a value of 0.6 [37]. The power consumed at each engine speed and boost pressure is illustrated in Section 2.8. Based on these values the Net Power from the engine was calculated by deducting the losses from the supercharger. Figure 4.16 represents the optimized ISFC map with the supercharger losses accounted for. It can be seen that the best ISFC point shifted from 175 to 225 g/kWh after accounting for the losses. Moreover, given that the engine power output is lower at low engine speeds, the best ISFC for a given engine speed occurs at low power and the ISFC values increase at higher loads. Therefore it can be seen that the ISFC values increased roughly by 30% after the losses were accounted for. Moreover, the peak thermal efficiency dropped from 47% to 37%, which is approximately a 10 % reduction. This provides a good incentive to use RCCI exhaust energy (in Figures 4.14 and 4.15) for turbocharging the engine instead of using a supercharger.

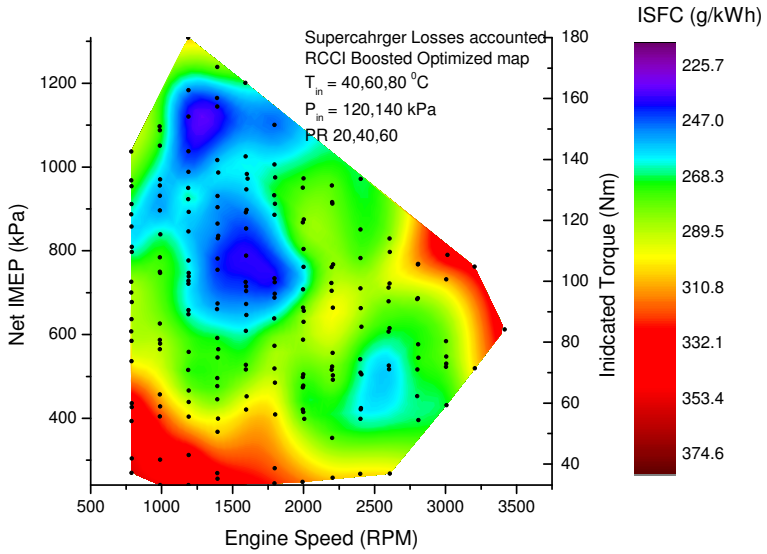

Figure 4.16: Optimized ISFC map for RCCI combustion regime with supercharger losses accounted for

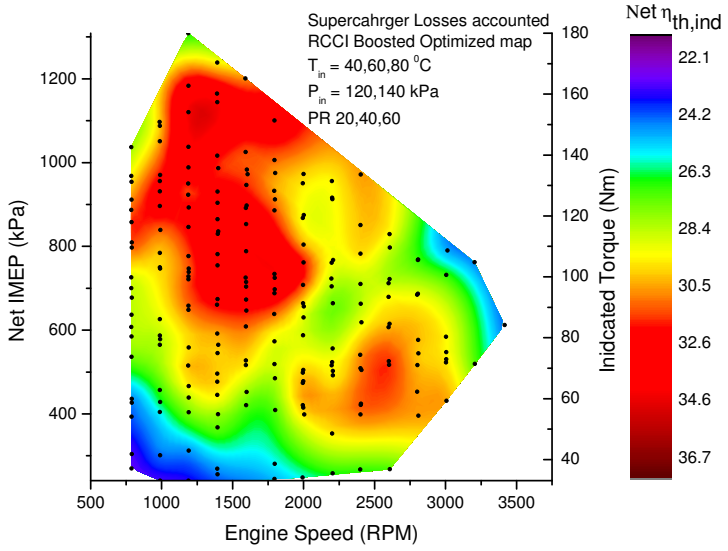

Figure 4.17: Optimized $\eta_{th,ind}$ map for RCCI combustion regime with supercharger losses accounted for

4.6 RCCI optimized maps with COV of IMEP less than 5 percent

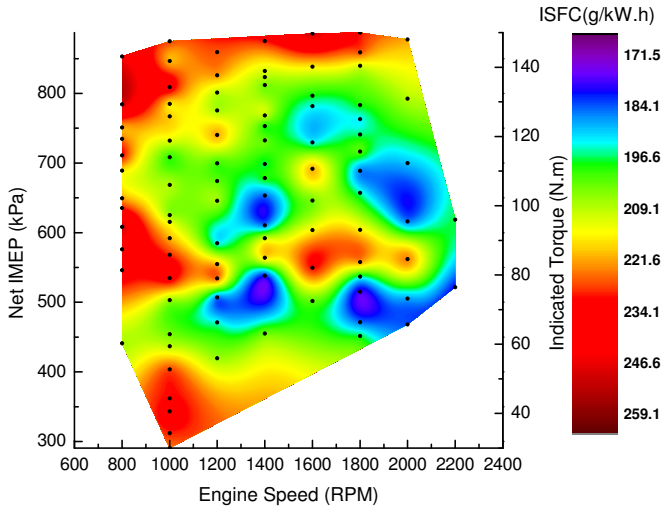

Figure 4.18: ISFC optimized map for RCCI combustion regime for COV of IMEP less than 5% at naturally aspirated conditions

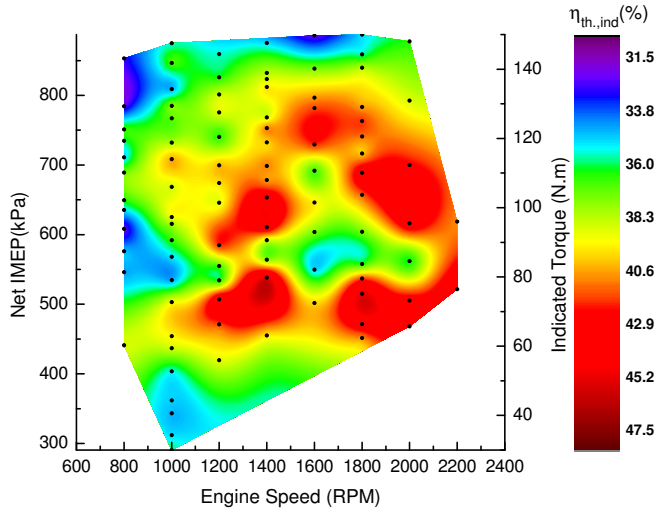

Figure 4.19: Indicated thermal efficiency optimized map for RCCI combustion regime for COV of IMEP less than 5% at naturally aspirated conditions

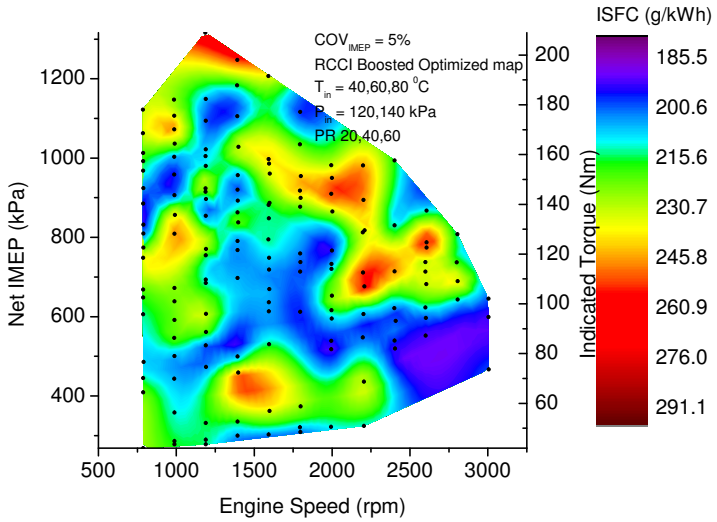

Figure 4.20: ISFC optimized map for RCCI combustion regime for COV of IMEP less than 5% and boosted conditions

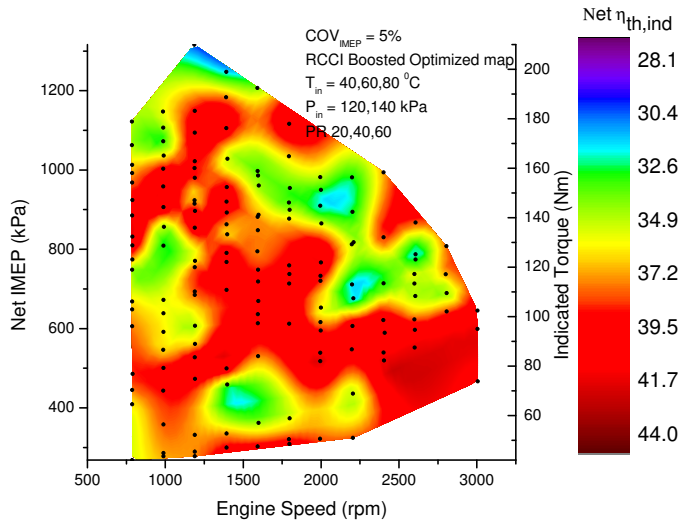

Figure 4.21: Indicated thermal efficiency optimized map for RCCI combustion regime for COV of IMEP less than 5% and boosted conditions

4.7 Effects of PR on RCCI combustion

This section discusses the effect of premixed ratio (PR) on the combustion characteristics and performance metrics of RCCI combustion regime, with premixed ratios of 20, 40 and 60. The start of injection was held constant at 25 CAD bTDC and the tests were performed at the constant total fuel energy. The operating conditions for performing these tests are given in Table 4.4.

Table 4.4
Operating conditions used for the experiments to study the effect of PR on RCCI combustion

Test Parameters	Value/ Unit
Engine Speed	1000 (rpm)
Injection Pressure	100 (bar)
SOI	25 (deg bTDC)
Fuel Type	PR 20, 40, 60
IVO	25.5 (deg bTDC)
EVC	22 (deg bTDC)
Throttle Body Position	100 (%)
Intake Air Temperature	60 (°C)
Fuel Mass	18 (mg/cycle)
Intake Pressure	120 (kPa)

Figure 4.22 illustrates the pressure trace and heat release rate curves for the three PRs used. It can be observed that the peak in-cylinder pressure decreases with an increase in PR. Moreover, the location of peak pressure (LPP) gets retarded too. The heat release rate curve shows that there is a significant charge cooling at the time when n-heptane is injected into the cylinder at 25 CAD bTDC. With n-heptane being the more reactive fuel, with an increase in PR, the reactivity of mixture decreases resulting in the combustion phasing to be retarded as illustrated in Figure 4.22 and Figure 4.24. It can be seen that the CA50 changes from 10 to 15 CAD aTDC as the PR is increased from 20 to 60. Further owing to the reduced reactivity of fuel at higher PR, the burn duration (BD) also increases indicating that the combustion rate is slower as compared to lower PRs.

An interesting observation from the heat release rate curve is that for PR 60, there appears to be a two-stage high temperature heat release (HTHR), as shown in Figure 4.23. This can be attributed to the fact that the injection timing was too retarded bTDC. Iso-octane being injected much earlier in the port at 450 CAD bTDC, gets sufficient time to mix homogeneously with air and a part of it is consumed shortly after n-heptane is injected directly into the cylinder. The high pressure and temperature at TDC catalyzes this process resulting in the combustion of the mixture for the first stage of HTR. The remaining iso-octane is expected to get consumed after the TDC. Therefor the first stage heat release is mainly trigerred due to n-heptane being injected late in the cylinder. The first stage heat release triggers the the remainder mixture to burn and thereby resulting in the second stage HTR [63].

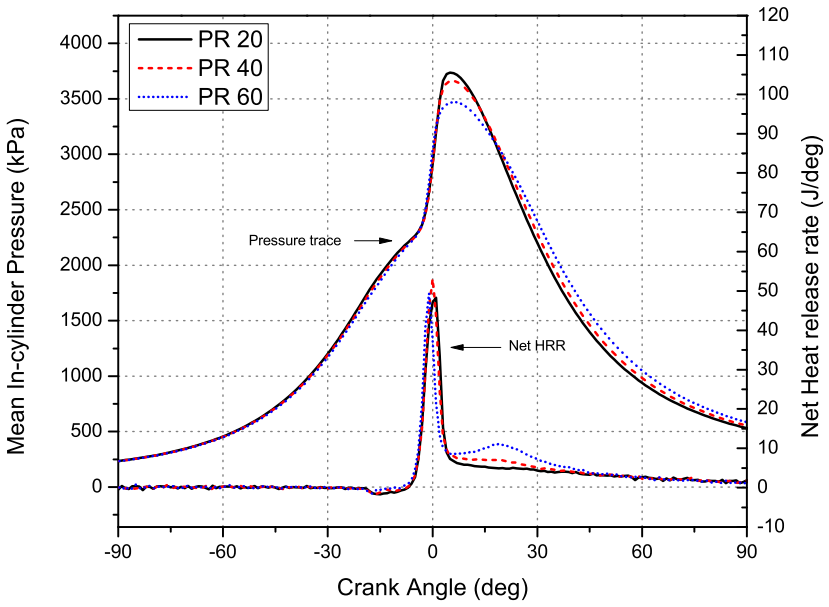

Figure 4.22: Pressure and heat release rates for PR 20, 40 and 60 for operating conditions listed in Table 4.4

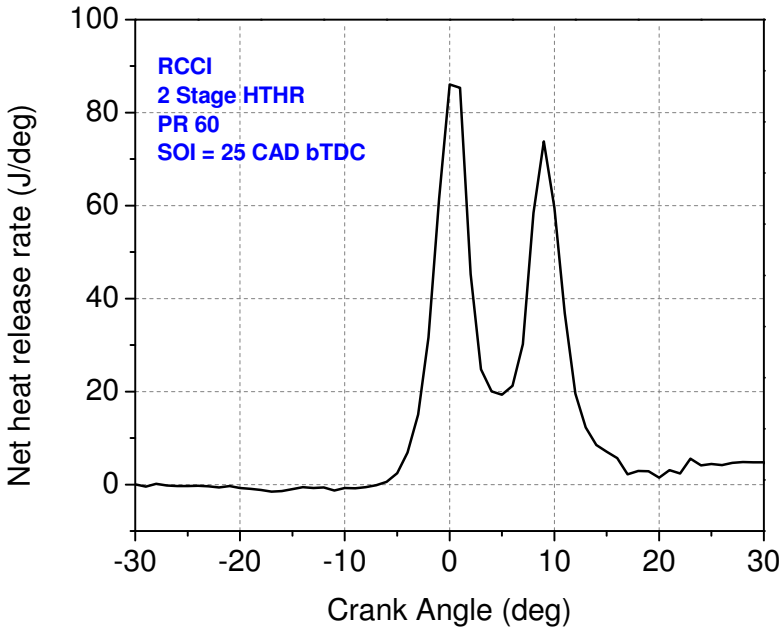

Figure 4.23: Heat release rate characteristics for RCCI combustion

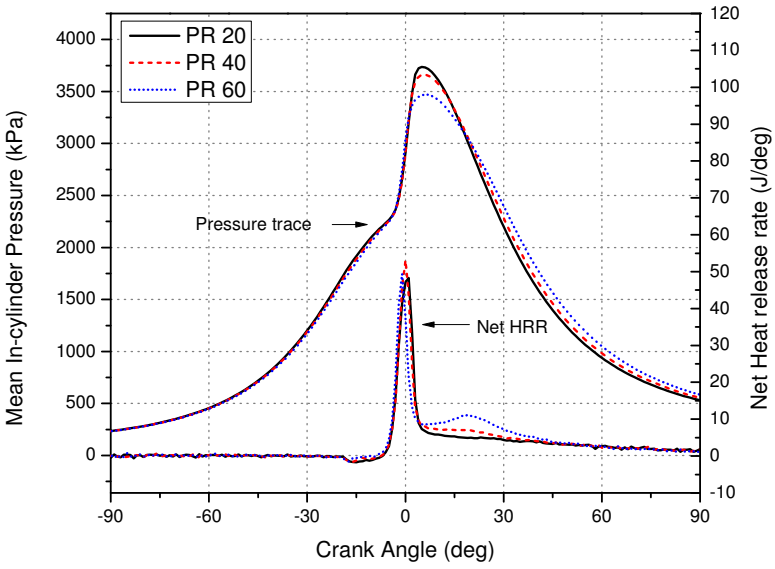

Figure 4.24: Effects of PR on combustion characteristics (CA10 CA50, CA90 and Burn Duration) for RCCI combustion regime

Figure 4.25 illustrates the effect of PR on the performance metrics. Owing to the increase in the effective area under the curve for the HRR, IMEP increases from 460 kPa to 545 kPa for PR 20 and 60, respectively. Moreover, the indicated thermal efficiency increases with increase in PR because the in-cylinder temperature and pressure are lower for higher PRs due to the two-stage HTHR for PR 60. At lower PR, the indicated thermal efficiency is 29 % which is significantly low. This is due to the incompleteness of combustion [64], as the combustion efficiency is 69 % for PR20. The combustion efficiency lies in the range of 69% to80 %, indicating that with higher PR and the two stage HTHR, the completeness of combustion is much higher as compared to that in lower PRs.

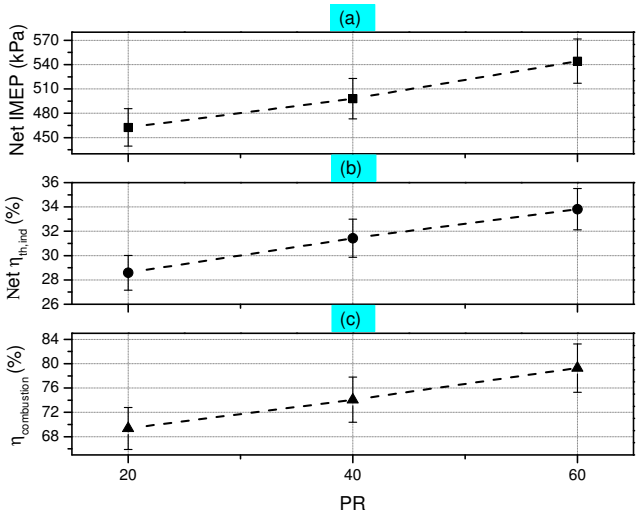

Figure 4.25: Effects of PR on (a) IMEP, (b) Indicated thermal efficiency and (c) Combustion efficiency for RCCI combustion regime

4.8 Effects of Intake Air Temperature on RCCI Combustion

This section discusses the effect of intake air temperature on RCCI combustion and performance metrics. Four different temperatures 40, 60, 80 and 100 °C are used. The operating conditions for these tests are given in Table 4.5.

Table 4.5
Operating conditions used for the experiments to study the effect of PR on RCCI combustion

Test Parameters	Value/ Unit
Engine Speed	1000 (rpm)
Injection Pressure	100 (bar)
SOI	25 (deg bTDC)
Fuel Type	PR 20
IVO	25.5 (deg bTDC)
EVC	22 (deg bTDC)
Throttle Body Position	100 (%)
Intake Air Temperature	40,60,80,100 (°C)
Fuel Mass	18 (mg/cycle)
Intake Pressure	120 (kPa)

The effect of intake temperature on the in-cylidner pressure and the Net HRR is shown in Figure 4.26. The maximum in-cylinder pressure increases with an increase in intake temperature. Further, the LPP is also advanced with an increase in T_{intake}.

Heating the intake air increases the charge temperature that is inducted into the cylinder. The reaction rate of the fuel molecules are higher at higher temperatures. Beyond a temperature of 80 °C, knocking was observed and the MPRR was higher than 8 bar/CAD.

As seen through Figures 4.26 and 4.27, the start of combustion (CA10) is advanced with an increase in T_{intake}. Owing to the higher charge temperatures, the mixture starts to combust earlier at higher T_{intake}. However, it can be observed that the CA50 is 10 CAD aTDC for T_{intake} of 40 °C, but with higher temperatures up to 100 °C, the CA50 remains constant at 8 CAD aTDC. This shows that T_{intake} has a negligible effect on CA50, which could probably be better quantified if a higher resolution crank angle encoder was used.

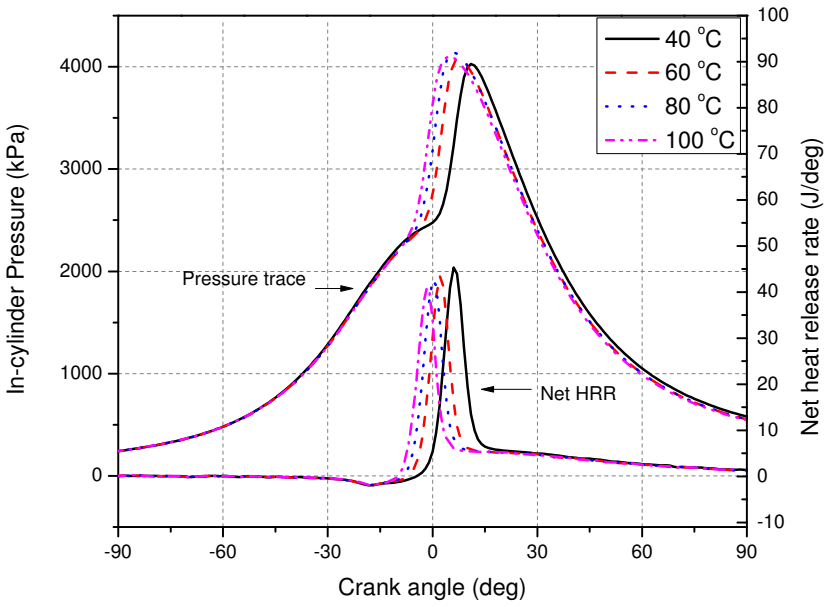

Figure 4.26: Pressure and heat release rates for PR 20 for operating conditions listed in Table 4.5

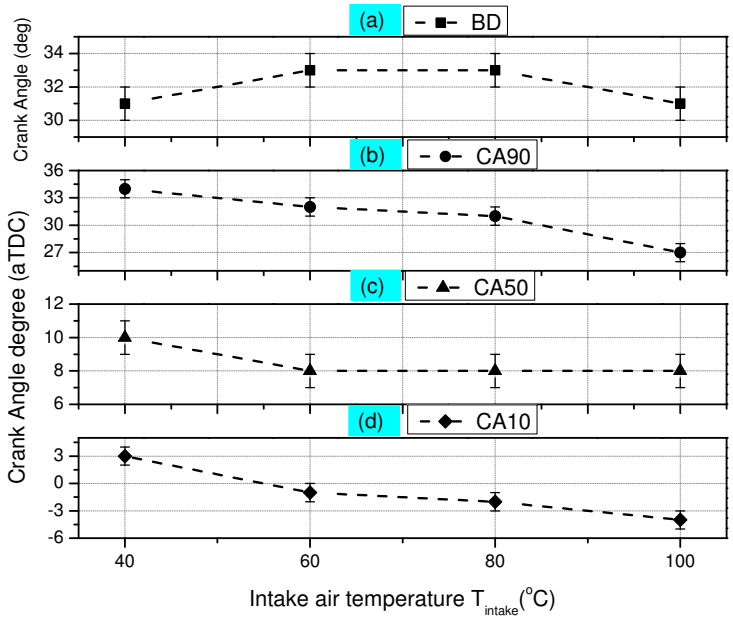

Figure 4.27: Effect of intake air temperature on combustion characteristics (CA10 CA50, CA90 and Burn Duration) for RCCI combustion regime

Figure 4.28 shows the effect of T_{intake} on the performance metrics of RCCI combustion. The net IMEP and indicated thermal efficiency reduce with an increase in T_{intake}, because of the higher in-cylinder temperatures at higher T_{intake}. The ratio of specific heats is reduced, decreasing the polytropic expansion coefficient and thereby the expansion work [46]. As seen in Figure 4.29, the combustion efficiency lies in the range of 72% to 75% for all T_{intake} values.

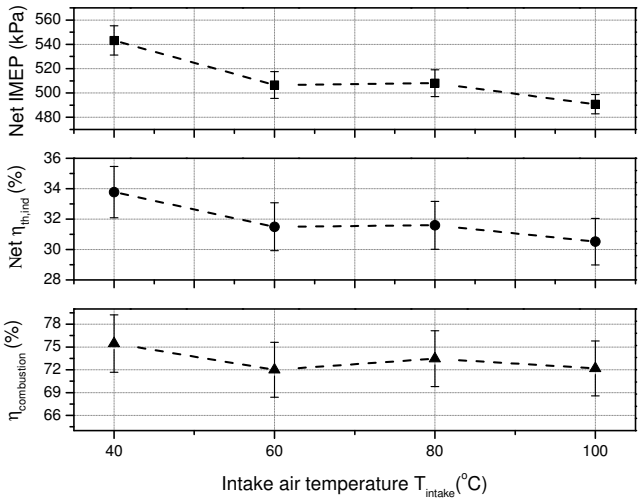

Figure 4.28: Effects of T_{intake} on (a) IMEP, (b) Indicated thermal efficiency and (c) Combustion efficiency for RCCI combustion regime

4.9 Effect of boost pressure on RCCI combustion

An investigation of the experimental results was conducted to study the effect of boost pressure on RCCI combustion, with the boost pressure varying from 100 kPa to 140 kPa. All experiments were performed at a constant fuel quantity and constant SOI as represented in Table 4.6.

Table 4.6
Operating conditions used for the experiments to study the effect of boost pressure on RCCI combustion

Test Parameters	Value/ Unit
Engine Speed	1000 (rpm)
Injection Pressure	100 (bar)
SOI	25 (deg bTDC)
Fuel Type	PR 20
IVO	25.5 (deg bTDC)
EVC	22 (deg bTDC)
Throttle Body Position	100 (%)
Intake Air Temperature	60 (°C)
Fuel Mass	15 (mg/cycle)
Intake Pressure	100,110,120,130,140 (kPa)

Figure 4.29 shows the effect of boost pressure on the in-cylinder pressure and heat release rate. It can be noted that the in-cylinder pressure increases with an increase in boost pressure and the LPP becomes more advanced towards TDC. The pressure and temperature at the end of compression stroke increases with an increase in boost pressure. The volume of air inducted increases with increase in boost pressure. This results in more charge energy being combusted in the cylinder.

As seen in Figures 4.29 and 4.30, the start of combustion (CA10) gets advanced significantly with increase in boost pressure. The combustion rates are faster at higher boost pressures due to stratification of the charge [32]. The thermal efficiency and net IMEP do not change significantly because the CA50 is obtained in the range of 8-12 CAD aTDC. The combustion efficiency lies between 75% to 80% between 100

kPa and 140 kPa boost pressures.

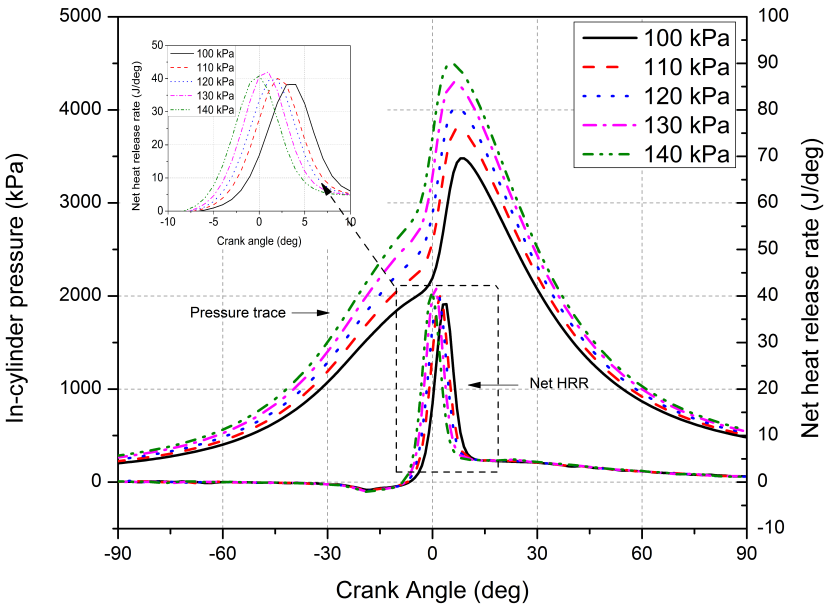

Figure 4.29: Pressure and heat release rates for PR 20 for operating conditions listed in Table 4.6

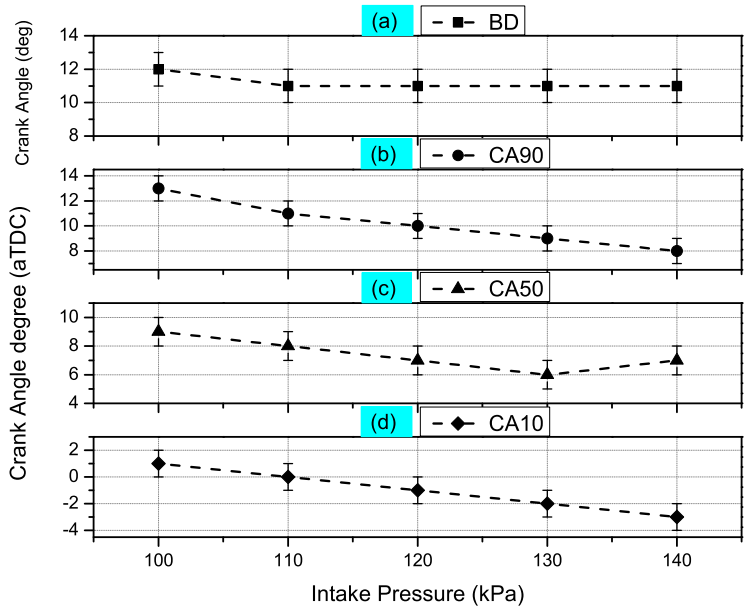

Figure 4.30: Effects of intake pressure on combustion characteristics (CA10 CA50, CA90 and Burn Duration) for RCCI combustion regime

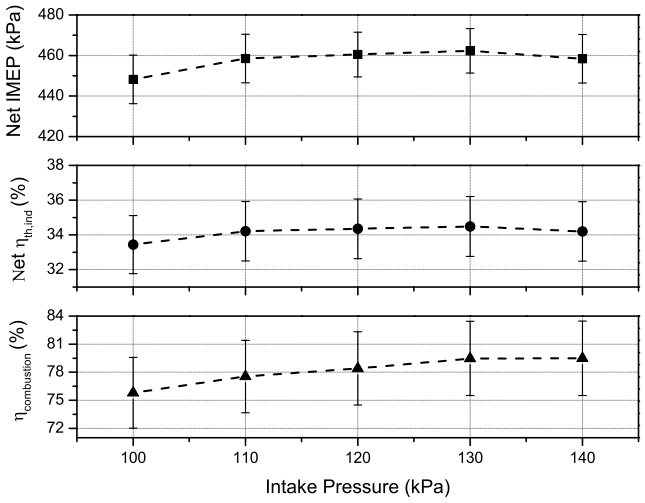

Figure 4.31: Effects of intake pressure on (a) IMEP, (b) Indicated Thermal efficiency and (c) Combustion efficiency for RCCI combustion regime

Chapter 5

Partially Premixed Compression Ignition (PPCI)

This chapter presents an investigation of the effect of various operating conditions on Partially Premixed Compression Ignition (PPCI) combustion mode. Engine maps were created to study the combustion and performance characteristics and the operating range of the engine running in PPCI combustion mode was determined. PPCI, also termed as early injection HCCI, aims to integrate the benefits of HCCI while improving the controllability of combustion phasing [51]. The ignition delay in PPCI is much longer than a CDI combustion regime but shorter than HCCI. The direct injection of the fuel into the cylinder can be used to control the combustion phasing [65]. The engine was tested in PPCI combustion mode in order to determine the

operating region of the engine. Operating parameters such as intake air temperature, boost pressure, engine speed, Research Octane number (RON) of fuel and equivalence ratio were varied. BSFC, exhaust gas temperature, ISFC and BSFC maps were created. The range of operating parameters are given in Table 5.1.

Table 5.1
Operating Parameters for PPCI Combustion Mode

Parameter	**Operating Conditions**
Intake Air Temperature	40, 60, 80, 100 (°C)
Manifold Pressure	95 (kPa)
Engine Speed	800:200:1800 (rpm)
RON of fuel	0, 20, 40 (-)
Lambda	1.4- 5.6 (-)

5.1 Parametrization of BMEP using Flynn-Chen Model for PPCI combustion regime

A plot of experimental FMEP vs parameterized FMEP based on Chen-Flynn model is shown in Figure5.1 for PPCI combustion regime indicating that the FMEP can be estimated with a relative error of 6%.

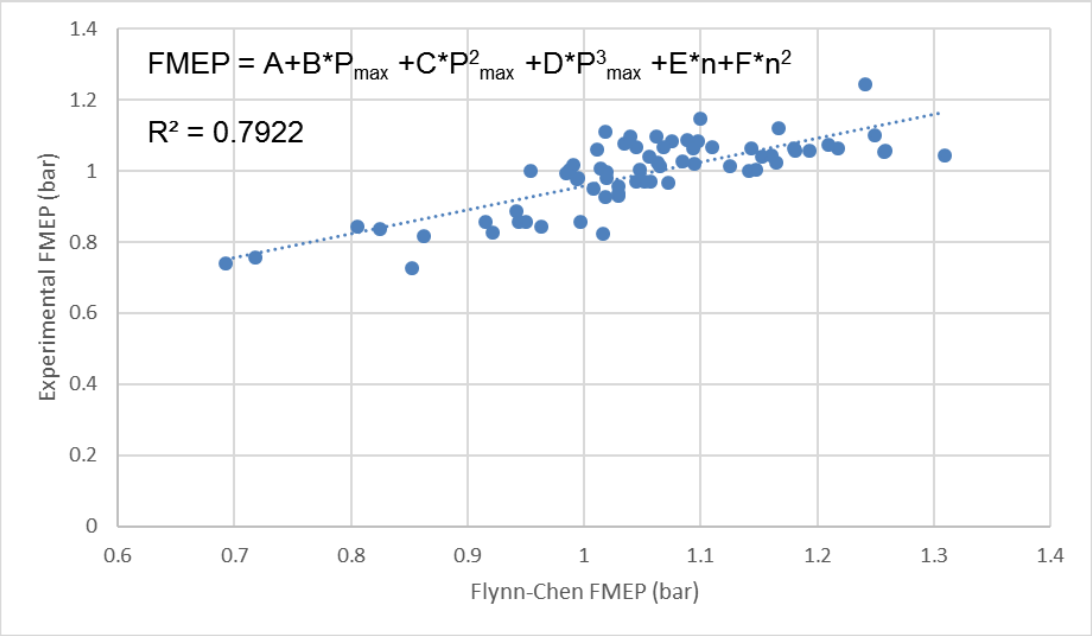

Figure 5.1: Experimental FMEP vs Parameterized FMEP

Table 5.2
Error in estimation of FMEP

Model	**Chen-Flynn with P^2_{max} and P^3_{max}**
Mean relative error	6 %
Max relative error	16 %
Max absolute error	0.17 bar

Table 5.3
Coefficients for the Flynn- Chen Model

Coefficient	Value
A	-2.088
B	0.2483
C	-0.0058
D	4.778E-5
E	-0.4747
F	0.0841

Based on the parametrized model for FMEP, the constants obtained for the Chen-Flynn model are given in Table 5.3.

5.2 Operating Range Maps

The operating range maps for three fuel compositions RON 0, 20 and 40 for two different intake air temperatures 40 °C and 80 °C are illustrated in Figure 5.2 and 5.3, respectively. At T_{intake} of 40 °C for the high octane fuel RON 40, the lean limit is 550 kPa at 800 rpm while it is 450 kPa at 800 rpm and 80 °C. It can be seen that the engine could be run at a very lean equivalence ratio at higher temperatures, thereby improving the operating range enabling the load limit to be pushed towards much leaner operating conditions. For both intake air temperatures, the range of engine speed is much larger for lower octane fuels RON 0 as compared to RON 40. However,

owing to the lower octane rating of RON 0, the upper limit of load was limited due to the knocking tendency of the fuel. Therefore, RON 0 was the best choice to run the engine at low load conditions, whereas RON 40 was efficient in running the engine at low-mid load conditions. Moreover, the speed range for all the fuels was limited due to the lower compression ratio of 9.2:1 being used for the engine.

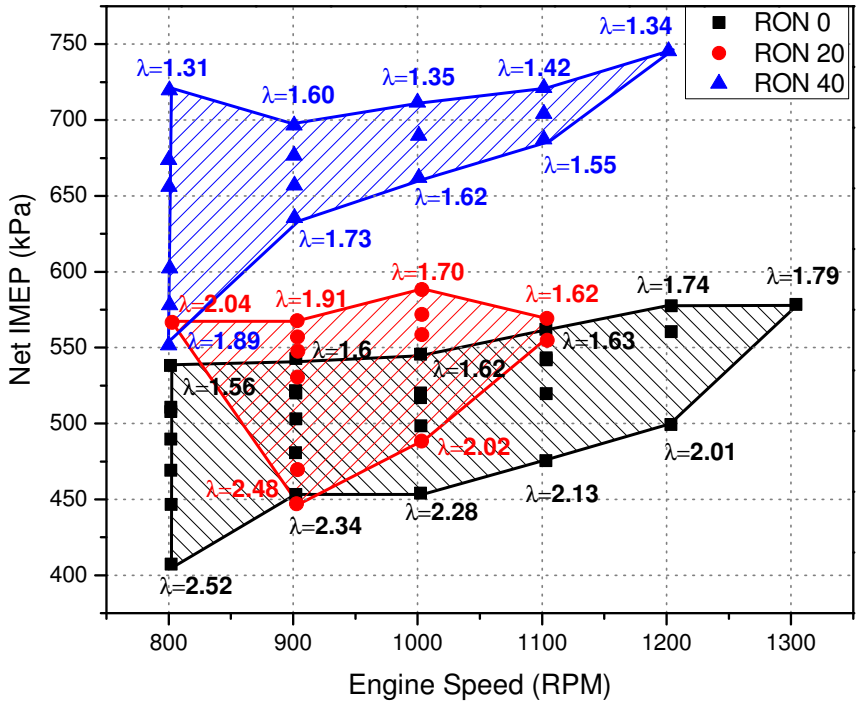

Figure 5.2: PPCI IMEP and speed range for 40 °C intake air temperature at naturally aspirated conditions

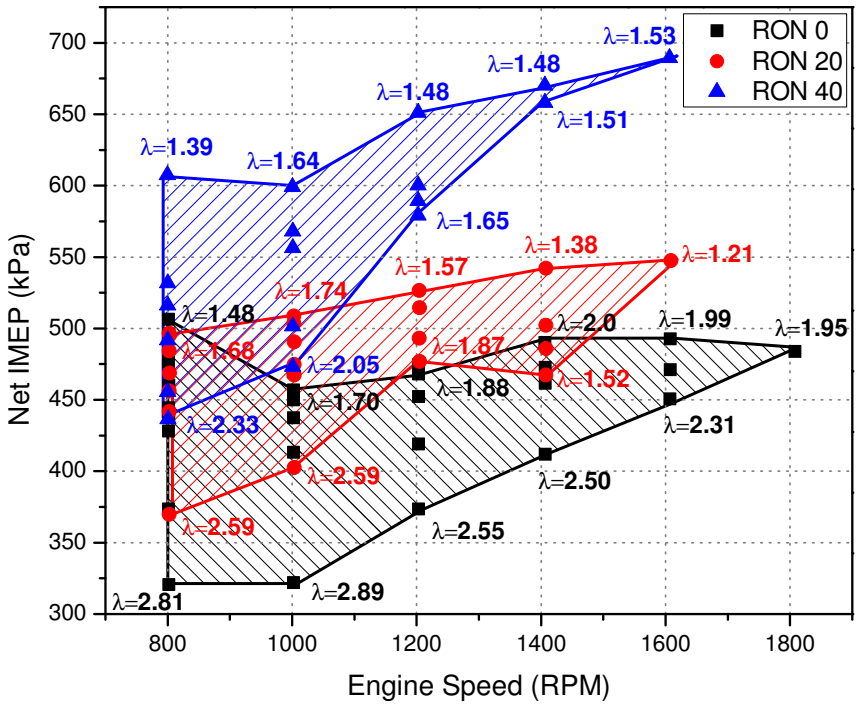

Figure 5.3: PPCI IMEP and speed range for 80 °C intake air temperature at naturally aspirated conditions

5.3 Maps for ISFC, BSFC, Indicated Thermal Efficiency and Exhaust Gas Temperature

The operating range maps are critical in evaluating the engine's performance in terms of brake and indicated specific fuel consumption (SFC), load and thermal efficiency. It gives a good indication of the regions in which the engine would run efficiently. Figure

5.4 represents the ISFC map for PPCI combustion mode at an intake temperature of 40 °C for three different fuel compositions RON 0, 20 and 40. It can be observed that the best ISFC is obtained at low loads at each engine speed. This can be attributed to the lean operation of the engine due to better fuel atomization. The fuel is injected directly into the cylinder and results in higher value of gamma thereby lowering in-cylinder combustion temperatures [46]. The heat transfer losses are significantly reduced. As compared to the ISFC map for HCCI for the same intake temperature of 40 °C, it can be observed that at 800 rpm and 1000 rpm, the engine could be run at higher loads in case of PPCI. Because of the lower compression temperature of the gases in case of PPCI, it leads to higher charge density thereby enabling higher amount of fuel to be inducted [32]. Thereby, the engine could be run at much richer mixtures within an acceptable MPRR of within 8 bar/CAD, avoiding knock.

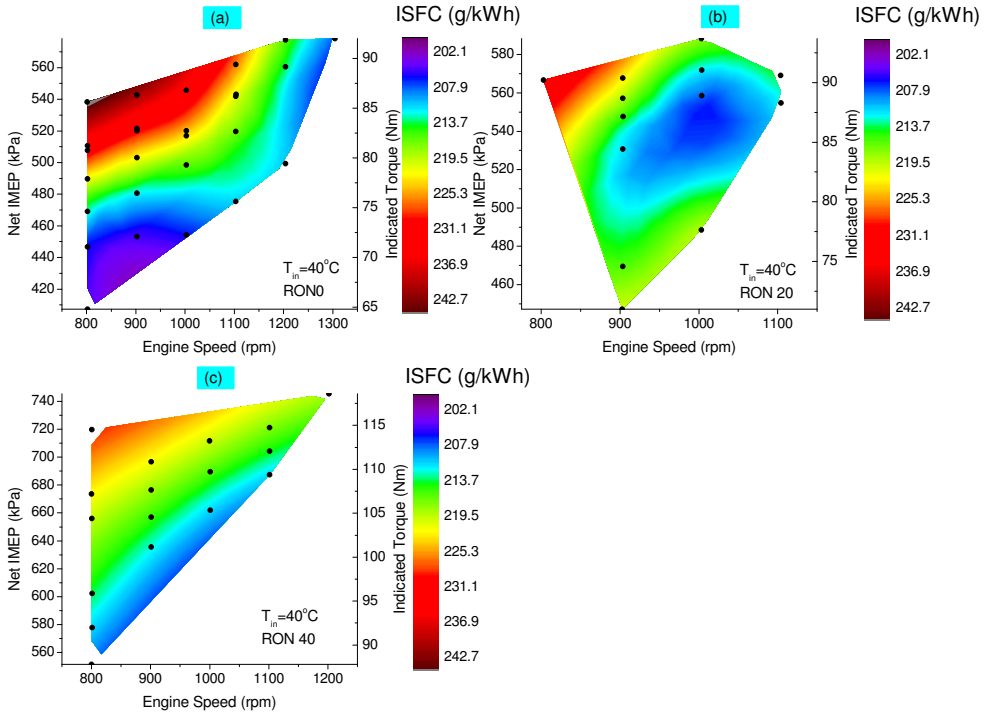

Figure 5.4: PPCI ISFC map for 40 °C intake air temperature at naturally aspirated conditions

The BSFC map for PPCI combustion regime at T_{intake} of 40 °C is shown in Figure 5.5. The sweet spot for BSFC of 250 g/kWh is obtained at a load of 72 Nm and 1000 rpm for RON 20. It can be seen that BSFC increases considerably at lower engine speeds and high loads. This is mainly due to the friction losses, which are higher at higher engine speeds. The friction losses increase with an increase in engine speed [40].

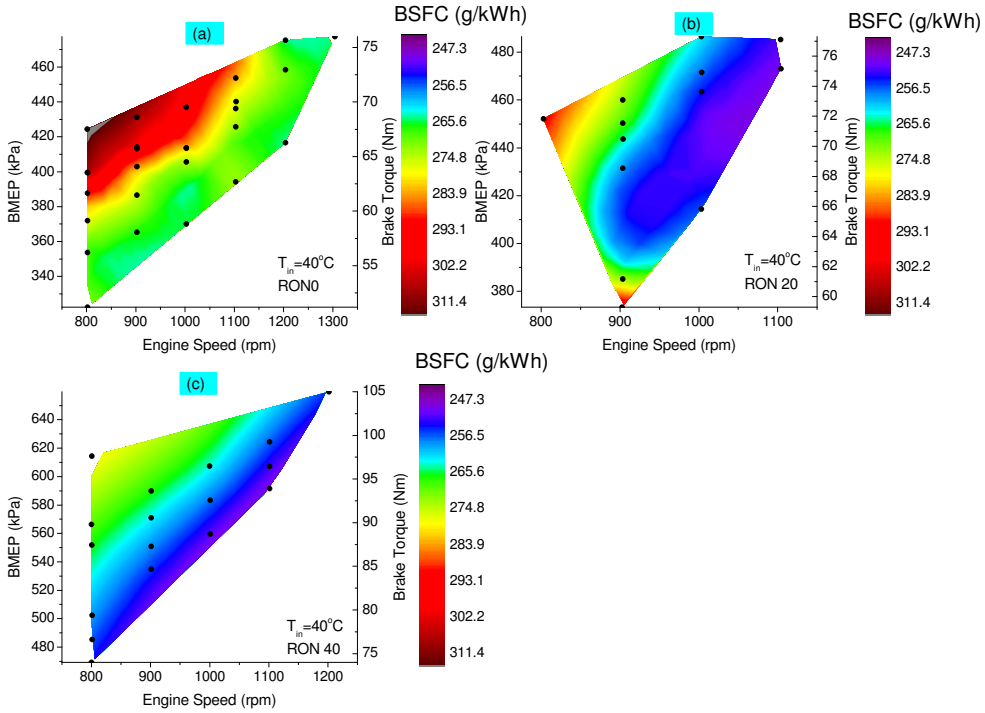

Figure 5.5: PPCI BSFC map for 40 °C intake air temperature at naturally aspirated conditions

Figure 5.6 represents the net indicated thermal efficiency maps for three RONs 0, 20 and 40 for an intake temperature of 40 °C at naturally aspirated conditions. A maximum TEF of 42% is obtained for an indicated torque of 70 Nm and 800 rpm engine speed. It can also be seen that the best thermal efficiency is attained at lower loads for all speeds. This is a typical characteristic of PPCI combustion mode, which works efficiently at low loads.

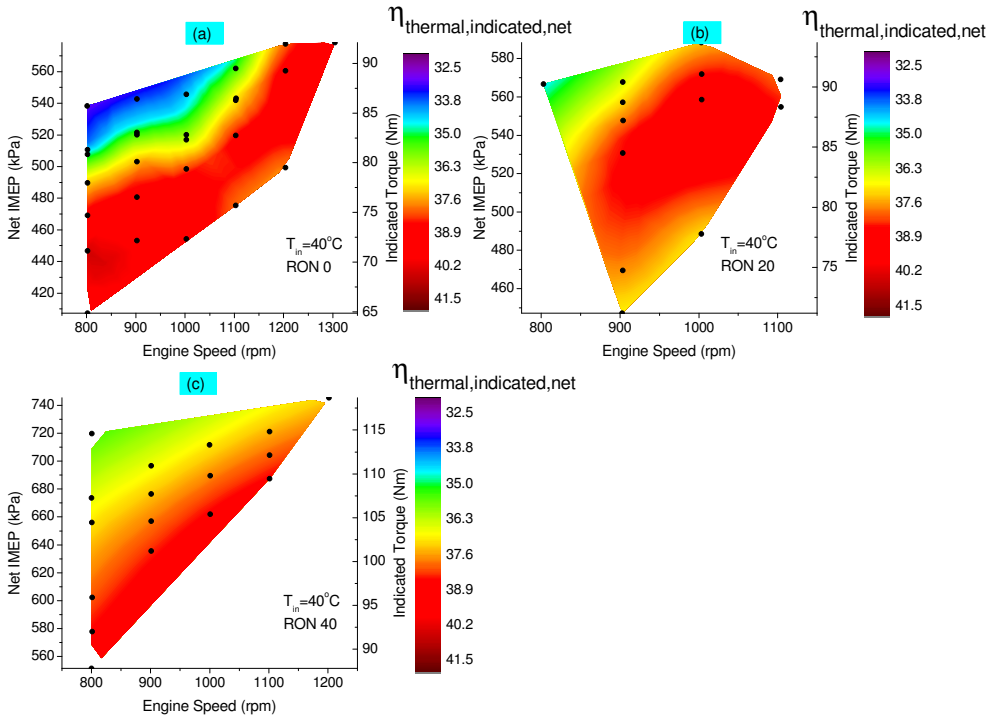

Figure 5.6: PPCI indicated thermal efficiency map for 40 °C intake air temperature at naturally aspirated conditions

Figure 5.7 shows the $T_{exhaust}$ map for PPCI combustion regime at T_{intake} of 40 °C. It can be seen that the exhaust temperatures have been maintained over 300 °C for even the lowest loads and speeds. This implies that the oxidation catalyst would function with a good conversion efficiency in order to break down the HC and CO molecules, since the catalyst light-off temperature is about 250 °C and the exhaust temperatures are way above it over the entire range of speeds and loads.

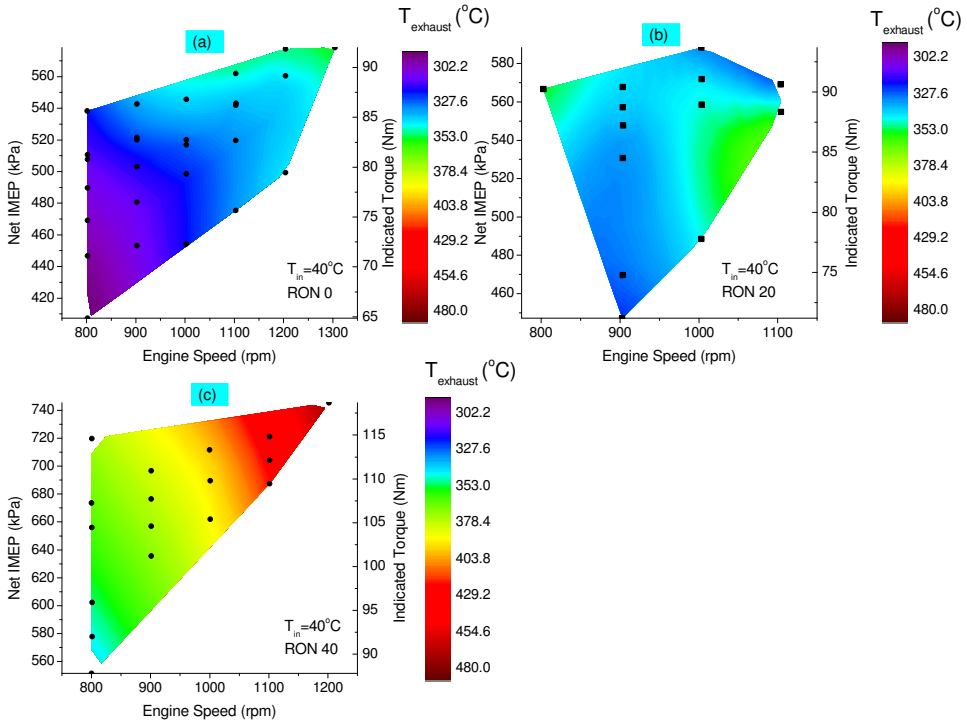

Figure 5.7: PPCI exhaust gas temperature map for 40 °C intake air temperature at naturally aspirated conditions

5.4 Optimized PPCI maps

Experiments were performed for PPCI combustion mode at 650 different combinations of operating conditions such as T_{intake}, P_{intake}, RON, equivalence ratio and engine speed. In order to generate the optimized map for PPCI combustion mode, the points with the best ISFC were chosen at every engine speed- load condition. The

data points chosen are given in Appendix A.1. The best ISFC obtained was 200 g/kWh at low engine loads. It has also been observed that up to 1400 rpm, the ISFC increases with an increase in engine load. The charge gets richer with an increase in load at these data points. However, at speeds higher than 1400 rpm, the ISFC values vary by a small amount at all loads. This is mainly because the equivalence ratio range is very narrow for higher engine speeds.

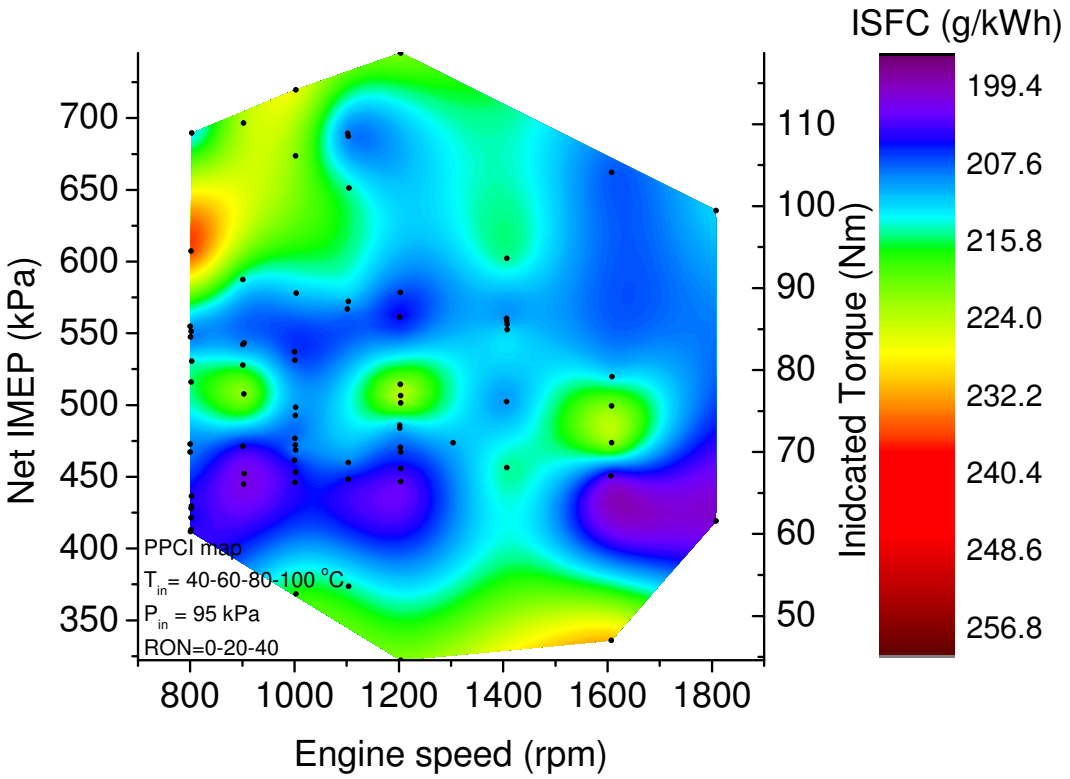

Figure 5.8: PPCI ISFC optimized map for all intake air temperatures and RONs at naturally aspirated conditions

Figure 5.9 illustrates the optimized BSFC map for three different fuel compositions

RON 0, 20 and 40. Lowest BSFC of 250 g/kWh is obtained at high loads and speeds. The friction losses are high at higher engine speeds and thereby have a significant effect on the BSFC values. The BSFC values are the highest at 1600 rpm and low loads. This shows that it is not suitable to run the engine in PPCI mode at higher engine speeds and low loads.

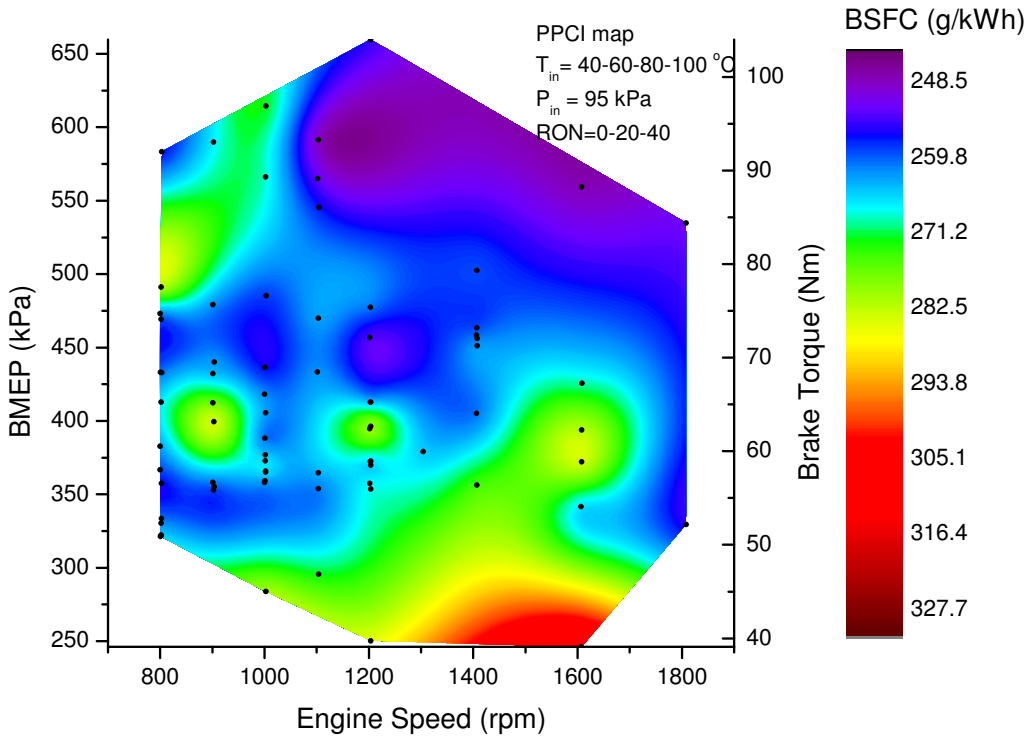

Figure 5.9: PPCI BSFC optimized map for all intake air temperatures and RONs at naturally aspirated

The indicated thermal efficiency maps are shown in Figure 5.10. The range of thermal efficiencies was 32- 42 % over a load range of 45- 120 Nm. The best thermal efficiency

points were obtained at an engine load of 450 kPa IMEP for all speeds. Since the map was an optimized set of data points obtained from a combination of various parameters, the engine would run quite efficiently at most of the data points with the combinations used for the map. However, it can be seen that the thermal efficiency reduces to 35% at low speeds and higher loads, limiting the high load operation at low speeds for PPCI combustion mode.

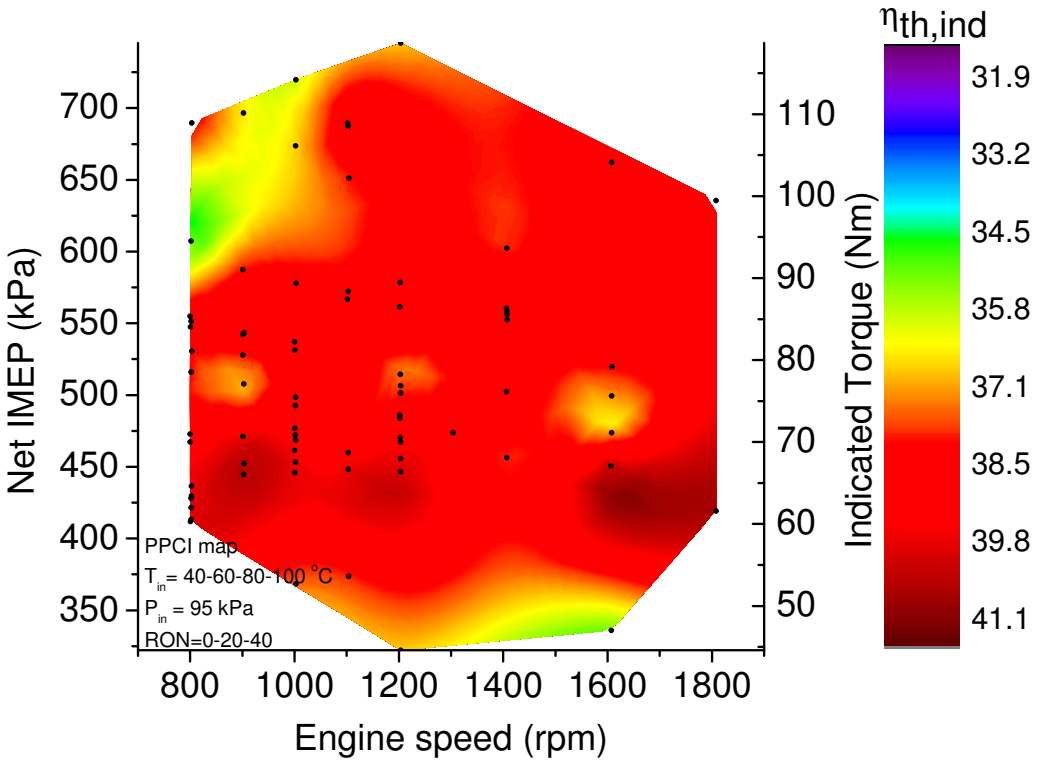

Figure 5.10: PPCI indicated thermal efficiency optimized map for all intake air temperatures and RONs at naturally aspirated conditions

The optimized exhaust temperature map for PPCI combustion regime under naturally aspirated conditions is shown in Figure 5.11. It can be observed that $T_{exhaust}$ for almost all the data points lie above the catalyst light off temperature of 250 °C. Moreover, the range of $T_{exhaust}$ lies in an acceptable region of 290-490 °C. The range is a trade off between HCCI and RCCI combustion regime, in terms of exhaust temperature and HC emissions based on the findings in this thesis.

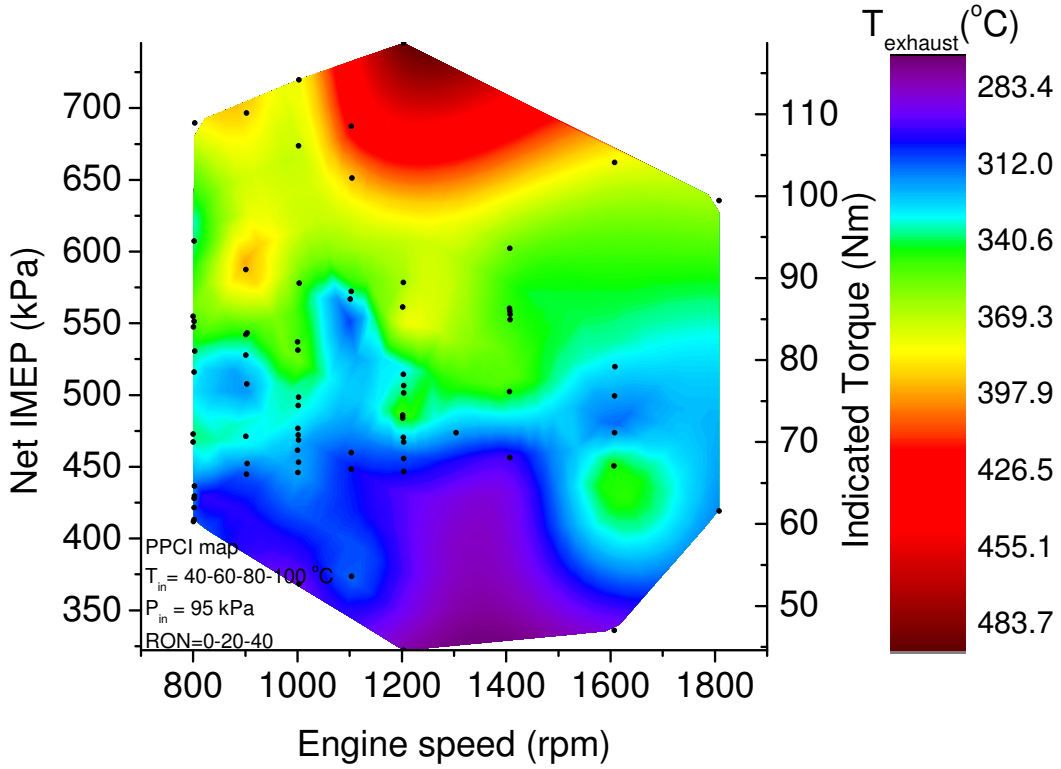

Figure 5.11: PPCI exhaust temperature optimized map for all intake air temperatures and RONs at naturally aspirated conditions

5.5 Effect of Intake Air Temperature on PPCI Combustion

Adjusting intake air temperature is one of the most common methods to control PPCI combustion [56]. For this reason, four different intake air temperatures are tested during experiment at a constant lambda and engine speed with RON20 fuel. Table 5.4 shows the test details for effects of increased intake air temperature.

Table 5.4
Operating conditions used for the experiments to study the effect of intake air temperature on PPCI combustion

Test Parameters	Value/ Unit
Engine Speed	1000 (rpm)
Injection Pressure	100 (bar)
Injection Starting Angle	100 (deg bTDC)
Fuel Type	RON 20
IVO	25.5 (deg bTDC)
EVC	22 (deg bTDC)
Throttle Body Position	100 (%)
Intake Air Temperature	40, 60, 80, 100 (°C)
Lambda	2.0
Intake Pressure	95 (kPa)

The effects of increasing intake air temperature on in-cylinder pressure are shown in Figure 5.12. The maximum cylinder pressure increases with the increase of the intake air temperature. At the same time, the location of maximum cylinder pressure

gradually approaches the TDC with an increase in intake air temperature. In addition, the maximum cylinder pressure occurred before TDC when the intake air temperature reached at 100 °C, as shown in Figure 5.12. Heating the air taken into the cylinder increases the reaction rate by providing faster movement of molecules. The start of combustion is advanced with increase of intake air temperature. During experiments, the knock was observed at high intake temperatures over 100 °C and misfire was observed at low intake temperatures below 40 °C.

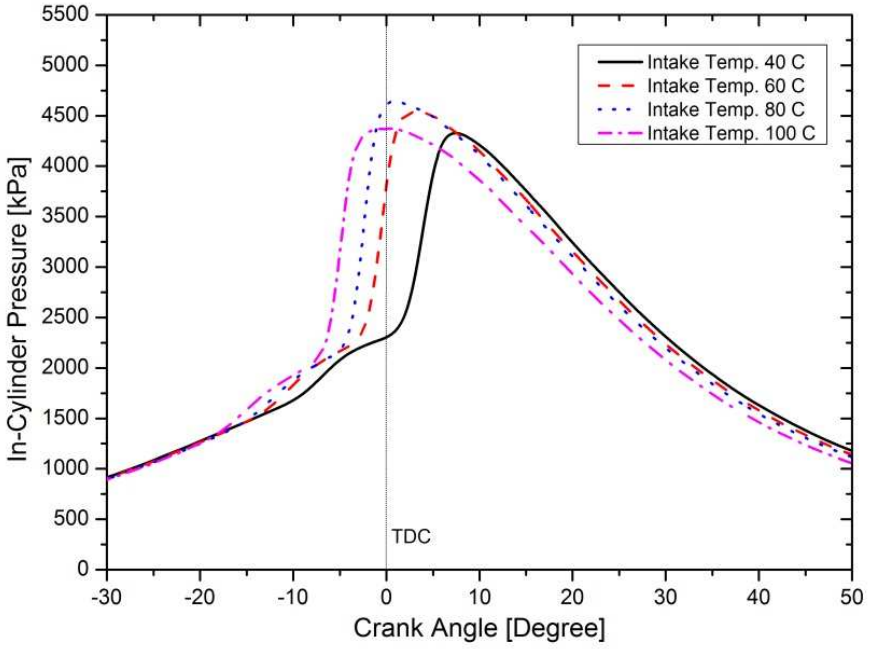

Figure 5.12: Effect of intake air temperature on PPCI in-cylinder pressure at a lambda of 2

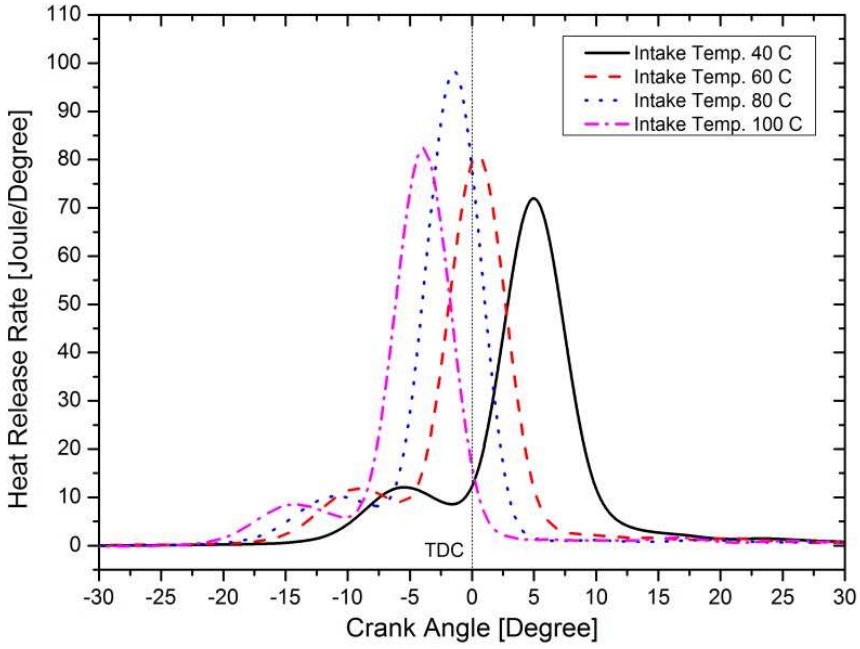

Figure 5.13: Effect of intake air temperature on the PPCI heat release rate at a lambda of 2

Figure 5.14 shows the effect of intake air temperature on IMEP and BMEP. It can be observed that the IMEP and BMEP reduce with an increase in T_{intake} . While maintaining a constant equivalence ratio, with an increase in intake temperature the air density decreases. The temperature of compression increases, thereby auto igniting the charge much earlier. With the combustion phasing being shifted away from the optimum value of 5-10 CAD aTDC, a drop in IMEP and BMEP is observed.

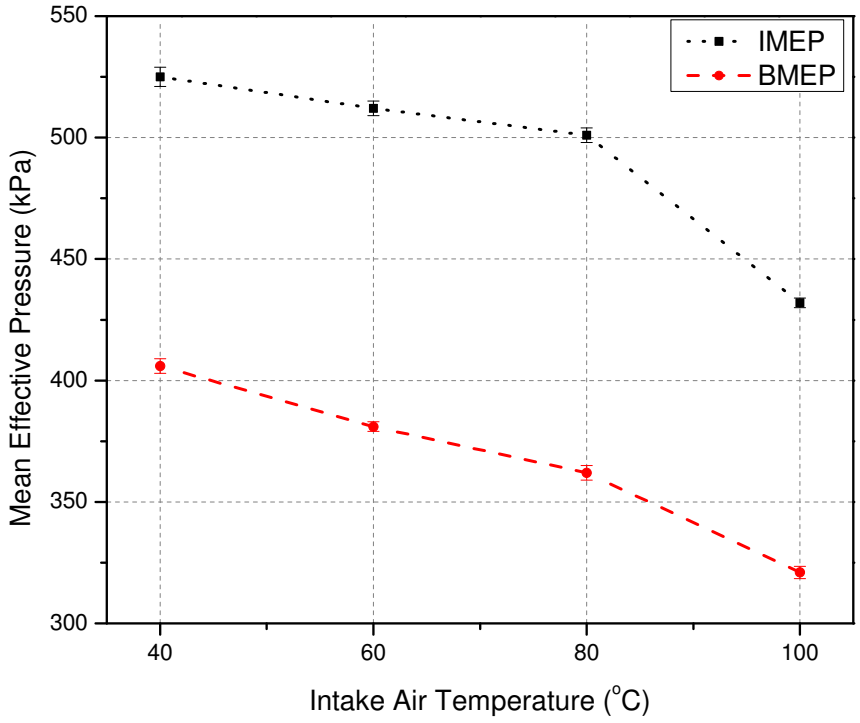

Figure 5.14: Effect of Intake temperature on IMEP and BMEP at a lambda of 2

The indicated thermal efficiency as a function of intake temperature is depicted in Figure 5.15. With an increase in intake air temperature, the thermal efficiency drops significantly. Due to the increase in compression and combustion temperature, the heat transfer losses increase. Moreover, the combustion efficiency is about 87% in case of 100 °C intake temperature. Due to the increase in fuel energy content and a drop in combustion efficiency, the thermal efficiency drops at higher intake temperatures.

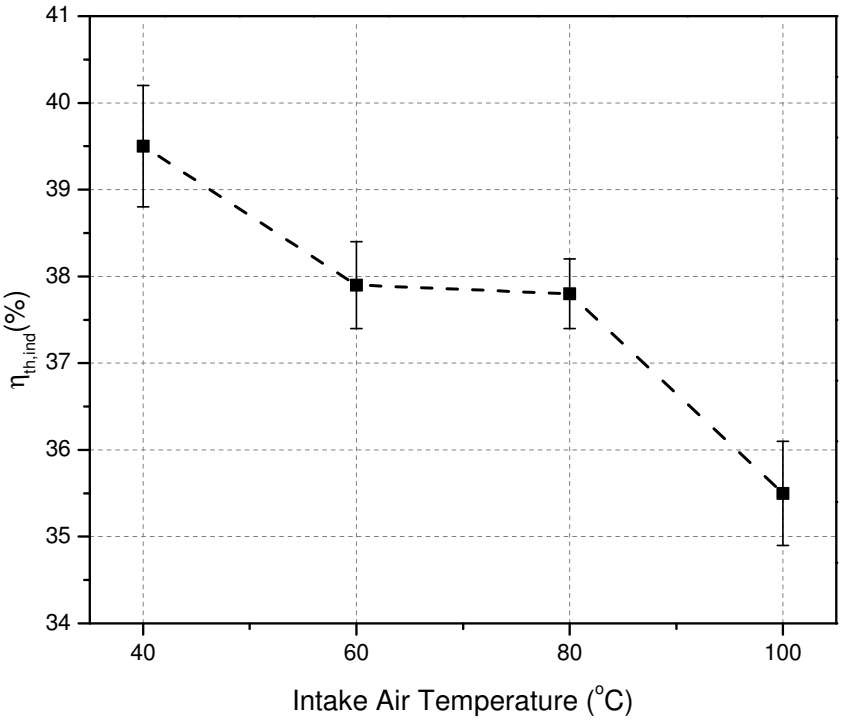

Figure 5.15: Effect of intake temperature on indicated thermal efficiency at a lambda of 2

The combustion characteristics at different intake temperatures are shown in Figure 5.16. It can be observed that the CA10, CA50 and CA90 get advanced with an increase in temperature. The start of injection for all the temperatures were held constant at 100 CAD bTDC. With an increase in intake air temperature, the start of combustion gets advanced. This is due to the increase in the IVC temperature of the air-fuel mixture. Thereby, auto ignition of the mixture occurs much earlier, thereby

advancing the combustion phasing. An interesting point to note is that the best indicated thermal efficiency of 39.5 % was obtained when the combustion phasing was about 5 CAD aTDC. This supports the study in literature [40] that the optimal combustion phasing for the best thermal efficiency should be between 5-10 CAD aTDC. Since the SOI was held constant, the CA50 for the other temperatures got advanced. However, if the SOI was retarded with an increase in intake air temperature, the combustion phasing could be controlled to be in the range of 5-10 CAD aTDC.

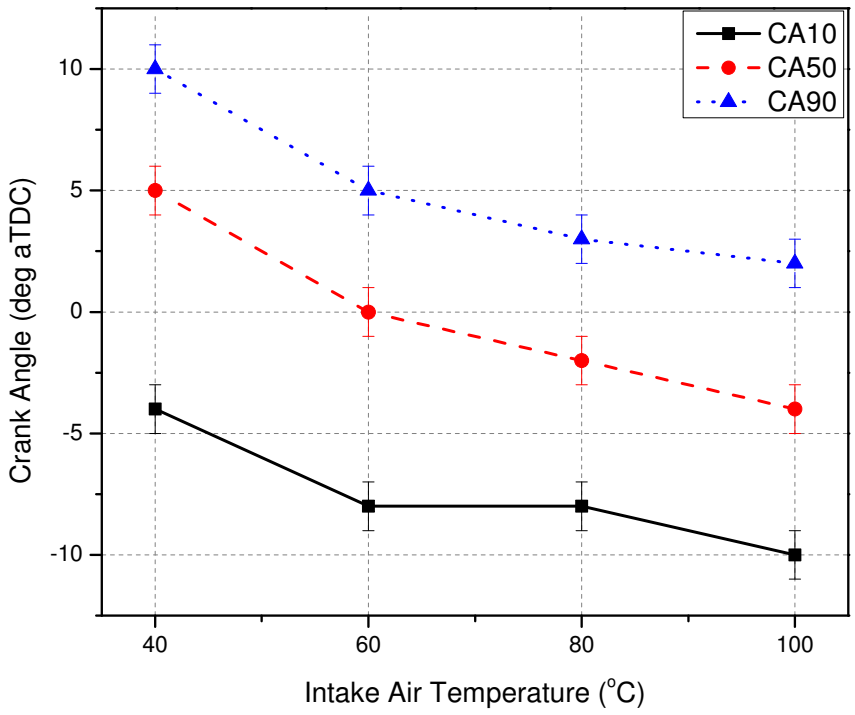

Figure 5.16: Effect of intake temperature on combustion phasing at a lambda of 2

5.6 Effects of Boost pressure on PPCI combustion

An analysis of the experimental results was conducted to understand the effect of intake manifold pressure on PPCI combustion. All experiments were performed at seven different intake pressures from 1.0 bar to 1.6 bar with 0.1 bar intervals at different loads using n-heptane as the fuel. All tests were conducted at constant engine speed, intake temperature, injection timing and injection pressure conditions as given in Table 5.5.

Table 5.5
Operating conditions used for the experiments to study the effect of intake pressure on PPCI combustion

Test Parameters	Value/ Unit
Engine Speed	1000 (rpm)
Injection Pressure	100 (bar)
Injection Starting Angle	100 (deg bTDC)
Fuel Type	RON 0
IVO	25.5 (deg bTDC)
EVC	22 (deg bTDC)
Throttle Body Position	100 (%)
Intake Air Temperature	60 (°C)
Lambda	1.8-6.0
Intake Pressure	100:10:160 (kPa)

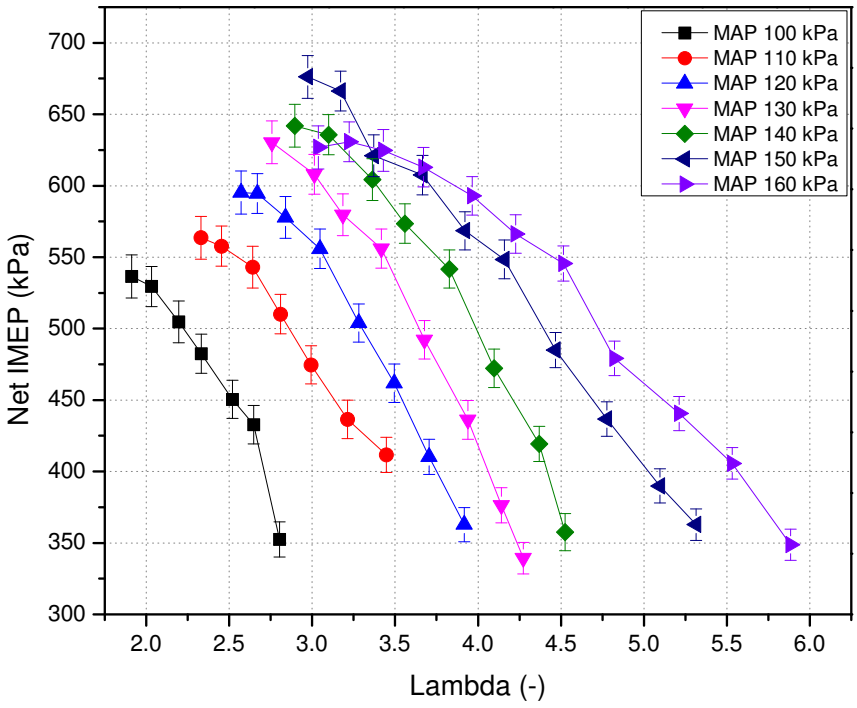

Figure 5.17: Effect of boost pressure on IMEP in the PPCI regime

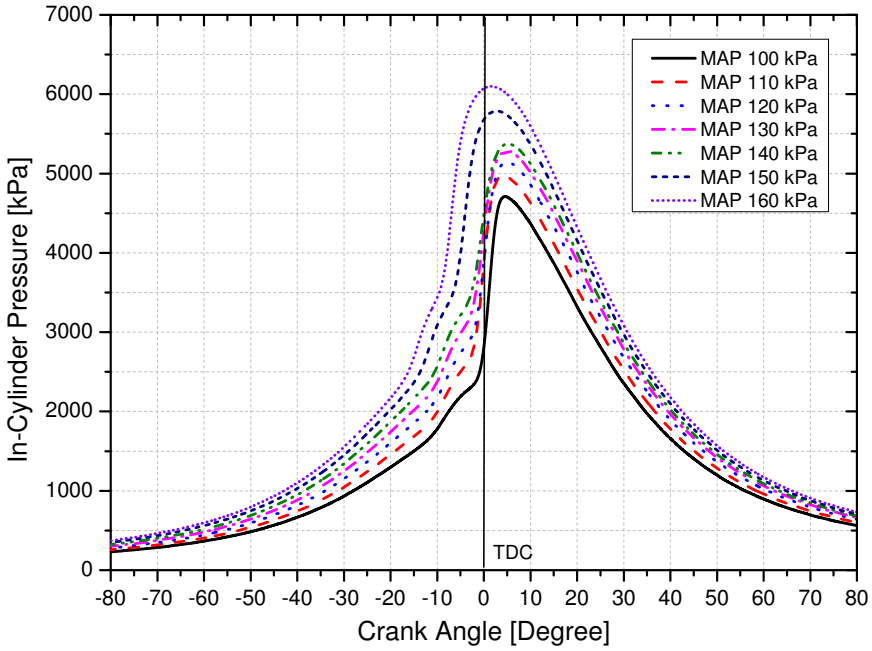

Figure 5.18: Variation of cylinder pressure versus crank angle at different intake manifold pressures at constant fuel energy 749 J in the PPCI regime

Figure 5.17 shows the effects of intake manifold pressure on IMEP. IMEP decreased with an increase in lambda. This is due to a decrease in input fuel energy quantity when moving towards lean air-fuel mixture (i.e., high lambda values). Figure 5.17 shows that PPCI combustion can be achieved at a larger range of lambda values with an increase in the intake manifold pressure. For a fixed lambda condition, as intake pressure increased, IMEP increased due to delivery of more air and fuel energy to the cylinder. But for a fixed intake pressure condition, IMEP has a decreasing trend with increase in lambda values.

Figure 5.18 and 5.19 show the variations of cylinder pressure and heat release rate versus crank angle at different intake manifold pressures for a constant input fuel energy. In-cylinder pressure increased with the increase in intake manifold pressure. The compression pressure and temperature also increase at the end of compression stroke with an increase in intake manifold pressure. Higher in-cylinder pressure is obtained with the increase in intake manifold pressure as intake valve closing (IVC) pressure and IVC temperature will increase. This significantly affects PPCI combustion which is highly dependent on the temperature-pressure history during the compression stroke.

Maximum cylinder pressure was obtained near the TDC at higher intake manifold pressures especially at 150 and 160 kPa. Figure 5.19 shows the two stages of heat release in which increased intake manifold pressure resulted in earlier low temperature reactions. Also, main combustion was advanced with the increase of intake manifold pressure.

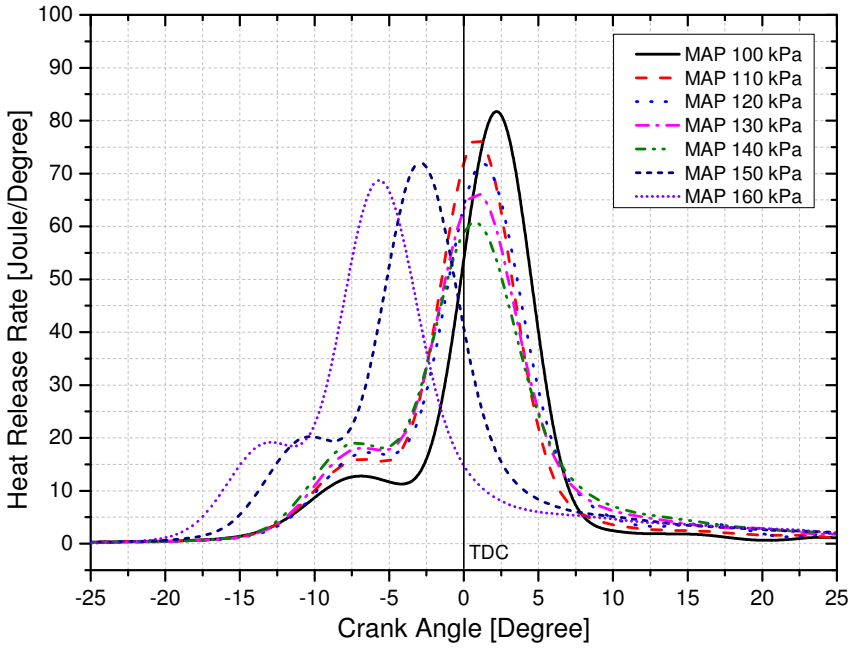

Figure 5.19: Variation of heat release rate versus crank angle at different intake manifold pressures at constant fuel energy 749 J in the PPCI combustion regime

Figure 5.20 shows the variation of indicated thermal efficiency as a function of lambda and intake manifold pressure. Indicated thermal efficiency increased until a certain lambda value and then started to decrease for all intake manifold pressures. Maximum thermal efficiency of 40% was observed at an intake manifold pressure of 100 kPa and lambda 2.6, which is comparable to that of conventional diesel engines. As the intake manifold pressure increased, a small decrease in the indicated thermal efficiency was observed owing to leaner mixtures.

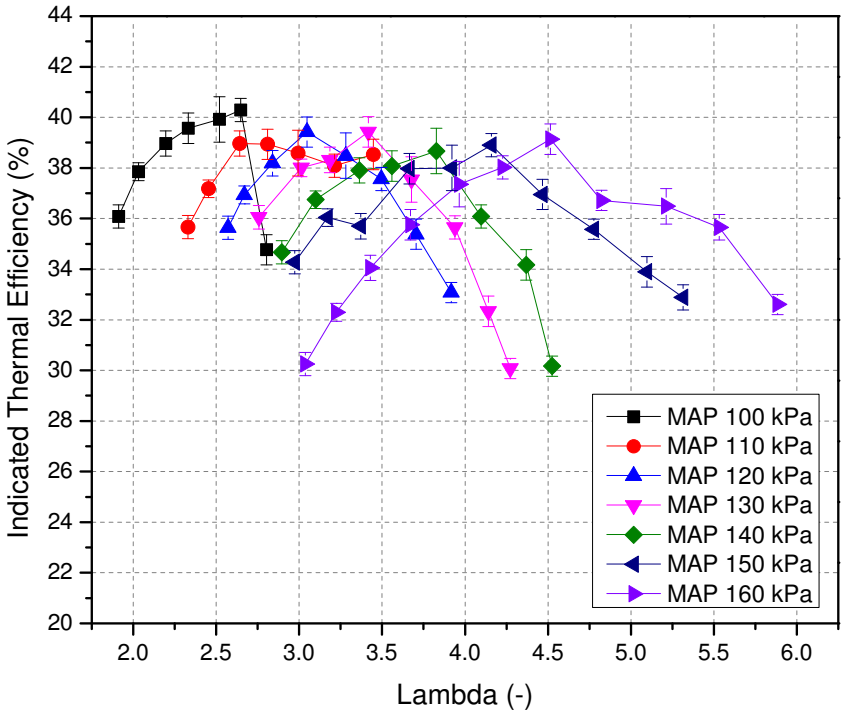

Figure 5.20: Variation of indicated thermal efficiency with lambda at different intake manifold pressures in PPCI combustion regime

Figure 5.21 depicts the effects of intake manifold pressure on CA50. It is apparent that combustion is advanced with an increase in intake manifold pressure. Therefore, CA50 is observed bTDC because of early auto-ignition at higher intake manifold pressures. Thermal efficiency is strongly affected by CA50. CA50 should be kept slightly after the TDC to obtain higher engine efficiency [40] [66]. An increase in thermal efficiency is observed when CA50 is slightly after TDC in Figure 5.21. CA50 was retarded after TDC at lower intake manifold pressure due to an increase of lambda. However,

indicated thermal efficiency decreased because of very lean mixture at lambda value of 2.8 and intake manifold pressure of 100 kPa. At this point, the operating region is close to the misfiring zone with weak auto-ignition capability at very lean mixtures, leading to low indicated thermal efficiency. At 160 kPa, both the start of combustion (SOC) and CA50 were advanced especially with richer mixtures. Too early ignitions bTDC result in low indicated thermal efficiency.

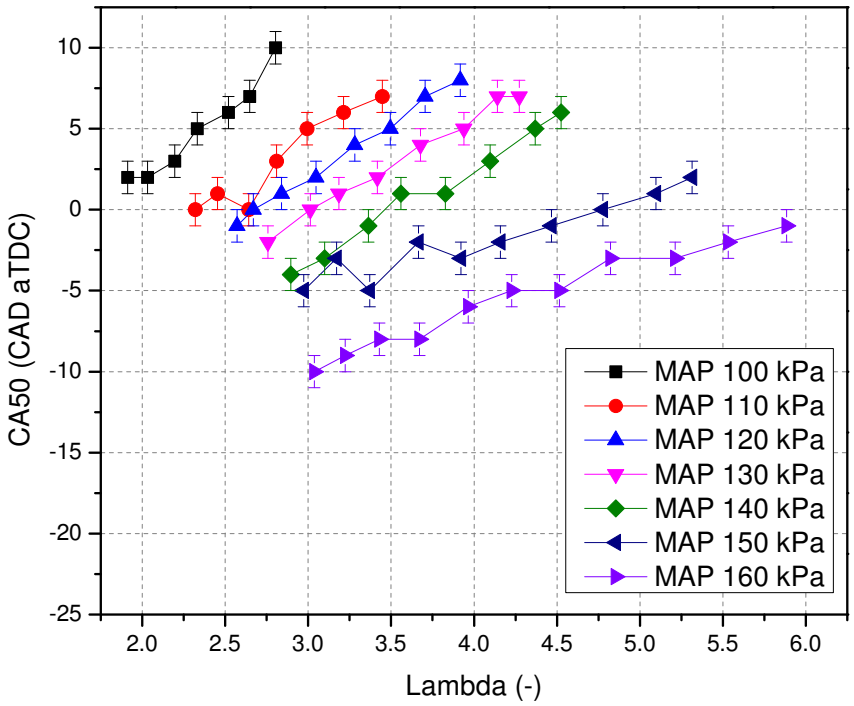

Figure 5.21: Effect of intake manifold pressure on CA50 at different lambda values in PPCI combustion regime

5.7 Effect of SOI on PPCI combustion

PPCI combustion is strongly dependent on temperature of charge mixture and composition during the compression stroke. Injection timing is used commonly in order to control PPCI combustion, because injection timing alters the homogeneity of the charge mixture, start of combustion and combustion process. So, the effects of injection timing on PPCI combustion must be investigated in detail. The operating conditions for studying this effect is given in Table 5.6.

Table 5.6
Operating conditions used for the experiments to study the effect of SOI on PPCI combustion

Test Parameters	Value/ Unit
Engine Speed	1000 (rpm)
Injection Pressure	100 (bar)
SOI	270, 180, 90, 60, 30, 20 (deg bTDC)
Fuel Type	RON 0
IVO	25.5 (deg bTDC)
EVC	22 (deg bTDC)
Throttle Body Position	100 (%)
Intake Air Temperature	80 (°C)
Lambda	1.8
Boost Pressure	95 (kPa)

Figure 5.22 shows the variations of in-cylinder pressure at different SOI versus crank angle. Maximum in-cylinder pressure was obtained as 4733 kPa at 2 CAD bTDC when the fuel was injected at 270 CAD bTDC whereas it was obtained 3368 kPa at

20 CAD bTDC when the fuel was injected 20 CAD bTDC. It was seen that maximum in-cylinder pressure increased and it was obtained earlier in case of early injection timing. Early fuel injection causes to obtain more homogeneous charge mixture. So, fuel molecules can meet with oxygen molecules more easily. In addition, the residence time for the fuel to vaporize increased and obtain stable combustion conditions as a result of early injection [40, 67]. Thus, fuel can be ignited earlier according to crank angle and maximum in-cylinder pressure was obtained earlier. In case of advancing SOI, the increase of maximum in-cylinder pressure can be explained by the fact that all fuel energy is released at a small interval of crank angle with more homogeneous charge mixture. SOC is retarded and large part of combustion occurred in expansion stroke when the fuel is injected towards to the TDC. This situation causes a decrease in the maximum in-cylinder pressure.

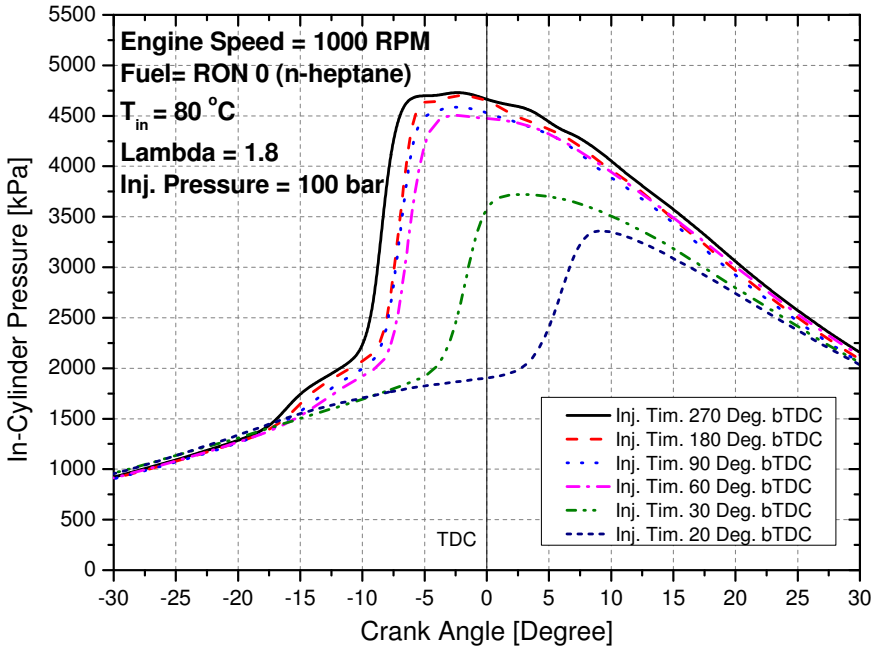

Figure 5.22: Effects of SOI on in-cylinder pressure in PPCI combustion regime

Figure 5.23 shows the heat release rates variation by injection timing. As seen in the figure there are two peak points in HRR for cases with SOI 180 and 270 CAD bTDC. The first peak indicates the insufficient in-cylinder temperature to vaporize of the fuel at the beginning of the injection. Retarded injection provides a higher in-cylinder temperature because of the single stage heat release. Advanced SOI caused early ignition as shown in Figure 5.23. Therefore the maximum heat release rate locations were shifted towards TDC except for SOI of 20 CAD bTDC. This may cause a reduction in thermal efficiency. Optimal CA50 is very critical in determining

the best thermal efficiency of the engine at a given operating condition. Theoretically, an ideal CA50 lies close to TDC [68]. However, when CA50 is located around 8-10 ° aTDC in a conventional CI or SI engine [40], net IMEP and thermal efficiency is the maximum. It is seen that the CA50s were obtained bTDC with advanced injection timings. This will reduce the thermal efficiency of the engine. CA50 was close to TDC when the SOI was 30 CAD bTDC. N-heptane is a high reactivity fuel and therefore it should not be injected early as it leads to too early combustion.

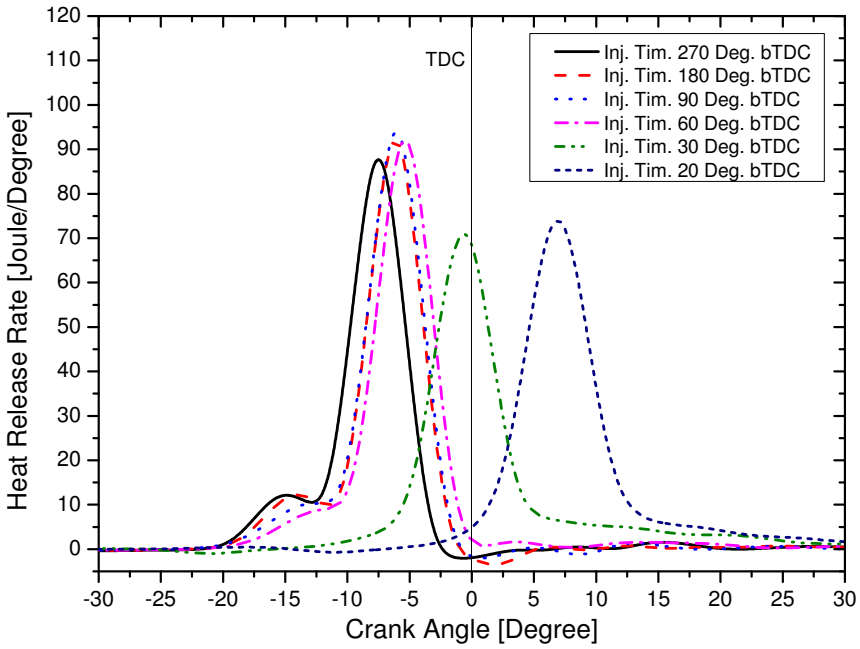

Figure 5.23: Effects of SOI on heat release rate in PPCI combustion regime

Figure 5.24 gives the CA10, CA50 and CA90 as a function of SOI. As seen in Figure

5.24, there is no remarkable effect on CA10, CA50 and CA90 when SOI was fixed at interval of 270 and 90 CAD bTDC. But, CA10, CA50 and CA90 were obtained later if the injection timing was fixed under 90 CAD bTDC. Combustion phasing was retarded towards TDC. So, CA10, CA50 and CA90 values were much retarded as calculated from the cumulative heat release rate.

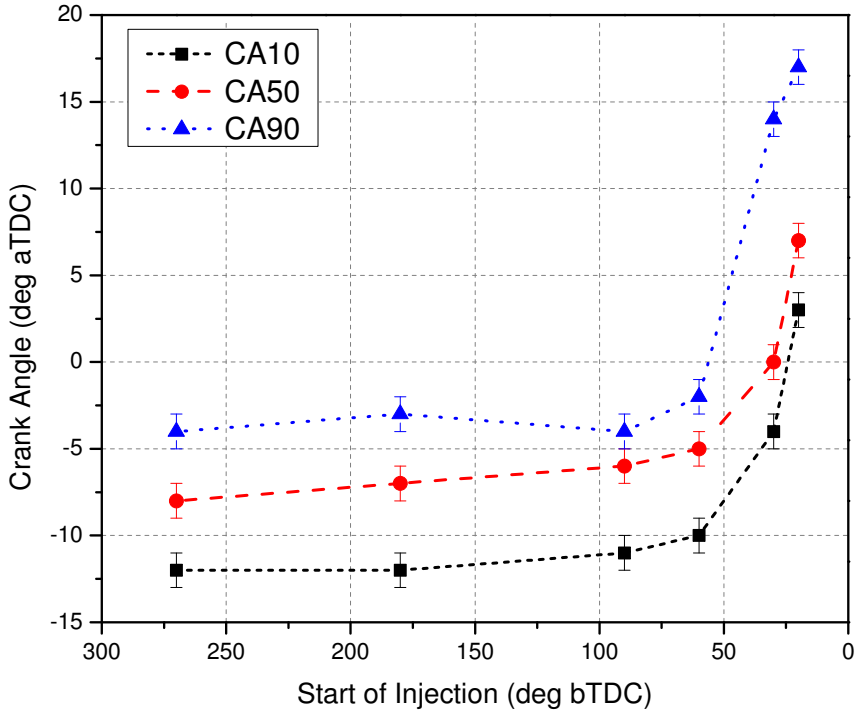

Figure 5.24: Effects of SOI on CA10, CA50 and CA90 in PPCI combustion regime

Chapter 6

Summary and Conclusions

Experimental investigation has been carried out to determine the operating regions and performance maps for three different low temperature combustion regimes: HCCI, PPCI and RCCI. Different methods of operating range extension for load limit and lean limit have been studied. A parametric study has been conducted to study the effect of several operating conditions on the combustion and performance characteristics of the LTC modes. Major results and contributions from this thesis have been summarized and conclusions have been outlined.

6.1 Conclusions

The results and the summary of the findings form this research have been described in the following sections:

6.1.1 Operating range and performance maps

- HCCI operation for naturally aspirated conditions in this study has a speed range of 800- 1600 rpm and load range of 250 kPa to 580 kPa IMEP for RON 0, 20 and 40. For boosted conditions the speed limit could be extended to 2000 rpm and the load limits were between 440 kPa to 800 kPa. The higher in-cylinder pressures and higher intake temperature with the assist of boost pressure enables extending the load limit and the speed limit for HCCI mode operation. Moreover, the control of combustion phasing was challenging for higher RON at lower T_{intake}. While very high loads result in pressure oscillations due to the rapid heat release rate, low loads result in unstable combustion due to the lower in-cylinder temperatures and dilution effect of the trapped exhaust gases. These two factors limit the HCCI operating range between the lean limit and the high load limit.

- The most efficient operating region for HCCI is found to be in the range of

50-100 Nm brake torque. ISFC improved with engine load. The lowest ISFC of 205 g/kWh was obtained for RON 40 and the best BSFC of 210 g/kWh was obtained for RON 0. Fuels with higher reactivity tend to allow leaner HCCI operation. Moreover, a decrease in volumetric efficiency at increased T_{intake} and higher boost pressures results in higher pumping losses thereby leading to higher BSFC values. Combustion phasing plays a crucial role in determining the optimal thermal efficiency at a given engine load and speed. The best thermal efficiencies were obtained at an optimal combustion phasing of 5-8 deg aTDC. A maximum indicated thermal efficiency of 40% was attained at mid load conditions for all three RONs. The exhaust gas temperatures are in the range of 230 to 410 °C which is close to typical catalyst light off temperatures. Thereby, the operating region for HCCI combustion regime falls in the acceptable range.

- The speed range for the RCCI mode operation gets narrower with an increase in PR. This is mainly due to the reduced reactivity of fuel at higher PR as a result of which the combustion becomes unstable at speeds higher than 1400 rpm for PR 60. Moreover, the lean limit for lower PR is much higher due to the combustion stability provided by the high reactive fuel dominance. At higher boost pressures, due to the increased charge temperature at IVC, the lean limit for all PRs could be further expanded. The engine load for the operating region is in the range of 300 to 1300 kPa IMEP and speed range lies in the range of 800- 3200 rpm, which is considerably higher as compared to HCCI combustion

regime.

- The best ISFC shifts towards higher load conditions at 1400 rpm with an increase in the PR of the fuel. The best ISFC of 184 g/kWh was obtained for PR 40 at 1800 rpm. At low loads and speeds, the lower combustion efficiencies lead to an increase in the ISFC. The range of BSFC obtained was 230- 325 g/kWh with th best BSFC occurring at high speeds and loads for all PRs. The compression ratio of the engine, pumping losses and specific heat ratio play a crucial role in determining the optimal thermal efficiency. Maximum indicated thermal efficiency of 45% was obtained at 1800 rpm and 120 Nm indicated torque for PR 40. Exhaust gas temperatures were in the range of 200 °C to 725 °C. The exhaust gas temperatures are well below the catalyst light off temperatures at low loads. This region is not favorable due to the inability of the oxidation catalysts to function at these temperatures. However, about 90% of the data points lie in the favorable operating region with respect to the operating temperature of oxidation catalysts.

- For PPCI combustion mode, the engine could be run much leaner at higher intake temperatures, pushing the load limit towards much leaner operating conditions. The range of engine speeds is much larger for lower octane fuels RON 0 as compared to RON 40. RON 0 is more suitable to run the engine at low load conditions, whereas RON 40 is ideal for low-mid load conditions. The load range for operation was in the range of 320- 750 kPa IMEP, while the speed

range was 800- 1800 rpm.

- The best ISFC was obtained at low loads for each engine speed. The best ISFC of 202 g/kWh was attained at 800 rpm and 65 Nm indicated torque for RON 0. The sweet spot for BSFC (250 g/kWh) was obtained at a load of 72 Nm and 1000 rpm for RON 20. A maximum thermal efficiency of 42% is obtained at the point of the best ISFC. As a typical characteristic of PPCI combustion, the best efficiencies were obtained at low loads. The exhaust temperatures remained over 300 °C even at the lowest loads and speeds. This implies that the oxidation catalyst would function flawlessly over the entire operating region.

- As a baseline comparison with the SI map, it can be observed that RCCI combustion under naturally aspirated conditions had a much better ISFC at mid loads in the range of 600-800 kPa IMEP and engine speed in the range of 1200-2000 rpm. Moreover, PPCI had a 5% improvement in ISFC at 600 kPa engine load and 1400 rpm of engine speed. for low loads, HCCI combustion regime had an improvement of about 9% in ISFC values in the load range of 400-600 kPa and engine speed of 800-1600 rpm.

- Cost vs Efficiency Gain The Bosch 62251 port fuel injector costs about $95 each. In order to install four port fuel injectors on the manifold, with the actuation linked to the control unit, the total cost to install the port fuel injection system could be roughly estimated to be $800. As seen in this study, RCCI combustion regime can offer upto 14% improvement in fuel economy and upto

8% improvement in net indicated thermal efficiency over SI mode. Therefore, it is recommended that an SI-RCCI mode switch could be performed with one direct injection rail and one port fuel injection rail. With the cost incurred for the instrumentation of the PFI rail, a significant improvement in overall engine efficiency can be achieved.

6.1.2 Parametric Study on Combustion and Performance characteristics

- For HCCI combustion, the combustion phasing gets advanced with lower RON of the fuel. The higher reactivity of the fuel advances the start of combustion. At higher T_{intake} and engine loads, the control of combustion pahsing becomes more challenging. The best thermal efficiency is attained at a combustion phasing of 8-10 CAD aTDC. With an increase in T_{intake}, higher in-cylinder pressure and combustion temperatures result in knocking. However, higher T_{intake} improves the auto ignition conditions in the combustion chamber. The SOC is advanced due to the higher compression temperatures. Higher boost pressure tends to decrease the thermal efficiency and the combustion efficiency. This is due to the fact that the CA50 is too advanced at these boost pressures.

- For RCCI combustion, there appears to be a two stage HTHR. The first stage

heat release is mainly triggerred due to n-heptane being injected late into the cylinder. The first stage heat release triggers the remainder mixture to burn and thereby resulting in the second stage HTR. This two stage HTHR occurs due to the SOI for n-heptane being too retarded. The indicated thermal efficiency increased with an increase in PR. This is because of the reduced in-cylinder temperatures and pressures due to the two stage HTHR for PR 60. Moreover, the combustion efficiency improves with PR because of the higher completeness of combustion with the two stage HTHR for the conditions studied. With an increase in T_{intake}, the SOC tends to get advanced due to the higher charge temperatures. However, the CA50 does not get advanced drastically and remains around 8-10 CAD aTDC. With an increase in boost pressure, the CA10 gets advanced significantly. But the thermal efficiency and net IMEP do not change much since the combustion phasing lies in the range of 8-12 CAD aTDC.

- For PPCI combustion, the IMEP and BMEP tend to reduce with an increase in T_{intake} since the temperature of compression increases and thereby reducing the amount of fuel being injected. The CA10, CA50 and CA90 tend to get advanced with an increase in T_{intake}. Due to the increased manifold temperature of air-fuel mixture, auto ignition occurs much earlier and thereby advancing the combustion phasing. Thermal efficiencies are strongly affected by combustion phasing. The best thermal efficiencies are obtained when the combustion phasing are in the range of 5-10 CAD aTDC. PPCI combustion could be achieved

at a larger range of lambda values with an increase in boost pressure. The two stage heat release (LTR and HTR) result in reduced in-cylinder temperatures, thereby resulting in earlier low temperature reactions with increase in boost pressure. Therefore, the combustion phasing was advanced with increase in boost pressure. Maximum thermal efficiency of 40% was observed at 100 kPa boost pressure and lambda of 2.6, which is comparable to that of conventional diesel engines. Advancing the SOI results in more homogeneous mixture and provides sufficient time for the fuel to vaporize. Thereby the fuel is ignited early and maximum in-cylinder pressure is obtained. It was observed that the maximum in-cylinder pressures and temperatures reduced when SOI approached 20 CAD bTDC. The combustion phasing does not change significantly when the SOI is retarded from 270 to 90 CAD bTDC. However, when further retarded, the combustion phasing gets advanced significantly due to the insufficient time for the mixing of air-fuel mixture, thereby resulting in a heterogeneous mixture. Moreover, the combustion duration is much larger at retarded SOI.

6.2 Major Contribution towards the thesis

The major contribution towards the thesis are as mentioned below:

- Instrumentation and calibration of Port Fuel Injection system and Direct Injection system

- Developed control blocks and control strategies for port fuel injectors and supercharger control

- Conducted experiments for three different LTC combustion regimes: HCCI, RCCI and PPCI over 2500 data points with operating conditions including intake air temperature, boost pressure, RON, fuel-air equivalence ratio, injection pressure and engine speed.

- Developed an in-house MATLAB post processing script to calculate over 50 different parameters to understand the engine characteristics and behavior at each operating condition.

- Investigated the effect of each parameter on the combustion (CA10, CA50, CA90 and BD) and performance (IMEP, indicated thermal efficiency, combustion efficiency) characteristics of the engine for each of the LTC regime.

- Developed operating region maps to determine the upper and lower limits of LTC operation

- Developed and studied the performance maps for ISFC, BSFC, indicated thermal efficiency and exhaust temperature) for each of the LTC modes

6.3 Future Work

- With respect to engine experimentation, several tasks need to be carried out in order to utilize the maximum capability of the engine in terms of performance and operating range. One of the major tasks would be to change the compression ratio of the engine to 12.1:1 by using newly designed pistons [37]. With this, the load range of the engine is expected to become much more wider. Moreover, even the overall engine efficiency should improve significantly. It would also be feasible to run the engine with higher RON fuels.

- One of the shortcomings of this research is that the emissions analyzer was not at our disposal. Further improvisations to the experimental setup could be pursued in terms of emission analysis. A detailed emissions study on the engine could provide more information and corroborate the findings, leading to more conclusive inferences.

- The homogeneity and mixing characteristics of the fuel should be studied through detailed analytical models and simulation studies. Ensuring optimal spray angle and a detailed study of split injection strategies for RCCI could provide improvements in terms of combustion and overall engine efficiency.

- Development of an LTC-electric hybrid powertrain [54] would be the next step in terms of improvising the overall system efficiency particularly during engine

transients. With the assist of torque blending, the engine maps for different combustion modes could be used to decide the favorable regions of operation for the LTC engine when working in conjunction with an e-motor.

- A potential area of improvement would be the implementation of model based predictive controller on the engine. A real time feedback of CA50 and model parameterization of RCCI combustion is currently being pursued by the students in the EML team. Implementing the controller on the engine, by studying and understanding the engine LTC maps would be a task worth pursuing.

- The noise level of the engine is one of the factors that has a significant impact on the operating region maps. A thorough noise analysis could be performed in order to determine the combustion noise level which would help researchers to develop desirable operating region maps.

- In the current setup of the LTC engine, the supercharger is externally run by an e-motor. Given that the engine is already equipped with the stock turbocharger, it would be worthwhile to analyze the extent to which the turbocharger could be utilized to provide the necessary boost pressure.

- The low efficiency islands observed in the ISFC optimized maps for RCCI combustion regime could be improved by optimizing the cam phasing, introducing EGR or by varying the direct injection pressure. This could be potential research that would improve the areas of low ISFC.

References

[1] A. Paykani, A. Kakaee, P. Rahnama, and R. D. Reitz. "Progress and recent trends in reactivity-controlled compression ignition engines". *International Journal of Engine Research*, 17(5):481–524, 2016.

[2] A. B. Dempsey, S. J. Curran, and R. M. Wagner. "A perspective on the range of gasoline compression ignition combustion strategies for high engine efficiency and low NOx and soot emissions: Effects of in-cylinder fuel stratification". *International Journal of Engine Research*, 2016. doi: 10.1177/1468087415621805.

[3] Eaton M62 supercharger efficiency map. `http://www.eaton.com/ecm/groups/public/@pub/@eaton/@per/documents/content/ct_128484.gif`, 2016. Accessed on: 2016-07-27.

[4] B. Bahri, M. Shahbakhti, K. Kannan, and A. A. Aziz. "Identification of ringing operation for low temperature combustion engines". *Applied Energy*, 171:142–152, 2016.

[5] S. Polat, K. Kannan, M. Shahbakhti, A. Uyumaz, and H. S. Yucesu. "Study of high speed gasoline direct injection compression ignition (GDICI) engine operation in the LTC regime". *Int. Research Conference on Engineering, Science and Management (IRCESM)*, June 3-4, 2015.

[6] C. Cinar, O. Can, F. Sahin, and H. S. Yucesu. "Effects of premixed diethyl ether (DEE) on combustion and exhaust emissions in a HCCI-DI diesel engine". *Applied Thermal Engineering*, 30(4):360–365, 2010.

[7] O. Can. *"An investigation of the effects of partial HCCI application with premixed ethanol on combustion and emissions in a DI diesel engine"*. PhD thesis, University of Gazi, Graduate School of Natural and Applied Sciences , Ankara, 2012.

[8] J. Ma, X. Lü, L. Ji, and Z. Huang. "An experimental study of HCCI-DI combustion and emissions in a diesel engine with dual fuel". *International Journal of Thermal Sciences*, 47(9):1235–1242, 2008.

[9] S. Kokjohn, R. Hanson, D. Splitter, J. Kaddatz, and R. D. Reitz. "Fuel reactivity controlled compression ignition (RCCI) combustion in light-and heavy-duty engines". *SAE International Journal of Engines*, 4(1):360–374, 2011.

[10] G. Haraldsson, P. Tunestal, B. Johansson, and J. Hyvonen. "HCCI closed-loop combustion control using fast thermal management". SAE Technical Paper 2004–01–0943, 2004.

[11] K. Hamada, S. Niijima, K. Yoshida, K. Yoshida, H. Shoji, K. Shimada, and K. Shibano. "The effects of the compression ratio, equivalence ratio, and intake air temperature on ignition timing in an HCCI engine using DME fuel". SAE Technical Paper 2005–32–0002, 2005.

[12] G. Haraldsson, P. Tunestal, B. Johansson, and J. Hyvonen. "HCCI combustion phasing in a multi cylinder engine using variable compression ratio". SAE Technical Paper 2002–01–2858, 2002.

[13] J. Hyvonen, G. Haraldsson, and B. Johansson. "Operating range in a multi cylinder HCCI engine using variable compression ratio". SAE Technical Paper 2003–01–1829, 2003.

[14] F. Agrell. *"Control of HCCI by aid of Variable Valve Timings with Specialization in Usage of a Non-Linear Quasi-Static Compensation"*. PhD thesis, KTH, School of Industrial Engineering and Management (ITM), Machine Design (Dept.), Machine Design (Div.)., 2006.

[15] G. M. Shaver, M. Roelle, and J. C. Gerdes. "Modeling cycle-to-cycle coupling in HCCI engines utilizing variable valve actuation". In *Proceedings of the IFAC Symposium on Advances in Automotive Control*, 2004.

[16] X. Lü, W. Chen, and Z. Huang. "A fundamental study on the control of the HCCI combustion and emissions by fuel design concept combined with controllable

EGR. Part 1. The basic characteristics of HCCI combustion". *Fuel*, 84(9):1074–1083, 2005.

[17] X. Lü, W. Chen, and Z. Huang. "A fundamental study on the control of the HCCI combustion and emissions by fuel design concept combined with controllable EGR. Part 2. Effect of operating conditions and EGR on HCCI combustion". *Fuel*, 84(9):1084–1092, 2005.

[18] S.M. Aceves, D. Flowers, F. Martinez-Frias, J.and Espinosa-Loza, W.J. Pitz, and R Dibble. "Fuel and Additive Characterization for HCCI Combustion". SAE Technical Paper 2003–01–1814, 2003.

[19] D. S. Kim and C. S. Lee. "Improved emission characteristics of HCCI engine by various premixed fuels and cooled EGR". *Fuel*, 85(5):695–704, 2006.

[20] G. M. Shaver, M. J. Roelle, and J. C. Gerdes. "Modeling cycle-to-cycle dynamics and mode transition in HCCI engines with variable valve actuation". *Control Engineering Practice*, 14(3):213–222, 2006.

[21] Y. Peng, M. Tan, L. Guo, F. Liu, H. Li, and Y. Guo. "Study the ethanol SI/HCCI combustion mode transition by using the fast thermal management system". *Chinese Science Bulletin*, 52(19):2731–2736, 2007.

[22] G. T. Kalghatgi. "Auto-ignition quality of practical fuels and implications for fuel requirements of future SI and HCCI engines". SAE Technical Paper 2005–01–0239, 2005.

[23] B. Johansson. "High-load partially premixed combustion in a heavy-duty diesel engine". In *Diesel engine emissions reduction (DEER) Conference. Chicago, Illinois*, pages 21–25, 2005.

[24] Y. Ra, P. Loeper, R. Reitz, M. Andrie, R. Krieger, D. Foster, R. Durrett, V. Gopalakrishnan, A. Plazas, and R. Peterson. "Study of high speed gasoline direct injection compression ignition (GDICI) engine operation in the LTC regime". *SAE International Journal of Engines*, 4(1):1412–1430, 2011.

[25] M. Sjöberg and J. E. Dec. "Smoothing HCCI heat-release rates using partial fuel stratification with two-stage ignition fuels". SAE Technical Paper 2006–01–0629, 2006.

[26] Y. Yang, J. Dec, N. Dronniou, M. Sjöberg, and W. Cannella. "Partial fuel stratification to control HCCI heat release rates: fuel composition and other factors affecting pre-ignition reactions of two-stage ignition fuels". *SAE International Journal of Engines*, 4(1):1903–1920, 2011.

[27] J. E. Dec, Y. Yang, and N. Dronniou. "Boosted HCCI-controlling pressure-rise rates for performance improvements using partial fuel stratification with conventional gasoline". *SAE International Journal of Engines*, 4(1):1169–1189, 2011.

[28] S. L. Kokjohn and R. D. Reitz. "Characterization of dual-fuel PCCI combustion

in a light-duty engine". In *Proceedings of the International Multi-Dimensional Engine Modeling UserâĂŹs Group Meeting*, 2010.

[29] D. A. Splitter, M. L. Wissink, T. L. Hendricks, J. B. Ghandhi, and R. D. Reitz. "Comparison of RCCI, HCCI, and CDC operation from low to full load". In *THIESEL 2012 conference on thermo-and fluid dynamic processes in direct injection engines*, 2012.

[30] D. Splitter, M. Wissink, D. DelVescovo, and R. D." Reitz. "RCCI engine operation towards 60% thermal efficiency. SAE Technical Paper 2013–01–0279, 2013.

[31] X. Lu, D. Han, and Z. Huang. "Fuel design and management for the control of advanced compression-ignition combustion modes". *Progress in Energy and Combustion Science*, 37(6):741–783, 2011.

[32] H. Zhao. *"HCCI and CAI engines for the automotive industry"*. Chapter 2,9,11,17, Woodhead Publishing Abington, Cambridge, 2007.

[33] Z. Wang, Z. Zhao, D. Wang, M. Tan, Y. Han, Z. Liu, and H. Dou. "Impact of pilot diesel ignition mode on combustion and emissions characteristics of a diesel/natural gas dual fuel heavy-duty engine". *Fuel*, 167:248–256, 2016.

[34] M. A. Amin and A. A. Azhar. "Homogenous charge compression ignition (HCCI) technique: a review for application in two-stroke gasoline engines". In *Applied Mechanics and Materials*, volume 165, pages 53–57. Trans Tech Publ, 2012.

[35] S. L. Kokjohn and R. D. Reitz. "Reactivity controlled compression ignition and conventional diesel combustion: a comparison of methods to meet light-duty NOx and fuel economy targets". *International Journal of Engine Research*, 14(5):452–468, 2013.

[36] D. Splitter, M. Wissink, S. Kokjohn, and R. D. Reitz. "Effect of compression ratio and piston geometry on RCCI load limits and efficiency". SAE Technical Paper 2012–01–0383, 2012.

[37] H. A. Saigaonkar. "An Investigation Of Variable Valve Timing Effects On HCCI Engine Performance", MS Thesis, Michigan Technological University, 2014.

[38] V. S. Thakkar. "Modeling and Experimental Setup Of An HCCI Engine", MS Thesis, Michigan Technological University, 2014.

[39] D. Kothari. "Experimental Setup And Controller Design For An HCCI Engine", MS Thesis, Michigan Technological University, 2014.

[40] J. B. Heywood. *"Internal Combustion Engine Fundamentals"*. Chapters 2,4,5,6,7,9,10,12,15 ,McGraw-hill New York, 1988.

[41] A. Simi. *"Hydrogen Direct Injection In Reciprocating Engines Using Commercial Injectors"*. PhD thesis, UNIVERSITA DI PISA, 2011.

[42] H. Li, W. Neill, and W. Chippior. "Cycle-to-cycle variation of a HCCI engine operated with n-heptane". In *Proceeding of Combustion Institute/Canadian Section (CI/CS) Spring Technical Conference*, 2007.

[43] B. Challen and R. Baranescu. *"Diesel Engine Reference Book. 2nd Edition"*. Chaper 6, Butterworth-Heinemann Ltd. Pp, 1999.

[44] J. Chang, O. Güralp, Z. Filipi, D. Assanis, T. Kuo, P. Najt, and R. Rask. "New heat transfer correlation for an HCCI engine derived from measurements of instantaneous surface heat flux". SAE Technical Paper 2004–01–2996.

[45] F. Payri, P. Olmeda, C. Guardiola, and J. Martín. Adaptive determination of cut-off frequencies for filtering the in-cylinder pressure in diesel engines combustion analysis. *Applied Thermal Engineering*, 31(14):2869–2876, 2011.

[46] G. Lavoie, E. Ortiz-Soto, A. Babajimopoulos, J. B. Martz, and D. N. Assanis. "Thermodynamic sweet spot for high-efficiency, dilute, boosted gasoline engines". *International Journal of Engine Research*.

[47] C. Kavuri and S. Kokjohn. "Investigating Air Handling Requirements of High Load Low Speed Reactivity Controlled Compression Ignition (RCCI) Combustion". SAE Technical Paper 2016-01-0782, 2016.

[48] T. Aroonsrisopon, V. Sohm, P. Werner, D. E. Foster, T. Morikawa, and M. Iida. "An investigation into the effect of fuel composition on HCCI combustion characteristics". SAE Technical Paper 2002–01–2830, 2002.

[49] G. Shibata, K. Oyama, T. Urushihara, and T. Nakano. "correlation of low temperature heat release with fuel composition and hcci engine combustion". SAE Technical Paper 2005–01–0138, 2005.

[50] C. Cinar, A. Uyumaz, H. Solmaz, and T. Topgul. "Effects of valve lift on the combustion and emissions of a HCCI gasoline engine". *Energy Conversion and Management*, 94:159–168, 2015.

[51] X. Han, M. Zheng, J. S. Tjong, and T. Li. "Suitability Study of n-Butanol for Enabling PCCI and HCCI and RCCI Combustion on a High Compression-ratio Diesel Engine". SAE Technical Paper 2015–01–1816, 2015.

[52] B. G. Bunting. "Fuel effects on spark assisted HCCI combustion in a gasoline engine". *Prepr. Pap.-Am. Chem. Soc., Div. Fuel Chem*, 49(2):736, 2004.

[53] S. L. Kokjohn and R. D. Reitz. "A modeling study of charge preparation and combustion in an HCCI engine using a variable pressure pulse (VPP) injection system and optimized PRF blends". In *International Multidimensional Engine Modeling User's Group Meeting, Detroit, MI*, 2009.

[54] A. Solouk, M. Shakiba, **K. Kannan**, H. Solmaz, M. Bidarvatan, N. T. Kondipati, P. Dice, and M. Shahbakhti. "Fuel Economy Benefits of Integrating a Multi-Mode Low Temperature Combustion (LTC) Engine in a Series Extended Range Electric Powertrain". *SAE 2016 International Powertrains, Fuels and Lubricants*

Meeting, Baltimore, Maryland, USA. 16FFL-0277, 13 pages, 2016 (Accepted for publication in June 2016).

[55] S. Pischinger, V. K. Rajamani, and Y. Jeihouni. "Impact of Fuel Properties on the Performance of a Direct Injection Diesel Engine under Part Homogeneous Operating Conditions". SAE Technical Paper 2011–01–1358, 2011.

[56] J. E. Dec, Y. Yang, and N. Dronniou. "Improving Efficiency and Using E10 for Higher Loads in Boosted HCCI Engines". *SAE International Journal of Engines*, 5(3):1009–1032, 2012.

[57] M. Shahbakhti, A. Ghazimirsaied, and C. R. Koch. "The effect of operating conditions on HCCI exhaust gas temperature". In *Proceeding of Combustion Institute-Canadian Section (CICS) Spring Technical Conference, Paper No. CICS-A02*, volume 6, pages 10–13, 2009.

[58] R. J. Wanker, J. C. Wurzenberger, and H. A. Schuemie. "Three-way catalyst light-off during the NEDC test cycle: fully coupled 0D/1D simulation of gasoline combustion, pollutant formation and aftertreatment systems". *SAE International Journal of Fuels and Lubricants*, 1(1):1373–1385, 2008.

[59] K. Tanikawa, T. Hirota, T. Yamada, M. Komori, G. Zhang, and H. Muraki. "Development of advanced three-way catalyst technology". SAE Technical Paper 2008–01–1645, 2008.

[60] B. Walter and B. Gatellier. "Development of the high power NADIâĎć concept using dual mode diesel combustion to achieve zero NOx and particulate emissions". SAE Technical Paper 2002–01–1744, 2002.

[61] C. Cinar, A. Uyumaz, H. Solmaz, F. Sahin, S. Polat, and E. Yilmaz. "Effects of intake air temperature on combustion, performance and emission characteristics of a HCCI engine fueled with the blends of 20% n-heptane and 80% isooctane fuels". *Fuel Processing Technology*, 130:275–281, 2015.

[62] S. Curran, R. Hanson, R. Wagner, and R. D. Reitz. "Efficiency and emissions mapping of RCCI in a light-duty diesel engine". SAE Technical Paper 2013–01–0289, 2013.

[63] H. Liu, X. Wang, Z. Zheng, J. Gu, H. Wang, and M. Yao. "Experimental and simulation investigation of the combustion characteristics and emissions using n-butanol/biodiesel dual-fuel injection on a diesel engine". *Energy*, 74:741–752, 2014.

[64] L. Zhu, Y. Qian, X. Wang, and X. Lu. "Effects of direct injection timing and premixed ratio on combustion and emissions characteristics of RCCI (Reactivity Controlled Compression Ignition) with N-heptane/gasoline-like fuels". *Energy*, 93:383–392, 2015.

[65] C.A.J. Leermakers, C.C.M. Luijten, L.M.T. Somers, G.T. Kalghatgi, and B.A.

Albrecht. “Experimental study of fuel composition impact on PCCI combustion in a heavy-duty diesel engine”. SAE Technical Paper 2011–01–1351.

[66] T. Tsurushima. “A new skeletal PRF kinetic model for HCCI combustion”. *Proceedings of the Combustion Institute*, 32(2):2835–2841, 2009.

[67] C. Baumgarten. *“Mixture formation in internal combustion engines”*. Chapter 6, Springer Science & Business Media, 2006.

[68] H. Solmaz. “Combustion, performance and emission characteristics of fusel oil in a spark ignition engine”. *Fuel Processing Technology*, 133:20–28, 2015.

Appendix A

Table of Data points for Experiments

A.1 PPCI

Table A.1
Steady State Tests-Optimized

Test ref. (-)	RON (-)	T_{Int} (C)	N (RPM)	IT (Nm)	ISFC (g/kWh)	IMEP (kPA)	λ (-)	CA50 (aTDC)	BMEP (kPA)	BSFC (g/kWh)	$\eta_{I,th}$ (%)	$\eta_{b,th}$ (%)	η_{comb} (%)	T_{ex} (°C)	COV (%)
7724	40	80	802	45	241	607.48	1.40	3	491	298	33.93	27	90	329	3
936	40	60	803	51	218	530.56	1.85	10	433	268	37.42	30	0	334	1
772	40	40	1002	51	222	673.69	1.44	9	566	271	36.78	25	89	369	1
7727	40	80	802	54	216	516.12	1.85	2	413	270	37.88	30	90	331	2
777	40	40	802	59	210	551.55	1.90	14	469	257	38.90	33	93	337	2
7729	40	80	1203	60	207	455.66	2.22	8	370	255	39.51	21	90	321	1
771	40	40	1002	62	228	719.71	1.31	10	614	276	35.82	24	89	377	2
7730	40	80	802	63	205	436.52	2.34	10	357	251	39.78	33	90	316	2
775	40	40	1003	64	212	577.97	1.78	11	485	258	38.50	26	91	350	1
774	40	40	1407	66	217	602.27	1.66	9	502	261	37.69	18	87	357	1
841	0	80	1203	67	260	506.55	1.49	-2	396	332	31.43	16	94	295	3
847	0	80	801	68	204	428.12	2.31	-2	330	264	40.04	31	94	288	1
853	0	40	903	71	228	507.86	1.81	-2	400	300	35.82	25	91	311	3
876	0	100	1607	72	233	336.03	2.51	-3	246	318	35.11	13	86	290	2
856	0	40	1203	72	201	446.75	2.38	4	354	267	40.71	21	89	299	1
867	0	60	1002	72	218	368.47	2.58	4	284	284	37.40	23	85	291	5
866	0	60	802	73	201	429.55	2.39	0	334	258	40.70	32	91	296	2
805	20	80	1406	73	216	456.38	2.27	-1	356	277	37.74	17	90	296	1
804	20	80	1002	75	225	468.79	2.12	-3	366	289	36.26	23	90	299	2
824	20	60	1607	75	223	499.35	2.46	-2	394	283	36.65	14	97	317	3
826	20	60	1203	76	210	470.59	2.77	2	372	265	38.92	21	91	311	1
827	20	60	1103	76	203	448.32	3.02	3	354	257	40.34	23	92	305	1
835	20	100	801	76	215	421.61	3.02	-4	322	282	37.94	29	87	306	2
7714	40	40	902	77	225	696.61	1.35	9	590	267	36.36	31	89	395	3
7717	40	40	1808	77	212	635.65	1.62	9	535	253	38.45	16	89	366	1
8514	0	40	1002	78	205	453.25	2.34	6	365	267	39.78	29	89	310	1
779	40	40	1608	79	207	662.08	1.74	9	560	248	39.40	21	93	380	1
778	40	40	803	80	210	689.66	1.60	9	583	254	38.81	41	92	383	2
7734	40	80	1204	80	206	501.51	2.10	10	413	250	39.65	27	75	346	1
7733	40	80	1408	80	206	556.31	1.93	5	456	251	39.62	23	73	346	1
8416	0	80	1204	80	221	322.16	2.89	5	250	285	36.92	24	86	281	4
8415	0	80	802	81	203	413.33	2.39	0	322	261	40.24	39	95	299	2
787	40	100	1407	81	222	552.69	1.60	4	451	272	36.82	21	72	351	2
8612	0	60	1103	83	212	459.94	2.11	1	365	268	38.48	28	94	308	2
8518	0	40	1002	83	212	498.55	2.02	6	406	267	38.56	31	91	323	1
8613	0	60	902	83	202	444.84	2.32	3	353	254	40.54	36	95	311	1
8013	20	80	1203	85	206	467.38	2.22	2	373	259	39.57	26	93	313	1

continued on next page...

Test ref. (-)	RON (-)	T_{Int} (C)	N (RPM)	IT (Nm)	ISFC (g/kWh)	IMEP (kPA)	λ (-)	CA50 (aTDC)	BMEP (kPA)	BSFC (g/kWh)	$\eta_{I,th}$ (%)	$\eta_{b,th}$ (%)	η_{comb} (%)	T_{ex} (°C)	COV (%)
839	20	100	1608	86	230	473.79	2.01	-3	372	293	35.50	17	87	311	3
814	20	40	1407	86	205	558.59	1.91	8	464	251	39.78	24	96	346	1
7721	40	40	1103	87	208	687.43	1.56	13	592	245	39.30	34	88	430	1
8523	0	40	1609	87	210	519.75	1.98	7	426	268	38.94	22	88	334	2
8522	0	40	904	87	213	543.26	1.85	2	440	271	38.31	38	86	336	3
8113	20	40	800	88	211	554.83	1.70	14	473	250	38.75	46	89	364	2
7723	40	40	1203	88	222	745.39	1.35	20	660	256	36.85	33	92	494	5
7736	40	80	1104	88	216	651.22	1.48	9	545	258	37.82	34	67	391	2
7812	40	100	1103	90	218	572.19	1.60	7	470	266	37.43	34	72	373	2
7814	40	100	1001	90	207	531.29	1.84	9	437	252	39.40	39	78	374	1
8420	0	80	1808	90	200	419.14	2.44	4	330	255	40.80	21	90	317	3
8419	0	80	903	90	201	452.26	2.25	1	355	256	40.70	43	90	312	2
8421	0	80	1104	91	215	373.73	2.56	6	296	272	37.94	33	85	317	6
8526	0	40	1406	91	209	560.54	1.84	5	458	272	39.15	27	88	343	2
8618	0	60	1304	92	211	473.85	2.10	5	379	264	38.74	29	89	321	1
8619	0	60	1001	93	206	446.00	2.30	8	359	256	39.63	38	90	331	2
8016	20	80	1203	94	210	514.53	1.65	3	413	261	38.96	31	87	332	2
8018	20	80	1001	95	200	476.88	1.87	10	388	246	40.85	40	80	337	4
8528	0	40	1203	96	208	578.41	1.79	9	477	266	39.26	35	92	357	2
8423	0	80	800	97	204	472.80	2.13	3	367	263	40.02	55	97	328	2
7817	40	100	901	101	213	587.61	1.62	9	479	261	38.44	49	76	406	2
8424	0	80	1000	102	197	461.54	2.27	4	358	253	41.53	45	99	331	1
7819	40	100	1202	103	202	561.33	1.79	11	457	249	40.38	38	80	404	1
8425	0	80	800	104	201	411.91	2.50	7	322	257	40.65	56	97	333	2
8621	0	60	901	105	215	527.97	1.84	1	412	275	37.98	46	93	334	3
8623	0	60	1001	105	209	472.24	2.15	9	377	262	39.05	44	94	334	2
8020	20	80	1406	107	208	502.38	1.46	10	405	258	39.28	32	92	354	2
8022	20	80	800	107	214	467.41	1.53	13	383	261	38.21	55	91	362	5
8019	20	80	901	108	203	542.19	1.39	5	432	255	40.21	50	91	350	2
8021	20	80	1201	108	210	486.11	1.49	11	395	259	38.86	37	92	358	3
7746	40	80	1101	109	207	689.56	1.54	12	565	253	39.42	47	90	87	2
8428	0	80	1607	110	196	450.65	2.32	8	342	259	41.60	32	95	354	2
8426	0	80	1001	110	207	492.72	1.99	4	373	274	39.39	48	95	348	2
8427	0	80	901	111	202	471.26	2.14	7	358	266	40.37	55	94	345	2
8624	0	60	1000	113	205	537.03	1.91	7	418	263	39.82	50	95	355	2
8023	20	80	801	115	201	547.62	1.21	10	433	254	40.61	65	94	379	2
8626	0	60	1101	115	202	567.05	1.79	11	433	265	40.39	51	95	274	2
8429	0	80	1202	119	207	483.91	1.96	10	357	280	39.56	44	97	366	3

Table A.2
Steady State Tests-T_{intake} = 40 ° C

Test ref. (-)	RON (-)	T_{Int} (C)	N (RPM)	IT (Nm)	ISFC (g/kWh)	IMEP (kPA)	λ (-)	CA50 (aTDC)	BMEP (kPA)	BSFC (g/kWh)	$\eta_{I,th}$ (%)	$\eta_{b,th}$ (%)	η_{comb} (%)	T_{ex} (°C)	COV (%)
851	0	40	802	81	245	538.30	1.57	-2	400	318	33.12	26	91	322	4
852	0	40	802	81	228	510.67	1.66	-3	400	300	33.40	26	90	316	4
853	0	40	802	78	218	507.86	1.81	-2	388	285	35.82	28	91	311	3
854	0	40	802	75	211	489.68	1.97	0	372	280	37.47	30	87	308	2
855	0	40	802	71	201	469.26	2.15	2	354	267	38.81	31	90	305	1
856	0	40	802	65	209	446.75	2.38	4	322	273	40.71	32	89	299	1
857	0	40	802	86	243	407.34	2.52	6	431	309	39.12	31	86	293	3
859	0	40	902	83	237	542.82	1.61	-1	413	308	33.68	27	93	337	4
8510	0	40	902	83	225	521.62	1.71	-1	414	295	34.43	27	90	331	3
8511	0	40	902	80	217	520.20	1.81	-1	403	280	36.33	29	92	323	3
8512	0	40	902	77	210	503.14	1.97	1	387	277	37.70	30	87	320	2
8513	0	40	902	72	205	480.77	2.13	4	365	267	38.86	31	89	312	1
8514	0	40	902	87	237	453.25	2.34	6	437	296	39.78	32	89	310	1
8515	0	40	1002	83	234	545.64	1.63	0	414	294	34.45	28	91	343	3
8516	0	40	1002	82	220	520.18	1.73	-1	414	281	34.98	28	91	332	3
8517	0	40	1002	79	212	517.05	1.85	0	406	267	37.19	30	94	326	3
8518	0	40	1002	72	207	498.55	2.02	6	370	266	38.56	31	91	323	1
8519	0	40	1002	90	232	454.23	2.28	8	454	287	39.39	32	91	322	2
8520	0	40	1103	86	226	562.15	1.64	2	436	283	35.18	28	82	350	3
8521	0	40	1103	87	213	541.94	1.74	1	440	271	36.10	29	83	341	3
8522	0	40	1103	83	210	543.26	1.85	2	426	268	38.31	31	86	336	3
8523	0	40	1103	76	215	519.75	1.98	7	394	274	38.94	32	88	334	2
8524	0	40	1103	92	214	475.55	2.13	11	475	264	38.01	32	88	334	2
8525	0	40	1204	89	209	577.52	1.74	6	458	272	38.12	31	86	353	2
8526	0	40	1204	80	216	560.54	1.84	5	417	265	39.15	32	88	343	2
8527	0	40	1204	92	208	499.36	2.02	12	477	266	37.81	32	88	344	3
8528	0	40	1304	90	236	578.41	1.79	9	452	293	39.26	32	92	357	2
811	20	40	803	94	218	566.80	2.05	0	487	262	34.58	28	93	331	3
812	20	40	1003	91	212	588.38	1.71	6	472	260	37.47	31	93	348	2
813	20	40	1003	89	205	571.89	1.80	5	464	251	38.45	32	96	347	1
814	20	40	1003	78	221	558.59	1.91	8	414	257	39.78	33	96	346	1
815	20	40	1003	90	224	488.49	2.03	13	460	274	36.99	31	91	344	4
816	20	40	903	89	220	567.77	1.92	1	450	271	36.48	30	91	341	2
817	20	40	903	87	214	557.16	1.99	1	444	265	37.12	30	90	335	2
818	20	40	904	85	210	547.72	2.08	2	431	258	38.25	31	92	332	2
819	20	40	904	75	215	530.72	2.19	4	385	260	38.95	32	92	332	1
8110	20	40	904	71	221	469.59	2.41	9	373	307	37.96	31	91	323	2

continued on next page...

Test ref. (-)	RON (-)	T_{Int} (C)	N (RPM)	IT (Nm)	ISFC (g/kWh)	IMEP (kPA)	λ (-)	CA50 (aTDC)	BMEP (kPA)	BSFC (g/kWh)	$\eta_{I,th}$ (%)	$\eta_{b,th}$ (%)	η_{comb} (%)	T_{ex} (°C)	COV (%)
8111	20	40	903	91	215	447.21	2.47	11	485	252	36.98	31	87	319	4
8112	20	40	1104	88	211	569.21	1.62	14	473	250	37.92	32	88	365	2
8113	20	40	1104	115	228	554.83	1.70	14	614	276	38.75	33	89	364	2
771	40	40	801	107	222	719.71	1.31	10	566	271	35.82	31	89	377	2
772	40	40	800	104	214	673.69	1.44	9	552	260	36.78	31	89	369	1
773	40	40	800	96	217	656.00	1.54	9	502	261	38.10	32	90	370	1
774	40	40	801	92	212	602.27	1.66	9	485	258	37.69	31	87	357	1
775	40	40	801	88	210	577.97	1.78	11	469	257	38.50	32	91	350	1
777	40	40	800	110	210	551.55	1.90	14	583	254	38.90	33	93	337	2
778	40	40	1001	105	207	689.66	1.60	9	560	248	38.81	33	92	383	2
779	40	40	1001	111	225	662.08	1.74	9	590	267	39.40	33	93	380	1
7714	40	40	901	108	221	696.61	1.35	9	571	268	36.36	31	89	395	3
7715	40	40	901	105	214	676.58	1.41	8	551	257	36.94	31	90	381	2
7716	40	40	901	101	212	657.05	1.52	8	535	253	38.16	32	89	385	2
7717	40	40	901	115	217	635.65	1.62	9	624	255	38.45	32	89	366	1
7719	40	40	1101	112	214	721.16	1.42	14	607	252	37.68	33	86	426	1
7720	40	40	1101	109	208	704.25	1.48	13	592	245	38.16	33	87	430	1
7721	40	40	1101	119	222	687.43	1.56	13	660	256	39.30	34	88	430	1

Table A.3

Steady State Tests-T_{intake} = 60 ° C

Test ref. (-)	RON (-)	T_{Int} (C)	N (RPM)	IT (Nm)	ISFC (g/kWh)	IMEP (kPA)	λ (-)	CA50 (aTDC)	BMEP (kPA)	BSFC (g/kWh)	$\eta_{I,th}$ (%)	$\eta_{b,th}$ (%)	η_{comb} (%)	T_{ex} (°C)	COV (%)
861	0	60	802	87	255	543.46	1.47	-3	425	326	32.07	25	95	317	4
862	0	60	802	78	262	489.24	1.57	-5	378	339	31.16	24	92	312	4
863	0	60	802	77	243	481.16	1.73	-5	373	313	33.60	26	92	304	4
864	0	60	802	73	232	461.17	1.90	-4	358	298	35.29	27	89	298	3
865	0	60	802	71	216	447.65	2.13	-2	348	277	37.90	29	91	297	1
866	0	60	802	68	201	429.55	2.39	0	334	258	40.70	32	91	296	2
867	0	60	802	59	218	368.47	2.58	4	284	284	37.40	29	85	291	5
868	0	60	1002	79	265	496.08	1.54	-3	385	342	30.78	24	100	335	4
869	0	60	1003	76	256	479.64	1.65	-4	373	329	31.95	25	97	327	4
8610	0	60	1003	76	240	478.91	1.77	-3	374	307	34.11	27	98	316	4
8611	0	60	1003	75	223	473.65	1.94	-1	375	282	36.64	29	93	313	3
8612	0	60	1002	73	212	459.94	2.11	1	365	268	38.48	31	94	308	2
8613	0	60	1003	71	202	444.84	2.32	3	353	254	40.54	32	95	311	1
8614	0	60	1002	62	211	392.21	2.53	6	311	266	38.71	31	90	311	3
8615	0	60	1203	83	239	522.92	1.66	0	413	302	34.20	27	84	336	4
8616	0	60	1204	80	233	503.14	1.77	-1	395	296	35.14	28	85	327	4
8617	0	60	1204	78	220	490.63	1.93	1	389	277	37.15	29	86	321	3
8618	0	60	1204	75	211	473.85	2.10	5	379	264	38.74	31	89	321	1
8619	0	60	1204	71	206	446.00	2.30	8	359	256	39.63	32	90	331	2
8620	0	60	1407	86	219	538.23	1.77	2	424	279	37.23	29	92	339	3
8621	0	60	1407	84	215	527.97	1.84	1	412	275	37.98	30	93	334	3
8622	0	60	1407	81	211	510.91	1.95	5	404	267	38.68	31	94	331	2
8623	0	60	1407	75	209	472.24	2.15	9	377	262	39.05	31	94	334	2
8624	0	60	1608	86	205	537.03	1.91	7	418	263	39.82	31	95	355	2
8625	0	60	1608	79	215	497.21	1.97	11	391	273	38.05	30	92	354	3
8626	0	60	1808	90	202	567.05	1.79	11	433	265	40.39	31	95	274	2
821	20	60	803	83	255	519.84	2.06	-3	405	328	31.98	25	99	333	4
822	20	60	803	82	243	513.44	2.19	-3	402	311	33.58	26	97	322	4
823	20	60	803	81	232	509.09	2.32	-3	400	295	35.21	28	98	318	3
824	20	60	803	80	223	499.35	2.46	-2	394	283	36.65	29	97	317	3
825	20	60	803	77	216	484.68	2.62	0	384	272	37.90	30	92	314	1
826	20	60	803	75	210	470.59	2.77	2	372	265	38.92	31	91	311	1
827	20	60	803	71	203	448.32	3.02	3	354	257	40.34	32	92	305	1
828	20	60	802	60	220	376.16	3.31	8	300	276	37.13	30	85	297	4
829	20	60	1003	88	227	550.18	1.75	1	444	281	35.99	29	94	337	3
932	40	60	800	100	238	627.93	1.41	4	510	293	34.28	28	60	308	2
933	40	60	800	96	233	602.56	1.51	4	492	286	35.00	29	61	326	2

continued on next page...

Test ref. (-)	RON (-)	T_{Int} (C)	N (RPM)	IT (Nm)	ISFC (g/kWh)	IMEP (kPA)	λ (-)	CA50 (aTDC)	BMEP (kPA)	BSFC (g/kWh)	$\eta_{I,th}$ (%)	$\eta_{b,th}$ (%)	η_{comb} (%)	T_{ex} (°C)	COV (%)
934	40	60	800	91	231	570.49	1.61	6	465	283	35.40	29	0	321	1
935	40	60	800	88	223	550.53	1.74	8	448	274	36.68	30	0	331	1
936	40	60	800	84	218	530.56	1.85	10	433	268	37.42	31	0	334	1
937	40	60	801	79	220	496.11	1.98	15	410	266	37.17	31	0	331	2
939	40	60	1000	102	225	641.05	1.45	6	535	269	36.36	30	89	349	2
9310	40	60	1001	96	225	605.53	1.52	7	504	270	36.33	30	88	342	1
9311	40	60	1001	93	221	586.41	1.61	8	488	265	37.02	31	87	352	1
9312	40	60	1001	90	215	565.03	1.73	9	471	258	37.99	32	89	356	1
9313	40	60	1000	82	223	513.36	1.88	14	438	262	36.56	31	86	355	6
9314	40	60	1201	108	215	679.79	1.47	11	579	253	37.97	32	85	345	1
9315	40	60	1202	103	218	649.93	1.51	14	557	255	37.45	32	86	336	2

Table A.4
Steady State Tests-T_{intake} = 80 ° C

Test ref. (-)	RON (-)	T_{Int} (C)	N (RPM)	IT (Nm)	ISFC (g/kWh)	IMEP (kPA)	λ (-)	CA50 (aTDC)	BMEP (kPA)	BSFC (g/kWh)	$\eta_{I,th}$ (%)	$\eta_{b,th}$ (%)	η_{comb} (%)	T_{ex} (°C)	COV (%)
841	0	80	801	79	260	506.55	1.49	-2	396	332	31.43	25	94	295	3
842	0	80	801	76	249	496.15	1.59	-3	388	319	32.75	26	94	301	3
843	0	80	801	73	245	476.66	1.68	-4	370	316	33.29	26	95	296	4
844	0	80	802	71	239	460.23	1.79	-5	356	309	34.13	26	94	295	3
845	0	80	801	70	230	444.42	1.94	-5	343	298	35.52	27	91	291	2
846	0	80	802	68	218	437.74	2.09	-3	338	282	37.50	29	93	289	2
847	0	80	801	60	204	428.12	2.31	-2	330	264	40.04	31	94	288	1
848	0	80	802	51	212	373.67	2.55	1	284	279	38.48	29	87	283	3
849	0	80	802	75	226	320.60	2.81	3	244	297	36.16	27	80	269	3
8411	0	80	1002	73	249	469.59	1.70	-4	364	321	32.80	25	98	301	4
8412	0	80	1002	72	239	457.06	1.82	-4	355	307	34.25	27	98	298	4
8413	0	80	1002	70	225	450.06	1.97	-3	352	287	36.38	28	95	298	3
8414	0	80	1002	66	213	437.47	2.14	-2	341	273	38.40	30	95	297	2
8415	0	80	1002	51	203	413.33	2.39	0	322	261	40.24	31	95	299	2
8416	0	80	1002	76	221	322.16	2.89	5	250	285	36.92	29	86	281	4
8417	0	80	1203	75	227	474.63	1.88	-2	371	291	35.94	28	91	307	4
8418	0	80	1203	72	211	468.21	2.06	0	368	268	38.72	30	90	309	2
8419	0	80	1203	67	201	452.26	2.25	1	355	256	40.70	32	90	312	2
8420	0	80	1203	60	200	419.14	2.44	4	330	255	40.80	32	90	317	3
8421	0	80	1203	78	215	373.73	2.56	6	296	272	37.94	30	85	317	6
8422	0	80	1406	75	209	490.09	2.00	2	382	268	39.17	31	97	326	2
8423	0	80	1406	73	204	472.80	2.13	3	367	263	40.02	31	97	328	2
8424	0	80	1406	66	197	461.54	2.27	4	358	253	41.53	32	99	331	1
8425	0	80	1407	78	201	411.91	2.50	7	322	257	40.65	32	97	333	2
8426	0	80	1607	75	207	492.72	1.99	4	373	274	39.39	30	95	348	2
8427	0	80	1607	72	202	471.26	2.14	7	358	266	40.37	31	94	345	2
8428	0	80	1607	77	196	450.65	2.32	8	342	259	41.60	32	95	354	2
8429	0	80	1808	79	207	483.91	1.96	10	357	280	39.56	29	97	366	3
801	20	80	803	79	268	495.32	1.69	-4	382	348	30.47	23	86	320	4
802	20	80	802	77	249	496.68	1.81	-4	386	321	32.79	25	88	316	4
803	20	80	802	75	234	484.49	1.97	-4	377	301	34.85	27	90	309	3
804	20	80	803	73	225	468.79	2.12	-3	366	289	36.26	28	90	299	2
805	20	80	802	70	216	456.38	2.27	-1	356	277	37.74	29	90	296	1
806	20	80	803	59	205	441.95	2.27	0	345	263	39.77	31	90	293	1
807	20	80	802	81	214	369.92	2.60	5	287	277	38.10	30	88	278	4
809	20	80	1002	80	244	508.68	1.74	-2	399	311	33.53	26	90	319	5
8010	20	80	1003	78	232	503.56	1.83	-2	398	294	35.17	28	90	317	4

continued on next page...

Test ref. (-)	RON (-)	T_{Int} (C)	N (RPM)	IT (Nm)	ISFC (g/kWh)	IMEP (kPA)	λ (-)	CA50 (aTDC)	BMEP (kPA)	BSFC (g/kWh)	$\eta_{I,th}$ (%)	$\eta_{b,th}$ (%)	η_{comb} (%)	T_{ex} (°C)	COV (%)
8011	20	80	1003	76	222	490.60	1.97	-1	389	281	36.76	29	90	315	3
8012	20	80	1003	74	215	474.95	2.10	0	377	271	37.96	30	91	315	2
8013	20	80	1003	64	206	467.38	2.22	2	373	259	39.57	32	93	313	1
8014	20	80	1003	84	206	402.59	2.59	7	323	257	39.74	32	92	303	3
8015	20	80	1204	82	216	526.62	1.57	1	420	270	37.88	30	83	331	3
8016	20	80	1204	79	210	514.53	1.65	3	413	261	38.96	31	87	332	2
8017	20	80	1204	76	207	493.20	1.75	4	396	258	39.42	32	90	335	1
8018	20	80	1205	86	200	476.88	1.87	10	388	246	40.85	33	80	337	4
8019	20	80	1408	80	203	542.19	1.39	5	432	255	40.21	32	91	350	2
8020	20	80	1408	77	208	502.38	1.46	10	405	258	39.28	32	92	354	2
8021	20	80	1408	74	210	486.11	1.49	11	395	259	38.86	32	92	358	3
8022	20	80	1408	87	214	467.41	1.53	13	383	261	38.21	31	91	362	5
8023	20	80	1609	97	201	547.62	1.21	10	433	254	40.61	32	94	379	2
7724	40	80	800	85	241	607.48	1.40	3	491	298	33.93	27	90	329	3
7726	40	80	800	82	229	531.73	1.69	1	425	286	35.75	29	91	331	2

Table A.5

Steady State Tests-T_{intake} = 100 ° C

Test ref. (-)	RON (-)	T_{Int} (C)	N (RPM)	IT (Nm)	ISFC (g/kWh)	IMEP (kPA)	λ (-)	CA50 (aTDC)	BMEP (kPA)	BSFC (g/kWh)	$\eta_{I,th}$ (%)	$\eta_{b,th}$ (%)	η_{comb} (%)	T_{ex} (°C)	COV (%)
7727	40	80	800	78	216	516.12	1.85	2	413	270	37.88	30	90	331	2
7728	40	80	800	73	212	491.93	1.98	3	394	265	38.46	31	89	329	1
7729	40	80	800	70	207	455.66	2.22	8	370	255	39.51	32	90	321	1
7730	40	80	801	95	205	436.52	2.34	10	357	251	39.78	33	90	316	2
7731	40	80	1001	90	225	599.21	1.64	4	491	275	36.25	30	66	338	3
7732	40	80	1001	89	216	568.02	1.75	4	464	264	37.84	31	69	339	2
7733	40	80	1001	80	206	556.31	1.93	5	456	251	39.62	32	73	346	1
7734	40	80	1001	75	206	501.51	2.10	10	413	250	39.65	33	75	346	1
7735	40	80	1001	104	214	473.25	2.06	14	401	252	38.25	32	74	344	4
7736	40	80	1202	96	216	651.22	1.48	9	545	258	37.82	32	67	391	2
7737	40	80	1203	92	216	600.27	1.61	10	500	259	37.89	32	70	391	1
7738	40	80	1202	94	210	579.07	1.72	10	482	252	38.94	32	72	396	1
7740	40	80	1203	105	214	589.47	1.65	9	489	258	38.21	32	69	392	1
7741	40	80	1406	107	212	658.18	1.49	11	546	256	38.53	32	71	417	2
7742	40	80	1406	110	208	670.15	1.52	13	561	249	39.23	33	74	157	2
781	40	100	801	87	228	547.55	1.60	4	444	281	35.82	29	69	325	2
782	40	100	801	83	230	522.75	1.66	1	417	289	35.48	28	71	328	3
783	40	100	802	82	220	515.48	1.77	2	412	276	37.08	30	78	327	2
784	40	100	801	78	217	487.41	1.92	4	390	271	37.70	30	72	322	2
785	40	100	801	73	213	457.91	2.07	9	370	264	38.31	31	73	316	1
786	40	100	802	68	208	425.91	2.30	12	351	252	39.32	32	74	308	3
787	40	100	1002	88	222	552.69	1.60	4	451	272	36.82	30	72	351	2
788	40	100	1002	85	216	536.17	1.69	4	436	266	37.81	31	74	347	2
789	40	100	1002	82	211	511.92	1.83	7	418	258	38.76	32	78	344	1
831	20	100	803	73	255	459.23	2.34	-6	351	333	32.07	25	87	317	4
832	20	100	803	70	254	442.54	2.44	-7	337	334	32.15	24	87	312	4
833	20	100	803	69	243	434.07	2.59	-6	331	319	33.57	26	85	309	3
834	20	100	803	69	229	430.72	2.77	-5	330	300	35.62	27	85	308	2
835	20	100	803	67	215	421.61	3.02	-4	322	282	37.94	29	87	306	2
836	20	100	803	62	213	388.78	3.31	-1	295	281	38.37	29	86	302	1
838	20	100	803	51	230	319.97	3.72	5	243	303	35.52	27	80	276	3
839	20	100	1003	75	230	473.79	2.01	-3	372	293	35.50	28	87	311	3
871	0	100	802	73	287	455.64	1.47	-7	347	377	28.52	22	94	294	5
872	0	100	802	68	284	427.58	1.57	-9	322	378	28.75	22	93	293	5
873	0	100	802	66	266	413.81	1.74	-8	311	354	30.69	23	91	291	4
874	0	100	802	63	252	397.32	1.93	-8	297	336	32.48	24	89	291	4
875	0	100	802	62	224	390.44	2.22	-7	292	299	36.51	27	89	290	3

continued on next page...

Test ref. (-)	RON (-)	T_{Int} (C)	N (RPM)	IT (Nm)	ISFC (g/kWh)	IMEP (kPA)	λ (-)	CA50 (aTDC)	BMEP (kPA)	BSFC (g/kWh)	$\eta_{I,th}$ (%)	$\eta_{b,th}$ (%)	η_{comb} (%)	T_{ex} (°C)	COV (%)
876	0	100	802	54	233	336.03	2.51	-3	246	318	35.11	26	86	290	2
877	0	100	802	50	225	316.69	2.77	-1	231	308	36.30	26	87	283	3
878	0	100	802	45	230	280.16	3.10	1	204	316	35.56	26	86	266	4
879	0	100	1003	66	267	417.41	1.73	-7	316	353	30.64	23	96	298	5
7810	40	100	1002	78	212	487.43	1.92	10	402	257	38.53	32	77	343	2
7812	40	100	1203	91	218	572.19	1.60	7	470	266	37.43	31	72	373	2
7813	40	100	1203	88	211	553.59	1.72	7	453	258	38.66	32	74	370	1
7814	40	100	1203	85	207	531.29	1.84	9	437	252	39.40	32	78	374	1
7815	40	100	1203	83	207	520.64	1.88	11	431	251	39.42	33	80	376	1
7816	40	100	1203	77	217	485.71	1.92	16	415	255	37.57	32	76	378	6
7817	40	100	1406	94	213	587.61	1.62	9	479	261	38.44	31	76	406	2

A.2 HCCI

Table A.6
Steady State Tests-Optimized at naturally aspirated conditions

Test ref. (-)	RON (-)	T_{Int} (C)	N (RPM)	IT (Nm)	ISFC (g/kWh)	IMEP (kPA)	λ (-)	CA50 (aTDC)	BMEP (kPA)	BSFC (g/kWh)	$\eta_{I,th}$ (%)	$\eta_{b,th}$ (%)	η_{comb} (%)	T_{ex} (°C)	COV (%)
2	0	40	800	60	216	379.03	2.66	5	354	227	37.40	56	82	192	2
31	20	40	1200	93	207	584.19	1.86	10	559	213	39.15	89	87	357	1
35	20	40	1400	99	207	622.60	1.79	12	591	216	39.06	94	87	402	1
36	40	40	800	86	206	541.81	2.06	10	521	210	39.20	83	85	325	1
37	40	40	800	90	212	565.73	1.89	4	557	211	38.15	89	82	360	1
44	40	40	1000	87	203	550.10	2.04	11	527	209	39.80	84	88	391	1
54	0	60	1000	60	217	377.04	2.49	1	352	229	37.21	56	84	280	1
65	0	60	1400	71	210	448.96	2.29	7	412	227	38.46	66	87	326	2
68	0	60	1600	74	209	463.47	2.21	10	415	232	38.68	66	89	342	2
69	0	60	1600	78	210	489.47	2.06	7	447	228	38.54	71	88	354	2
70	20	60	800	66	216	413.86	2.48	8	388	227	37.44	62	83	281	2
71	20	60	800	72	211	454.44	2.29	3	436	216	38.29	69	84	304	1
81	20	60	1200	88	204	551.95	2.13	8	526	212	39.70	84	88	368	1
85	20	60	1400	90	206	566.38	1.99	13	528	219	39.30	84	89	383	2
89	40	60	800	83	206	523.07	2.10	8	504	210	39.28	80	85	342	1
94	40	60	1000	91	203	572.38	2.09	7	556	206	39.96	88	87	377	1
97	40	60	1200	95	208	597.39	1.85	16	564	218	38.96	90	89	418	2
98	40	60	1200	101	222	633.68	1.60	5	624	223	36.51	99	79	337	3
99	40	60	1200	98	208	617.46	1.79	10	594	214	38.98	94	87	414	1
101	0	80	800	54	222	342.03	1.01	0	319	234	36.33	51	82	258	1
106	0	80	1000	45	253	284.20	2.87	8	253	279	31.93	40	74	254	9
107	0	80	1000	55	221	343.91	2.73	5	315	238	36.53	50	83	275	2
111	0	80	1200	54	229	339.06	2.70	9	304	253	35.24	48	83	296	6
112	0	80	1200	61	214	383.14	2.53	6	350	231	37.81	56	87	306	2
113	0	80	1200	64	213	403.01	2.41	3	373	228	37.85	59	86	315	1
117	0	80	1400	68	211	426.61	2.36	4	391	229	38.23	62	87	332	2
121	0	80	1600	72	209	450.68	2.21	6	406	231	38.61	65	89	357	2
124	20	80	800	63	217	397.45	2.55	5	373	227	37.33	59	82	298	1
133	20	80	1200	76	207	475.60	2.39	11	443	220	39.07	70	88	361	1
134	20	80	1200	81	206	506.38	2.12	7	480	214	39.30	76	88	377	1
136	20	80	1400	84	205	528.83	2.05	9	494	217	39.48	79	89	397	1
139	20	80	1600	90	205	568.35	2.03	11	525	221	39.43	83	89	434	1
140	20	80	1600	87	204	549.79	2.16	14	502	223	39.54	80	91	437	2
141	40	80	800	77	208	485.90	2.24	7	465	213	38.85	74	84	315	1
143	40	80	800	82	210	513.23	2.03	3	500	212	38.55	80	83	344	1
147	40	80	1000	80	204	500.83	2.34	10	475	212	39.72	76	88	372	1
148	40	80	1000	84	204	529.00	2.19	6	511	208	39.73	81	87	379	1

continued on next page...

Test ref. (-)	RON (-)	T_{Int} (C)	N (RPM)	IT (Nm)	ISFC (g/kWh)	IMEP (kPA)	λ (-)	CA50 (aTDC)	BMEP (kPA)	BSFC (g/kWh)	$\eta_{I,th}$ (%)	$\eta_{b,th}$ (%)	η_{comb} (%)	T_{ex} (°C)	COV (%)
154	40	80	1200	91	204	569.44	2.07	13	539	213	39.75	86	89	428	1
155	0	100	800	39	253	248.13	3.11	0	221	280	31.92	35	74	240	4
156	0	100	800	46	235	288.64	2.90	-3	264	252	34.41	42	79	258	1
157	0	100	800	50	234	314.59	2.68	-5	292	247	34.54	46	79	271	1
162	0	100	1000	42	245	266.09	2.99	4	236	273	32.93	37	77	247	5
163	0	100	1000	51	225	319.53	2.75	1	292	243	35.89	46	82	269	1
167	0	100	1200	50	230	313.12	2.81	6	278	256	35.18	44	83	289	4
172	0	100	1400	54	223	341.74	2.71	7	300	252	36.30	48	90	303	4
173	0	100	1400	62	212	386.88	2.48	3	350	232	38.18	56	92	318	1
174	0	100	1400	64	213	403.65	2.36	1	370	231	37.91	59	92	327	2
175	0	100	1600	62	210	390.71	2.43	7	342	238	38.56	54	95	338	2
176	0	100	1600	65	210	409.91	2.34	5	363	235	38.50	58	94	344	1
184	20	100	1000	64	213	403.37	2.46	4	378	225	37.89	60	87	316	1
185	20	100	1000	69	212	433.93	2.25	2	413	219	38.20	66	88	328	1
188	20	100	1200	68	211	427.25	2.40	9	394	227	38.30	63	90	334	2
189	20	100	1200	72	207	454.80	2.28	6	426	220	38.99	68	91	349	1
192	20	100	1400	75	207	470.52	2.40	11	431	225	38.98	68	92	355	1
193	20	100	1400	79	206	497.24	2.13	7	464	220	39.21	74	91	380	1
195	20	100	1600	82	206	517.29	2.21	12	469	226	39.21	75	93	395	1
196	20	100	1600	85	205	532.33	2.06	10	488	222	39.44	78	93	419	1
199	40	100	800	69	210	435.32	2.36	5	414	217	38.54	66	87	317	1
203	40	100	1000	67	211	420.96	2.62	12	391	225	38.30	62	89	341	3
204	40	100	1000	72	207	453.08	2.48	9	425	218	39.07	68	89	313	1
205	40	100	1000	76	206	476.40	2.37	5	454	213	39.36	72	89	349	1
208	40	100	1200	84	204	527.27	2.20	12	496	215	39.60	79	92	386	1

Table A.7
Steady State Tests-Optimized at Boosted conditions

RON (-)	T_{Int} (C)	N (RPM)	IT (Nm)	ISFC (g/kWh)	IMEP (kPA)	λ (-)	CA50 (aTDC)	BMEP (kPA)	BSFC (g/kWh)	$\eta_{I,th}$ (%)	$\eta_{b,th}$ (%)	η_{comb} (%)	T_{ex} (°C)	COV (%)
0	58	1000	54	320	338.22	3.55	4	312	347	30.31	25	70	163	6
0	80	1000	66	238	414.63	3.83	-1	394	249	40.92	33	99	160	3
0	59	1000	73	259	458.30	3.29	1	441	268	37.61	34	84	215	2
0	80	1000	74	232	468.03	3.47	-3	457	237	41.94	35	100	169	2
0	80	1000	79	239	495.30	3.22	-5	490	241	40.64	34	98	182	2
20	80	1000	83	219	519.15	3.49	2	506	224	44.51	34	105	186	1
10	80	1000	87	231	544.46	3.17	-2	540	232	42.13	35	99	197	1
20	61	1000	91	218	574.52	3.20	2	569	220	44.59	34	103	271	1
40	80	1000	97	211	612.03	3.22	3	608	213	45.97	32	106	220	1
40	60	1000	104	222	653.03	2.90	3	652	221	44.03	31	101	226	1
0	79	1200	43	307	269.16	3.86	4	236	347	26.56	19	66	176	5
0	77	1200	59	246	370.33	3.46	2	342	264	33.18	26	79	208	5
0	41	1200	70	243	437.26	3.16	6	408	258	33.62	28	86	225	6
0	79	1200	74	210	465.22	3.27	0	445	218	38.83	32	91	233	2
20	84	1200	79	204	495.61	3.29	6	471	212	40.04	28	95	270	2
20	81	1200	85	200	533.90	3.13	4	516	205	40.79	29	95	287	1
20	79	1200	91	199	572.26	2.95	1	563	200	41.16	31	96	294	1
20	60	1200	95	198	594.87	2.94	4	583	200	41.27	30	94	298	1
40	79	1200	100	196	626.68	2.90	7	612	199	41.69	28	96	309	1
40	60	1200	103	197	649.51	2.87	7	637	199	41.53	29	90	326	1
40	60	1200	110	197	690.60	2.61	4	689	196	41.48	30	93	331	1
40	43	1200	116	195	727.75	2.86	10	717	196	41.93	20	102	344	1
40	43	1200	120	196	753.98	2.74	8	750	195	41.74	21	101	348	1
0	80	1400	50	241	314.23	3.37	6	274	275	28.96	22	71	223	7
0	80	1400	64	198	404.83	3.25	5	368	216	35.30	28	84	242	5
0	80	1400	74	179	465.80	3.14	3	436	190	38.88	32	91	267	2
0	81	1400	79	179	495.28	2.98	0	473	186	39.00	33	91	279	2
0	40	1400	86	179	537.88	2.59	7	506	189	38.90	33	97	293	2
20	80	1400	88	170	552.59	2.96	9	522	179	40.94	28	95	319	1
20	80	1400	93	170	584.08	2.79	5	563	175	41.11	31	94	324	1
40	79	1400	99	173	619.73	2.91	14	584	182	40.41	19	96	353	3
20	60	1400	100	172	627.85	2.71	8	606	177	40.69	29	93	332	1
40	79	1400	107	168	670.26	2.75	10	647	173	41.52	19	96	361	1
20	43	1400	111	174	699.58	2.30	6	688	176	40.05	32	97	354	2
40	60	1400	115	172	723.75	2.37	8	712	174	40.52	29	91	361	2
40	40	1400	120	176	754.28	2.46	16	721	183	39.76	20	100	382	4
40	40	1400	125	173	783.56	2.41	13	762	177	40.44	20	99	378	1

continued on next page...

RON (-)	T_{Int} (C)	N (RPM)	IT (Nm)	ISFC (g/kWh)	IMEP (kPA)	λ (-)	CA50 (aTDC)	BMEP (kPA)	BSFC (g/kWh)	$\eta_{I,th}$ (%)	$\eta_{b,th}$ (%)	η_{comb} (%)	T_{ex} (°C)	COV (%)
0	79	1600	60	184	379.62	3.18	7	331	210	33.10	25	80	256	8
0	80	1600	74	157	464.60	3.08	6	421	172	38.78	31	92	278	3
0	80	1600	79	153	496.39	2.97	3	460	165	39.73	33	93	292	2
0	80	1600	82	153	517.32	2.85	1	488	162	39.77	33	93	300	2
20	79	1600	88	152	550.39	3.11	12	505	165	40.17	18	95	338	4
0	42	1600	93	154	583.90	2.60	7	550	162	39.58	34	101	301	2
20	79	1600	94	148	594.27	2.98	9	557	157	41.23	19	96	343	1
20	79	1600	98	149	617.62	2.56	6	589	156	40.83	30	94	352	1
20	43	1600	105	154	657.97	2.60	16	613	165	39.51	19	101	373	4
40	79	1600	108	148	679.08	2.74	13	640	156	41.29	19	98	384	1
40	79	1600	112	147	705.94	2.64	12	674	153	41.64	19	98	375	1
20	43	1600	115	151	723.47	2.37	8	703	155	40.24	20	99	368	1
0	78	1800	74	142	465.34	3.02	8	409	161	38.19	31	91	293	5
0	77	1800	84	135	528.22	2.79	6	479	149	39.98	34	94	312	2
0	79	1800	87	136	546.15	2.65	1	509	145	39.79	34	93	316	2
0	59	1800	90	136	568.19	2.66	8	519	148	39.90	33	93	308	2
0	60	1800	93	136	587.07	2.54	5	547	145	39.80	34	92	316	2
0	43	1800	97	135	610.02	2.46	8	567	145	39.96	35	102	323	2
20	79	1800	99	132	623.11	2.87	11	575	143	40.92	19	96	367	2
20	79	1800	102	132	643.96	2.71	7	604	140	40.92	21	95	369	1
20	80	1800	105	135	661.49	2.34	8	623	142	40.21	31	93	347	1
20	60	1800	112	134	705.28	2.22	11	660	143	40.38	30	93	346	2
20	44	1800	117	136	736.71	2.45	16	685	146	39.85	17	101	405	2
20	44	1800	122	135	765.38	2.39	12	727	141	40.29	19	101	406	1
0	44	1900	88	132	550.99	2.67	10	489	149	38.70	31	99	323	4
0	44	1900	94	128	591.09	2.81	9	537	140	40.07	19	103	324	2
0	45	1900	98	127	614.83	2.59	5	570	137	40.28	27	103	333	2
0	45	1900	102	128	640.02	2.33	4	602	135	40.04	35	101	339	2
0	77	2000	72	130	455.54	3.06	9	385	154	37.38	25	91	301	7
0	77	2000	86	119	539.89	2.78	6	482	133	40.86	34	90	326	2
0	59	2000	89	120	560.77	2.73	8	498	135	40.55	33	96	325	2
0	60	2000	94	120	591.06	2.57	6	536	132	40.63	34	95	333	2
0	45	2000	98	120	618.34	2.54	6	568	130	40.51	27	106	340	2
20	79	2000	106	117	665.27	2.59	7	616	126	41.74	22	97	378	1
0	75	2200	77	116	482.48	2.90	11	397	141	37.99	30	88	329	6
0	75	2200	87	108	547.05	2.72	7	473	125	40.77	34	93	339	2
0	75	2200	92	107	577.23	2.57	4	511	121	41.13	34	94	348	1
0	74	2400	79	108	496.48	2.88	13	392	136	37.58	23	88	345	7
0	74	2400	89	99	559.01	2.62	10	465	119	40.73	33	93	357	3

A.3 RCCI

Table A.8
Steady State Tests-Boosted-Optimized

Test ref. (-)	PR (-)	T_{Int} (C)	N (RPM)	MAP (kPa)	IT (Nm)	ISFC (g/kWh)	IMEP (kPA)	λ (-)	SOI (bTDC)	CA50 (aTDC)	BMEP (kPA)	BSFC (g/kWh)	$\eta_{I,th}$ (%)	$\eta_{b,th}$ (%)	η_{comb} (%)	T_{ex} ($^{\circ}$C)	COV (%)
86	60	39	1392	117	176	196	1106	2.12	56.00	8	923	234	41.82	147	88	460	2
31	20	40	1592	118	159	253	998	1.15	52.00	7	834	302	32.35	133	78	597	4
20	20	80	1393	118	53	215	335	3.91	32.00	6	259	278	38.07	41	92	255	4
22	20	80	1392	118	86	239	544	2.04	32.00	9	446	290	34.28	71	85	389	6
168	40	60	1796	119	117	195	738	2.01	54.00	8	601	240	41.86	96	98	456	3
164	40	60	1595	119	114	200	719	2.04	48.00	8	588	245	40.79	94	96	449	4
23	20	40	1392	119	79	185	500	3.07	44.00	9	400	230	44.31	64	101	307	4
165	40	60	1593	119	140	212	882	1.58	48.00	8	736	254	38.48	117	91	532	3
22	20	40	1393	119	69	192	432	3.45	44.00	11	353	234	42.64	56	98	288	9
158	40	60	1394	119	93	203	586	2.44	39.00	9	479	248	40.31	76	95	364	5
191	60	60	1594	119	135	212	848	1.75	55.00	11	718	251	38.50	114	89	526	5
159	40	60	1393	119	111	208	698	1.99	39.00	8	573	252	39.39	91	93	433	3
127	60	80	1599	119	80	230	501	2.87	47.00	4	389	296	35.51	62	88	375	8
129	60	80	1598	119	141	219	887	1.51	47.00	7	740	263	37.28	118	91	530	2
187	60	60	1393	119	122	206	768	2.01	50.00	7	637	249	39.61	101	90	460	4
87	40	80	1596	119	106	205	669	1.97	40.00	7	544	251	39.98	87	NaN	469	5
133	60	80	1798	119	143	216	900	1.50	53.00	5	743	262	37.82	118	93	558	2
111	20	60	1796	119	56	221	353	3.97	44.00	8	268	290	37.05	43	86	319	8
85	40	80	1594	119	90	204	566	2.32	40.00	6	450	256	40.16	72	NaN	420	10
108	20	60	1593	119	101	215	637	2.11	42.00	7	514	266	38.02	82	90	410	3
25	20	40	1393	119	137	225	863	1.47	44.00	7	713	273	36.28	113	86	505	4
90	40	80	1793	119	105	207	663	1.97	47.00	5	530	258	39.60	84	NaN	482	8
130	60	80	1599	119	153	240	961	1.26	47.00	7	802	287	34.08	128	83	584	1
134	60	80	1800	119	152	234	955	1.32	53.00	5	789	283	34.94	126	87	603	1
80	40	80	1392	120	100	218	627	1.98	34.00	7	510	268	37.43	81	NaN	439	6
34	20	40	1795	120	114	202	714	2.02	55.00	7	574	251	40.51	91	94	426	3
6	20	80	787	120	96	214	606	2.03	16.00	6	495	262	38.23	79	90	345	4
105	20	60	1596	120	51	238	318	4.28	42.00	5	234	323	34.36	37	80	288	7
79	40	80	1392	120	84	205	527	2.50	34.00	6	418	259	39.86	66	NaN	399	8
35	20	40	1795	120	139	222	877	1.49	55.00	8	724	268	36.87	115	88	549	4
123	60	80	1397	120	73	267	459	2.76	36.00	8	368	333	30.64	59	78	353	7
58	40	40	1394	120	126	191	791	2.12	52.00	10	657	230	42.74	105	98	425	4
71	40	80	986	120	98	221	619	1.99	26.00	5	501	273	36.99	80	NaN	375	7
2	20	40	788	120	60	211	375	3.72	16.00	7	295	268	38.69	47	87	209	8
59	40	40	1393	120	146	196	920	1.81	52.00	5	756	238	41.78	120	94	495	2
63	20	80	3013	120	124	324	778	1.11	75.00	17	666	379	25.22	106	NaN	754	6
172	40	60	1999	120	122	188	767	2.01	62.00	5	613	235	43.50	98	96	467	5
14	20	79	1189	120	44	220	278	4.44	26.00	5	210	291	37.10	33	91	235	3
15	20	80	1189	120	53	217	332	4.07	26.00	6	256	281	37.67	41	91	242	4
125	60	80	1398	120	133	232	838	1.50	36.00	10	712	273	35.20	113	88	517	3
35	20	80	1793	120	146	275	918	1.11	47.00	7	767	329	29.76	122	75	612	4
2	20	81	787	120	103	222	649	1.83	16.00	6	532	271	36.80	85	87	377	3
137	60	79	2001	120	138	225	865	1.53	53.00	8	722	269	36.36	115	87	575	3
36	20	79	1993	120	51	213	322	4.36	47.00	4	228	300	38.47	36	90	314	4
136	60	80	1999	120	104	232	653	2.01	53.00	7	524	288	35.29	83	85	454	5
31	20	80	1794	120	51	213	321	4.55	47.00	3	225	304	38.38	36	92	243	4
66	40	80	790	120	83	264	519	2.18	15.00	6	419	326	31.01	67	NaN	338	8
7	20	80	786	120	119	250	749	1.46	16.00	7	623	301	32.67	99	76	407	3
7	20	40	988	120	46	214	286	5.51	23.00	9	229	267	38.22	36	87	208	4
94	40	80	2001	121	107	277	676	1.56	48.00	11	557	336	29.50	89	NaN	545	7
9	20	40	989	121	62	203	391	3.80	26.00	8	309	256	40.29	49	90	233	8

continued on next page...

Test ref. (-)	PR (-)	T_{Int} (C)	N (RPM)	MAP (kPa)	IT (Nm)	ISFC (g/kWh)	IMEP (kPA)	λ (-)	SOI (bTDC)	CA50 (aTDC)	BMEP (kPA)	BSFC (g/kWh)	$\eta_{I,th}$ (%)	$\eta_{b,th}$ (%)	η_{comb} (%)	T_{ex} (°C)	COV (%)
117	20	60	1997	121	74	193	467	3.18	47.00	10	368	244	42.37	59	96	359	5
138	60	80	1999	121	151	243	950	1.28	53.00	9	801	288	33.68	127	81	649	2
144	60	80	2407	121	101	238	635	2.05	62.00	11	523	289	34.29	83	83	514	7
10	20	40	988	121	80	201	501	2.90	26.00	8	401	251	40.58	64	92	271	3
93	40	80	1997	121	83	249	521	2.15	48.00	8	410	316	32.88	65	NaN	431	8
119	20	60	1997	121	98	228	616	2.06	47.00	11	502	279	35.86	80	84	480	3
118	20	60	1994	121	86	207	539	2.55	47.00	10	431	259	39.46	69	91	405	4
39	20	40	1996	121	115	200	721	2.07	60.00	8	578	249	40.89	92	91	451	4
12	20	40	987	121	129	249	809	1.49	26.00	8	674	299	32.80	107	74	443	3
11	20	40	988	121	102	226	638	2.06	26.00	8	522	276	36.22	83	83	359	4
78	40	80	1188	121	147	297	923	1.05	28.00	9	782	350	27.58	124	NaN	537	2
38	20	40	1994	121	82	181	518	3.18	60.00	9	406	230	45.22	65	99	351	5
37	20	40	1994	121	75	183	472	3.33	60.00	11	375	230	44.62	60	98	351	8
51	20	80	2606	121	52	219	329	4.15	60.00	9	252	286	37.31	40	NaN	322	6
68	60	40	789	121	132	190	832	2.12	24.00	4	684	232	42.93	109	95	337	3
95	20	60	1190	121	75	204	473	2.96	28.00	7	374	258	40.09	59	93	309	2
69	60	40	787	121	141	195	885	1.93	24.00	1	722	239	41.85	115	92	377	2
59	20	80	2807	121	121	332	760	1.13	71.00	16	648	389	24.65	103	NaN	708	6
62	20	80	3005	121	116	248	728	1.46	75.00	9	587	307	33.03	93	NaN	620	6
96	20	60	1190	121	97	237	607	1.99	28.00	8	496	290	34.46	79	81	387	4
70	60	40	787	121	154	223	968	1.52	24.00	0	792	273	36.63	126	81	407	1
41	20	79	2204	121	52	211	324	4.49	51.00	6	236	290	38.75	37	89	281	4
47	20	79	2401	121	74	202	464	2.85	53.00	10	368	255	40.50	58	NaN	374	8
97	20	60	1190	121	123	262	771	1.42	28.00	9	645	313	31.23	103	73	490	4
44	20	81	2196	122	116	248	728	1.49	51.00	10	598	301	33.04	95	NaN	592	6
73	60	40	988	122	124	204	777	2.08	31.00	11	658	241	40.07	105	92	390	6
50	40	40	988	122	107	225	673	2.02	26.00	10	557	271	36.34	89	84	365	4
142	60	80	2201	122	142	250	895	1.33	55.00	15	769	290	32.75	122	79	691	3
134	20	60	2599	122	114	252	714	1.53	63.00	17	611	294	32.41	97	80	651	5
133	20	60	2599	122	99	220	623	1.99	63.00	15	526	260	37.22	84	89	522	4
74	60	40	988	122	144	191	906	1.85	31.00	7	762	227	42.86	121	96	431	2
139	60	79	2206	122	84	260	527	2.40	55.00	10	425	322	31.47	68	76	442	8
75	60	40	987	122	152	195	958	1.71	31.00	6	799	234	41.83	127	93	454	2
46	20	80	2398	122	53	218	330	4.19	53.00	8	249	290	37.50	40	NaN	303	6
41	40	40	787	122	51	238	318	4.49	13.00	8	255	296	34.41	41	81	225	8
135	20	60	2607	122	125	274	788	1.26	63.00	17	676	319	29.80	108	74	729	5
98	40	80	2206	122	108	277	676	1.55	53.00	12	560	334	29.51	89	NaN	574	5
125	20	60	2198	122	113	253	712	1.56	53.00	14	596	302	32.30	95	76	607	4
151	40	60	1190	122	63	253	394	3.28	32.00	8	312	318	32.38	50	75	298	6
132	20	60	2600	122	88	196	553	2.46	63.00	13	452	239	41.80	72	97	469	4
153	40	60	1189	122	110	213	694	2.00	32.00	7	569	259	38.41	90	90	408	4
47	40	40	988	122	54	224	338	4.59	23.00	11	279	271	36.53	44	84	237	6
123	20	60	2197	122	87	204	548	2.49	53.00	11	439	254	40.12	70	90	423	4
54	40	40	1188	122	91	190	570	2.90	44.00	9	462	234	43.12	73	97	332	7
129	20	60	2400	122	114	252	714	1.51	57.00	17	612	294	32.42	97	78	641	4
56	20	80	2808	122	70	206	437	2.94	71.00	9	336	268	39.69	53	NaN	366	7
127	20	60	2400	122	86	214	540	2.37	57.00	14	450	256	38.30	72	89	457	4
16	20	40	1190	122	84	191	528	2.94	38.00	7	417	242	42.76	66	97	289	3
52	40	40	986	122	171	269	1072	1.07	26.00	8	907	317	30.42	144	68	523	1
58	20	80	2805	122	110	261	690	1.49	71.00	10	557	323	31.31	89	NaN	586	5
78	60	40	1189	122	119	212	748	2.25	40.00	14	644	246	38.60	102	90	441	8
55	40	40	1189	122	120	191	755	2.10	44.00	7	616	234	42.82	98	97	385	3
79	60	40	1190	122	143	193	897	2.04	40.00	12	764	226	42.40	122	98	461	4
80	60	40	1189	122	156	191	980	1.87	40.00	9	828	226	42.78	132	97	482	2
17	20	40	1189	122	109	210	685	2.06	38.00	6	553	260	38.87	88	89	358	3
81	60	40	1189	122	163	197	1022	1.75	40.00	8	862	234	41.43	137	94	501	2

continued on next page...

Test ref. (-)	PR (-)	T_{Int} (C)	N (RPM)	MAP (kPa)	IT (Nm)	ISFC (g/kWh)	IMEP (kPA)	λ (-)	SOI (bTDC)	CA50 (aTDC)	BMEP (kPA)	BSFC (g/kWh)	$\eta_{I,th}$ (%)	$\eta_{b,th}$ (%)	η_{comb} (%)	T_{ex} (°C)	COV (%)
83	60	40	1188	122	174	198	1094	2.15	47.00	6	913	237	41.39	145	88	410	2
60	20	80	3006	123	74	201	467	2.75	75.00	7	351	267	40.76	56	NaN	403	4
84	60	40	1189	123	183	207	1149	1.96	47.00	2	954	249	39.52	152	84	427	2
118	60	80	991	124	136	252	857	1.42	22.00	5	701	308	32.41	111	75	463	1
1	20	80	787	126	106	216	668	1.92	16.00	7	547	263	37.92	87	89	362	3
102	20	60	987	135	87	231	546	2.92	19.00	9	433	291	35.43	69	82	359	3
29	20	39	1590	138	192	239	1207	1.18	50.00	8	1024	281	34.24	163	82	590	4
126	20	60	1796	138	49	198	309	6.73	48.00	8	213	287	41.28	34	96	230	3
54	60	60	1191	138	131	219	822	2.01	25.00	13	693	260	37.30	110	91	432	6
129	20	60	1795	139	97	194	612	2.96	48.00	8	476	249	42.12	76	98	326	3
122	20	60	1594	139	98	200	613	2.91	42.00	8	479	255	40.94	76	95	311	3
123	20	60	1591	139	126	218	795	2.02	42.00	9	647	267	37.59	103	89	408	4
84	40	80	2808	139	98	234	615	2.05	62.00	11	487	296	34.90	77	86	474	9
119	20	60	1593	139	48	202	303	6.62	42.00	7	206	297	40.44	33	95	219	3
53	40	80	1599	139	58	239	362	3.54	40.00	5	257	337	34.27	41	86	261	6
54	40	80	1598	139	65	246	410	2.99	40.00	5	299	337	33.21	48	84	263	7
114	20	60	1392	139	65	195	407	4.69	34.00	9	304	260	42.00	48	98	251	7
57	60	60	1394	139	142	202	893	1.99	36.00	10	748	241	40.53	119	99	454	5
92	20	80	1795	139	121	209	759	1.98	47.00	3	604	262	39.16	96	97	448	5
160	20	63	3004	139	103	201	646	2.45	73.00	11	509	255	40.71	81	94	438	5
82	40	80	2605	139	123	270	775	1.55	60.00	11	632	331	30.31	100	78	597	5
26	40	60	1800	139	82	223	517	2.86	40.00	10	395	292	36.68	63	96	362	7
159	20	63	3004	139	95	192	599	2.76	73.00	11	467	246	42.50	74	96	409	5
58	60	60	1394	139	152	200	957	1.85	36.00	10	809	236	40.99	129	99	483	6
27	40	60	1797	139	93	235	583	2.42	40.00	11	458	299	34.83	73	93	405	7
52	60	60	989	139	165	222	1037	1.59	17.00	10	879	262	36.76	140	84	471	2
12	40	60	1190	139	89	231	562	2.52	26.00	7	433	299	35.41	69	92	346	5
59	40	80	1799	139	65	248	406	3.08	45.00	6	294	343	32.94	47	83	269	8
107	60	80	1596	139	157	227	986	1.62	44.00	8	831	269	36.09	132	86	496	2
97	20	80	1996	139	117	216	733	2.00	52.00	2	574	276	37.82	91	91	458	7
100	20	60	987	139	57	211	358	4.84	19.00	8	266	284	38.72	42	91	235	6
58	40	80	1798	139	59	231	374	3.59	45.00	5	262	330	35.35	42	88	273	5
101	20	60	987	139	71	208	443	3.77	19.00	8	340	271	39.31	54	92	280	3
28	40	60	1795	139	105	251	660	2.10	40.00	13	532	311	32.54	85	87	457	7
134	20	60	1996	139	59	204	370	4.85	50.00	9	264	286	40.03	42	91	244	8
106	20	59	1189	139	46	211	290	6.07	26.00	8	206	298	38.68	33	92	230	2
7	40	60	989	139	81	256	506	2.58	18.00	8	388	334	31.92	62	83	334	6
82	60	40	1188	139	146	197	915	2.54	47.00	11	767	235	41.54	122	94	386	5
48	60	60	787	139	161	221	1013	1.71	14.00	4	841	265	37.08	134	85	396	2
138	20	60	1994	139	145	269	910	1.42	50.00	11	754	324	30.38	120	72	568	4
98	20	80	1999	140	136	261	854	1.48	52.00	5	692	322	31.27	110	77	568	6
46	60	60	789	140	129	196	810	2.46	14.00	8	677	234	41.77	108	97	322	3
87	20	80	1596	140	119	212	749	1.98	39.00	6	603	263	38.62	96	95	445	4
45	60	60	790	140	94	219	592	3.02	14.00	8	478	271	37.33	76	90	278	6
99	20	60	988	140	44	220	278	6.04	19.00	7	197	311	37.10	31	89	196	2
19	20	41	1392	140	56	211	352	4.45	45.00	12	277	268	38.82	44	91	222	8
113	20	60	1392	140	48	204	300	6.26	34.00	7	207	295	40.02	33	95	222	4
33	20	39	1794	140	178	194	1117	1.54	57.00	5	930	232	42.24	148	98	505	3
31	40	60	2005	140	80	215	503	3.11	45.00	8	373	290	38.03	59	97	349	7
136	20	60	1997	140	95	200	595	2.88	50.00	9	459	259	40.95	73	93	338	3
47	60	60	789	140	147	203	924	2.05	14.00	6	768	244	40.34	122	93	358	3
23	20	42	1391	140	168	219	1055	1.46	47.00	4	877	263	37.42	139	87	478	5
16	20	40	1189	140	136	194	855	1.95	34.00	7	698	237	42.17	111	98	354	3
149	20	60	2400	140	132	200	831	2.02	68.00	6	663	250	40.98	105	92	452	4
148	20	60	2399	140	99	186	621	2.94	68.00	8	477	242	44.08	76	96	347	4
72	40	80	2204	140	101	238	635	2.06	48.00	10	503	301	34.31	80	83	370	8

continued on next page...

Test ref. (-)	PR (-)	T_{Int} (C)	N (RPM)	MAP (kPa)	IT (Nm)	ISFC (g/kWh)	IMEP (kPA)	λ (-)	SOI (bTDC)	CA50 (aTDC)	BMEP (kPA)	BSFC (g/kWh)	$\eta_{I,th}$ (%)	$\eta_{b,th}$ (%)	η_{comb} (%)	T_{ex} (°C)	COV (%)
142	20	60	2201	140	96	190	607	2.97	61.00	7	462	250	43.04	73	94	337	4
104	60	80	1399	140	164	245	1028	1.42	35.00	11	880	286	33.34	140	80	522	2
147	20	60	2404	140	83	180	520	3.50	68.00	9	392	239	45.37	62	99	320	5
140	20	60	2201	140	73	181	459	4.17	61.00	10	344	241	45.30	55	100	288	8
21	40	60	1595	140	84	217	530	2.84	35.00	10	408	283	37.62	65	99	362	4
7	20	80	2408	140	94	208	590	2.47	50.00	9	458	267	39.36	73	96	438	6
42	40	60	2403	140	116	228	727	2.05	57.00	15	599	277	35.86	95	88	501	8
154	20	61	2606	140	138	208	868	1.83	70.00	7	698	258	39.38	111	84	510	5
150	20	60	2401	140	158	217	994	1.57	68.00	6	817	264	37.61	130	86	562	4
17	20	40	1188	140	160	229	1005	1.45	34.00	6	838	275	35.64	133	83	444	4
143	20	60	2197	140	129	204	813	2.02	61.00	6	647	256	40.11	103	90	439	4
17	20	80	2801	140	94	207	591	2.50	58.00	8	453	270	39.45	72	99	482	8
43	40	60	2400	140	141	227	890	1.69	57.00	20	777	259	36.06	124	87	589	8
144	20	60	2198	140	156	250	982	1.40	61.00	8	810	302	32.76	129	76	596	4
152	20	61	2601	140	95	193	597	2.96	70.00	10	461	250	42.34	73	94	357	5
153	20	61	2598	140	117	195	738	2.27	70.00	7	577	249	41.87	92	94	423	3
24	20	42	1391	140	198	260	1248	1.08	47.00	5	1058	306	31.47	168	74	543	3
39	40	60	2208	140	130	273	818	1.54	51.00	14	676	330	29.93	108	76	616	5
74	40	80	2203	140	150	229	944	1.45	48.00	19	816	265	35.72	130	89	591	6
92	20	60	787	140	43	228	268	6.28	15.00	6	188	325	35.83	30	86	179	3
94	20	60	787	140	71	210	445	3.97	15.00	6	337	278	38.86	54	90	256	2
37	40	60	2206	140	94	233	588	2.49	51.00	10	456	300	35.13	73	87	410	7
146	20	60	2401	140	79	181	498	3.71	68.00	10	377	239	45.20	60	99	318	8
1	20	82	2204	141	69	240	436	3.15	47.00	7	318	328	34.12	51	81	345	5
62	20	80	789	141	77	208	486	3.09	13.00	6	377	268	39.38	60	96	279	3
50	40	80	1398	141	105	239	663	1.99	31.00	9	535	296	34.19	85	86	377	6
109	60	80	1795	141	90	261	565	2.62	52.00	5	431	342	31.29	69	76	340	7
10	20	43	989	141	111	238	697	2.03	19.00	10	567	292	34.40	90	80	333	6
158	20	62	2804	141	129	214	808	1.91	71.00	9	647	267	38.22	103	90	519	4
156	20	62	2806	141	102	202	643	2.57	71.00	11	506	256	40.55	81	92	409	5
157	20	62	2800	141	117	205	737	2.19	71.00	8	581	260	39.82	92	92	460	4
22	20	80	3004	141	94	207	593	2.40	63.00	9	455	269	39.56	72	98	471	6
111	60	80	1794	141	165	223	1035	1.58	52.00	4	857	269	36.70	136	88	503	1
3	20	41	788	141	90	188	564	3.12	17.00	4	432	245	43.51	69	99	226	8
13	20	80	2605	141	108	232	682	1.95	55.00	10	543	292	35.19	86	89	575	5
4	20	41	788	141	123	214	774	2.15	17.00	4	624	265	38.20	99	86	297	4
30	20	81	3416	141	105	273	661	1.74	74.00	11	524	343	30.00	83	76	593	8
155	20	62	2800	141	85	208	536	3.01	71.00	14	424	263	39.25	67	89	373	7
68	40	38	1795	141	127	180	799	3.17	64.00	7	634	227	45.34	101	99	71	7
65	40	39	1605	141	160	193	1007	2.18	61.00	3	821	237	42.33	130	94	77	6
64	40	38	1595	141	125	183	785	3.08	61.00	5	619	233	44.57	98	99	104	6
1	20	39	788	141	50	217	315	5.12	17.00	6	224	305	37.62	36	87	171	6
114	60	80	1995	142	156	228	982	1.64	52.00	8	820	272	35.94	130	83	513	4
66	40	39	1594	142	135	187	849	2.54	61.00	3	673	235	43.81	107	97	129	7
23	20	80	3004	142	98	246	614	2.10	63.00	10	480	315	33.19	76	84	531	6
77	60	40	786	142	158	211	992	2.12	15.00	7	831	251	38.82	132	86	392	2
78	60	40	785	142	178	231	1122	1.68	15.00	3	939	276	35.38	149	78	406	2
60	40	40	1391	142	119	193	747	2.68	51.00	9	601	240	42.37	96	96	334	7
47	40	39	988	143	66	227	412	4.09	24.00	10	316	296	35.97	50	83	213	6
27	20	81	3206	143	93	246	587	2.26	72.00	7	444	324	33.29	71	82	472	17
50	40	40	987	143	176	228	1107	1.52	24.00	8	939	268	35.89	149	80	447	3
41	40	40	787	143	65	229	409	3.91	14.00	10	319	293	35.74	51	83	212	3
62	40	40	1390	143	188	213	1184	1.52	51.00	3	991	254	38.38	158	87	493	3
43	40	40	785	143	136	228	853	2.03	14.00	8	708	274	35.84	113	82	345	8
48	40	40	988	143	94	219	592	2.96	24.00	9	469	277	37.31	75	85	267	3
49	40	40	987	143	135	230	846	2.00	24.00	8	699	278	35.56	111	81	357	8

continued on next page...

Test ref. (-)	PR (-)	T_{Int} (C)	N (RPM)	MAP (kPa)	IT (Nm)	ISFC (g/kWh)	IMEP (kPA)	λ (-)	SOI (bTDC)	CA50 (aTDC)	BMEP (kPA)	BSFC (g/kWh)	$\eta_{I,th}$ (%)	$\eta_{b,th}$ (%)	η_{comb} (%)	T_{ex} (°C)	COV (%)
73	60	40	985	143	182	226	1147	1.60	25.00	4	961	270	36.17	153	79	435	2
44	40	40	785	144	169	237	1063	1.57	14.00	7	899	280	34.46	143	78	404	3
58	40	40	1186	144	209	268	1316	1.11	39.00	3	1115	316	30.48	177	70	541	2
72	60	39	987	144	160	201	1003	2.08	25.00	9	849	238	40.67	135	90	370	2
28	20	82	3204	144	127	271	797	1.52	72.00	8	637	339	30.14	101	78	665	7

Appendix B

MSc Publications

B.1 Conference Papers

† A. Solouk, M. Shakiba, **K. Kannan**, H. Solmaz, M. Bidarvatan, N. T. Kondipati, P. Dice, M. Shahbakhti, "Fuel Economy Benefits of Integrating a Multi-Mode Low Temperature Combustion (LTC) Engine in a Series Extended Range Electric Powertrain", SAE 2016 International Powertrains, Fuels and Lubricants Meeting, Baltimore, Maryland, USA, Paper No. 16FFL-0277, 13 pages, 2016. (Accepted for publication in June 2016)

The following paper was automatically selected by IRCESM 2015 conference for journal publication.

† S. Polat, **K. Kannan**, M. Shahbakhti, A. Uyumaz, "An experimental study for the effects of supercharging on performance and combustion of an early direct injection HCCI engine", International Journal of Advanced Research in Engineering Vol 1 (1) Apr-Jun 2015.

B.2 Journal Paper

† B. Bahri , M. Shahbakhti, **K. Kannan**, A. A. Aziz, "Identification of Ringing operation for Low Temperature Combustion engine", Applied Energy, 171:142-152, 2016.

Appendix C

Program and Data File Summary

The following lists describe the data files and the post processing code that is used for experiments used for this thesis.

Table C.1
Experimental data files

File Name	File Description
HCCI_NA.mat	340 data points for HCCI naturally aspirated tests for all intake temperatures, RON and engine speed
HCCI_boosted.mat	435 data points for HCCI boosted tests for all intake temperatures, RON and engine speed
PPCI_NA.mat	387 data points for PPCI Naturally aspirated tests for all intake temperatures, RON and engine speed
RCCI_NA.mat	453 data points for RCCI Naturally aspirated tests for all intake temperatures, RON and engine speed
RCCI_boosted.mat	453 data points for RCCI boosted tests for all intake temperatures, RON and engine speed

Table C.2
Experimental data files organized in excel

File Name	File Description
Combined data for HCCI naturally aspirated.xlsx	Data points for HCCI naturally aspirated tests for all intake temperatures, RON and engine speed
HCCI_boosted_optimized sheet.xlsx	Data points for HCCI boosted tests for all intake temperatures, RON and engine speed
Test_Summary_PPCI.xlsx	Data points for PPCI Naturally aspirated tests for all intake temperatures, RON and engine speed
LTC Engine-PCCI Mode-All Experiments.xlsx	Test number and operating conditions for all PPCI tests summarized
RCCI_NA_Optimized_All.xlsx	Data points for RCCI Naturally aspirated tests for all intake temperatures, RON and engine speed
RCCI boosted_all tests with BSFC paramterized.xlsx	Data points for RCCI boosted tests for all intake temperatures, RON and engine speed
RCCI data points effect.xlsx	Data points for the parametric study on RCCI combustion
HCCI data points effect.xlsx	Data points for the parametric study on HCCI combustion

Table C.3
Origin Project files

File Name	File Description
HCCI all tests_1-27-2015.opj	All plots and data for all HCCI tests (naturally aspirated+Boosted)
LTC PPCI maps.opj	All plots and data for PPCI tests
RCCI_NA_COV10.opj	All plots and data for all RCCI tests (naturally aspirated+Boosted)

Table C.4
DSPACE Raw Data for all experiments

Folder Name	File Description
dspace_exp5	335 Data files for HCCI steady state tests (naturally aspirated)
dspace_exp7	213 Data files for HCCI tests (naturally aspirated)
dspace_exp9	229 Data files for HCCI tests (Boosted)
dspace_exp10	107 Data files for HCCI tests (Boosted)
dspace_exp14	39 Data files for HCCI tests (Boosted)
dspace_exp19	184 Data files for RCCI tests (naturally aspirated)
dspace_exp21	191 Data files for RCCI tests (Boosted)
dspace_exp21	191 Data files for RCCI tests (Boosted)
dspace_exp22	160 Data files for RCCI tests (Boosted)
dspace_exp23	144 Data files for RCCI tests (Boosted)
dspace_exp24	99 Data files for RCCI tests (Boosted)
dspace_exp25	114 Data files for HCCI tests (Boosted)
PPCI_All_DSPACE files (77-test dspace to 106-test dspace)	625 Data files for PPCI tests (naturally aspirated)

Table C.5
Labview Raw Data for all experiments

Folder Name	File Description
labview_exp5	335 Data files for HCCI steady state tests (naturally aspirated)
labview_exp7	213 Data files for HCCI tests (naturally aspirated)
labview_exp9	229 Data files for HCCI tests (Boosted)
labview_exp10	107 Data files for HCCI tests (Boosted)
labview_exp14	39 Data files for HCCI tests (Boosted)
labview_exp19	184 Data files for RCCI tests (naturally aspirated)
labview_exp21	191 Data files for RCCI tests (Boosted)
labview_exp21	191 Data files for RCCI tests (Boosted)
labview_exp22	160 Data files for RCCI tests (Boosted)
labview_exp23	144 Data files for RCCI tests (Boosted)
labview_exp24	99 Data files for RCCI tests (Boosted)
labview_exp25	114 Data files for HCCI tests (Boosted)
PPCI_All_labview files (77-test labview to 106-test labview)	625 Data files for PPCI tests (naturally aspirated)

Table C.6
ACAP Raw Data for all experiments

Folder Name	File Description
ACAP_exp5	335 Data files for HCCI steady state tests (naturally aspirated)
ACAP_exp7	213 Data files for HCCI tests (naturally aspirated)
ACAP_exp9	229 Data files for HCCI tests (Boosted)
ACAP_exp10	107 Data files for HCCI tests (Boosted)
ACAP_exp14	39 Data files for HCCI tests (Boosted)
ACAP_exp19	184 Data files for RCCI tests (naturally aspirated)
ACAP_exp21	191 Data files for RCCI tests (Boosted)
ACAP_exp21	191 Data files for RCCI tests (Boosted)
ACAP_exp22	160 Data files for RCCI tests (Boosted)
ACAP_exp23	144 Data files for RCCI tests (Boosted)
ACAP_exp24	99 Data files for RCCI tests (Boosted)
ACAP_exp25	114 Data files for HCCI tests (Boosted)
PPCI_All_ACAP files (77-test ACAP to 106-test ACAP)	625 Data files for PPCI tests (naturally aspirated)

Table C.7
Matlab Scripts for post processing the data

File Name	File Description
Engine_data_analysis_steadystate.m	Updated post processing script used for data analysis for all three combustion regimes

Table C.8
Figure files included in this thesis

File Name	File Description
LTC.png	Figure 1.1
Fig1.png	Figure 1.2
ThesisOrganization.png	Figure 1.3
ExperimentalTestSetup_12-9-2015.png	Figure 2.1
experimental_setup.png	Figure 2.2
portfuelinjectorassembly.png	Figure 2.3
TriggeredSubsystem_PFI_control.png	Figure 2.4
Monitoring_panel_PFi_dspace.png	Figure 2.5
verification_DI_injectors.png	Figure 2.6
calibration_PFI_IsoOctane.png	Figure 2.7
Verification_PFI_IsoOctane.png	Figure 2.7
calibration_PFI_nHeptane.png	Figure 2.8
Verification_PFI_nHeptane.png	Figure 2.8
supercharger_Test_VFD_schematic.png	Figure 2.9
supercharger_frequencyMap24-5IVO.png	Figure 2.10
supercharger_frequencyMap25-5IVO.png	Figure 2.10
simulinkModel_superchargerControl.png	Figure 2.11
SusperchargerControlPanel_controlDesk.png	Figure 2.12
FMEP_parameterized.png	Figure 3.1
OperatingRegion_40_NA.png	Figure 3.2
OperatingRegion_100_NA.png	Figure 3.2
OperatingRegion_40_boosted120.png	Figure 3.3
ISFC_40deg_NA.png	Figure 3.4
ISFC_40deg_boost120.png	Figure 3.5
BSFC_40deg_NA.png	Figure 3.6
BSFC_40deg_boost120.png	Figure 3.7
ITE_40deg_NA.png	Figure 3.8
ITE_40deg_boost120.png	Figure 3.9
Texh_40deg_NA.png	Figure 3.10
Texh_40deg_boost120.png	Figure 3.11
IMEP-IT-Speed-ISFCcombinedforalltemparaturesand fuels HCCI.png	Figure 3.12
CombinedISFCmap.png	Figure 3.13
CombinedBSFCmap_HCCI.png	Figure 3.14
CombinedBSFCmap.png	Figure 3.15
IT-IMEP-Speed-ITEcombinedforalltemparatures and fuels.png	Figure 3.16

Table C.9
Figure files included in this thesis (Contd.)

File Name	File Description
combinedITEmap.png	Figure 3.17
Combinedexhaustmap.png	Figure 3.18
Combinedexhausttempmap.png	Figure 3.19
ROneffect_combustion.png	Figure 3.20
RON_IMEP_TEF_CEF.png	Figure 3.21
tempeffect_IMEP_CEF_TEF.png	Figure 3.22
tempeffect_combustion.png	Figure 3.23
Boostpressureeffect_Pressure_heatrelease.png	Figure 3.24
Boostpressureeffect_Combustiongraphs.png	Figure 3.25
Boostpressureeffect_IMEP_TEF_CEF.png	Figure 3.26
Experimental FMEP vs Parameterized FMEP.png	Figure 4.1
P140T40.png	Figure 4.2
P140T60.png	Figure 4.3
mergeP140T40_ISFC.png	Figure 4.4
MergeP140T40_BSFC.png	Figure 4.5
MergeP140T40_indeffciency.png	Figure 4.6
MergeP140T40_Exhausttemp.png	Figure 4.7
ISFC_NA_RCCI.png	Figure 4.8
ISFC.png	Figure 4.9
BSFC_COV10_NA_RCCI.png	Figure 4.10
BSFC.png	Figure 4.11
ITE_NA_RCCI.png	Figure 4.12
ITE.png	Figure 4.13
Exhausttemp_NA_RCCI.png	Figure 4.14
Exhausttemp.png	Figure 4.15
ISFC_superchargerLossesaccounted.png	Figure 4.16
ITE_superchargerLossesaccounted.png	Figure 4.17
rcciRONeffect_pressuretrace_constantfuelenergy.png	Figure 4.22
Graph94.png	Figure 4.23
RONeffect_combustion_constantfuelenergy1.png	Figure 4.24
RONeffect_indicated_constantfuelenergy.png	Figure 4.25
rccitempEffect_pressuretrace.png	Figure 4.26
rccitempeffect_combustion.png	Figure 4.27
rccitempeffect_performance.png	Figure 4.28
boost_pressure_pressuretrace.png	Figure 4.29
rcciboost_pressure_combustionGraphs.png	Figure 4.30
rcciboost_pressure_performace.png	Figure 4.31

Table C.10
Figure files included in this thesis (Contd.)

File Name	File Description
Experimental FMEP vs Parameterized FMEP.png	Figure 5.1
T40_PPCI.png	Figure 5.2
T80_EPS.png	Figure 5.3
MergeISFCT40.png	Figure 5.4
MergeBSFCT40.png	Figure 5.5
MergeITET40.png	Figure 5.6
MergeexhausttempT40.png	Figure 5.7
ISFCoptimized.png	Figure 5.8
BSFCoptimized.png	Figure 5.9
ITEoptimized.png	Figure 5.10
Texhaustoptimized.png	Figure 5.11
pressuretrace.png	Figure 5.12
heatresleaserate.png	Figure 5.13
MEP_temperatureeffect.png	Figure 5.14
ITE_temperatureeffect.png	Figure 5.15
combustionGraphs_temperatureeffect.png	Figure 5.16
IMEP_superchargereffect.png	Figure 5.17
4-In-cylinder_pressure.png	Figure 5.18
5-heatreleaserate.png	Figure 5.19
thermaleff_superchargereffecr.png	Figure 5.20
CA50_superchargereffect.png	Figure 5.21
1-pressure.png	Figure 5.22
2-heatrelease.png	Figure 5.23
combustionGraphs_injectiontiming.png	Figure 5.24

Table C.11
Visio Figure files in this thesis

File Name	File Description
ThesisOrganization.vsx	Figure 1.3
ExperimentalTestSetup_12-9-2015.vsx	Figure 2.1
supercharger_Test_VFD_schematic.vsx	Figure 2.9

Table C.12
Project files for testing and data acquisition

File Name	File Description
Allengine68.slx	Dspace project file for the Engine Control Model
Reader20.vi	Labview Visual interface for online monitoring and control
kaushik_configfile_7-16- 2015.nce	Labview configuration file for EML team

Appendix D

Letters of Permission

† This permission is for Figure 1.1.

Figure D.1: Copyright permission for the Figure 1.1

† This permission is for Figure 1.2.

Figure D.2: Copyright permission for the Figure 1.2